AD_____

Award Number:
W81XWH-07-1-0708

TITLE:
Design, Fabrication, Characterization and Modeling of Integrated Functional Materials

PRINCIPAL INVESTIGATOR: Pritish Mukherjee, Ph. D.

CONTRACTING ORGANIZATION:
University of South Florida
Tampa, FL 33620

REPORT DATE:
October 2010

TYPE OF REPORT: Annual

PREPARED FOR: U.S. Army Medical Research and Materiel Command
                Fort Detrick, Maryland 21702-5012

DISTRIBUTION STATEMENT:

   X Approved for public release; distribution unlimited

REPORT DOCUMENTATION PAGE

Form Approved
OMB No. 0704-0188

1. REPORT DATE *(10-19-2010)*	2. REPORT TYPE Annual	3. DATES COVERED *(20 Sep 2009-19 Sep 2010*

4. TITLE AND SUBTITLE	5a. CONTRACT NUMBER
Design, Fabrication, Characterization and Modeling of Integrated Functional Materials	USAMRMC W81XWH-07-1-0708
	5b. GRANT NUMBER
	EDMS# 3349
	5c. PROGRAM ELEMENT NUMBER

6. AUTHOR(S)	5d. PROJECT NUMBER
PI: Pritish Mukherjee, Ph. D.	
Email: pritish@casusf.edu	5e. TASK NUMBER
	5f. WORK UNIT NUMBER

7. PERFORMING ORGANIZATION NAME(S) AND ADDRESS(ES)	8. PERFORMING ORGANIZATION REPORT NUMBER
University of South Florida 4202 East Fowler Avenue Tampa, FL 33620	

9. SPONSORING / MONITORING AGENCY NAME(S) AND ADDRESS(ES)	10. SPONSOR/MONITOR'S ACRONYM(S)
U.S. Army Medical Research and Materiel Command Fort Detrick, Maryland 21702-5012	
	11. SPONSOR/MONITOR'S REPORT NUMBER(S)

12. DISTRIBUTION / AVAILABILITY STATEMENT

Approved for public release; distribution unlimited

13. SUPPLEMENTARY NOTES

14. ABSTRACT

The dynamically evolving needs of the U.S. soldier in the battlefield in response to changes in the technology of warfare and associated threats require advances in multiple areas including biomedical diagnostics, chemical sensing, communication technology, efficient power generation without increased payload, and mobile refrigeration. These technological advances are critically dependent on the development of new and currently non-existing materials. This research addresses the directed development of novel materials towards long-term needs of the United States Army. In order to address specific areas of integrated functional materials targeted towards the needs of the U.S. soldier in the field we have initiated research efforts in three main areas which are diagnostics and sensing, communication and energy, and power generation and refrigeration. The specific three independent "Tasks" that have been undertaken are:
Task I: Nanostructured materials for biomedical diagnostics and chemical sensing
Task II: Multifunctional composites for communication and energy applications
Task III: Solid-state materials for power generation and refrigeration
The specific outcome of the research activities is expected to lead to new devices/systems/composite materials useful for the USAMRMC.

15. SUBJECT TERMS

Functional materials, integrated fabrication, nanobiotechnology, smart materials, multifunctional, dimensional integration, nanocomposites, sensor technology, thermoelectrics, solar cells, photovoltaics, polypeptide multilayer films

16. SECURITY CLASSIFICATION OF:			17. LIMITATION OF ABSTRACT	18. NUMBER OF PAGES	19a. NAME OF RESPONSIBLE PERSON USAMRMC
a. REPORT U	**b. ABSTRACT** U	**c. THIS PAGE** U	UU	96	**19b. TELEPHONE NUMBER** *(include area code)*

Standard Form 298 (Rev. 8-98)
Prescribed by ANSI Std. Z39.18

Design, Fabrication, Characterization and Modeling of Integrated Functional Materials
(Program Director and PI: Prof. Pritish Mukherjee, Department of Physics, USF, Tampa, FL)
(co-PIs: Profs. Hariharan Srikanth, Sarath Witanachchi and George Nolas)
(Contributing Faculty: Prof. Donald Haynie)

Table of Contents

Design, Fabrication, Characterization and Modeling of Integrated Functional Materials
(Program Director and PI: Prof. Pritish Mukherjee, Department of Physics, USF, Tampa, FL)
(co-PIs: Profs. Hariharan Srikanth, Sarath Witanachchi and George Nolas)
(Contributing Faculty: Prof. Donald Haynie)

I. Introduction

The dynamically evolving needs of the U.S. soldier in the battlefield in response to changes in the technology of warfare and associated threats require advances in multiple areas including biomedical diagnostics, chemical sensing, communication technology, efficient power generation without increased payload, and mobile refrigeration. These technological advances are critically dependent on the development of new and currently non-existing materials. This research addresses the directed development of novel materials towards long-term needs of the United States Army.

Objective:
In addition to the integration of multiple functionalities with desirable properties (thermal, electrical, magnetic, mechanical, optical, etc.), the connection to real-world applications and devices also requires the seamless integration of dimensions (nano, micro, meso, macro) leading to integrated functional materials. We have initiated this Integrated Functional Materials Project at the Physics Department at the University of South Florida (USF) geared towards precisely addressing this grand challenge of dual integration. A series of targeted projects specifically address a spectrum of issues relevant to the needs of the U.S. soldier.

Specific Aims:
The Physics Department at the University of South Florida is home to a unique doctoral program in Applied Physics with an affiliated industrial practicum and nationally recognized research programs in physical and chemical materials synthesis and characterization of bulk materials, thin films and nanomaterials; crystal fiber growth; fundamentals of materials manufacturing processes and computational theoretical materials physics. This research synergistically coalesces existing expertise and leverages research infrastructure at USF in novel bulk materials synthesis, thin film growth, and nanotechnology. These goals are being further addressed through multidisciplinary research and new infrastructure development. The basic purpose of this project is to develop the novel science base both in the areas of multi-scale dimensional integration as well as multiple functional integration leading to previously unattained integrated functional materials.

Study Design:
In order to address specific areas of integrated functional materials targeted towards the needs of the U.S. soldier in the field we are directing the research efforts in three main areas which are diagnostics and sensing, communication and energy, and power generation and refrigeration. The specific three independent "Tasks", further subdivided into seven "Projects" are:

Task I: Nanostructured materials for biomedical diagnostics and chemical sensing
(Technical Directors.: Drs. H. Srikanth and P. Mukherjee)

Project 1	Functional magnetic fluids for biomedical applications
Project 2	Nanoporous/nano-wire structures and polymer nanotemplates for sensing and molecular manipulation
Project 3	Carbon-nanotube based sensors
Project 4	Functional materials for affecting cell proliferation and locomotion

Task II: Multifunctional composites for communication and energy applications
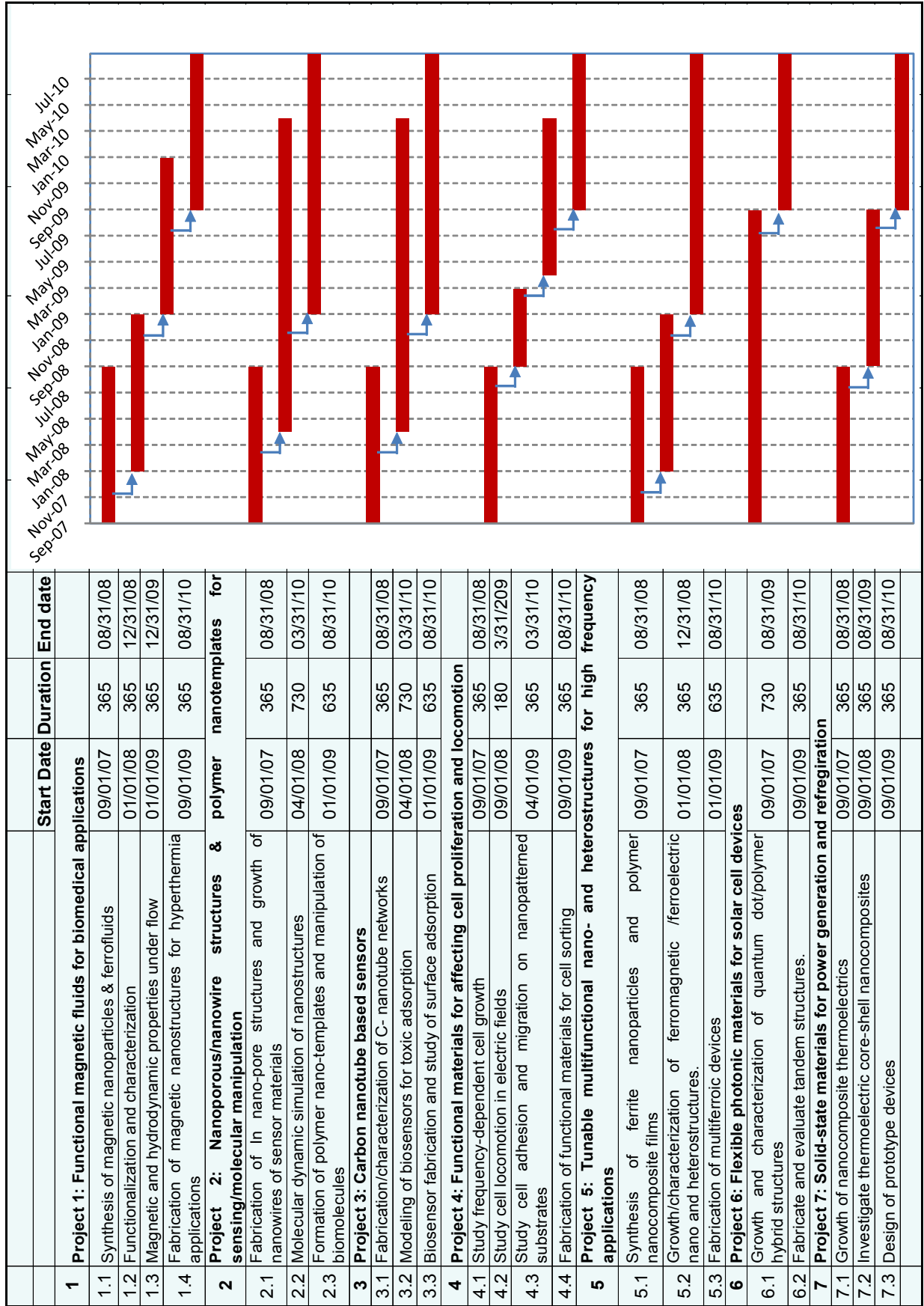*(Technical Director: Dr. S. Witanachchi)*

Project 5	Tunable multifunctional nano- and heterostructures for RF and microwave applications
Project 6	Flexible photonic materials for solar-based energy sources

Task III: Solid-state materials for power generation and refrigeration
(Technical Director: Dr. G. S. Nolas)

Project 7	High-performance nanofabricated thermoelectric materials for power generation and refrigeration

The timeline for proposed activities for each of these projects (over the three-year period of research) is detailed in the Gantt chart on the following page.

		Start Date	Duration	End date
1	**Project 1: Functional magnetic fluids for biomedical applications**			
1.1	Synthesis of magnetic nanoparticles & ferrofluids	09/01/07	365	08/31/08
1.2	Functionalization and characterization	01/01/08	365	12/31/08
1.3	Magnetic and hydrodynamic properties under flow	01/01/09	365	12/31/09
1.4	Fabrication of magnetic nanostructures for hyperthermia applications	09/01/09	365	08/31/10
2	**Project 2: Nanoporous/nanowire structures & polymer nanotemplates for sensing/molecular manipulation**			
2.1	Fabrication of In nano-pore structures and growth of nanowires of sensor materials	09/01/07	365	08/31/08
2.2	Molecular dynamic simulation of nanostructures	04/01/08	730	03/31/10
2.3	Formation of polymer nano-templates and manipulation of biomolecules	01/01/09	635	08/31/10
3	**Project 3: Carbon nanotube based sensors**			
3.1	Fabrication/characterization of C- nanotube networks	09/01/07	365	08/31/08
3.2	Modeling of biosensors for toxic adsorption	04/01/08	730	03/31/10
3.3	Biosensor fabrication and study of surface adsorption	01/01/09	635	08/31/10
4	**Project 4: Functional materials for affecting cell proliferation and locomotion**			
4.1	Study frequency-dependent cell growth	09/01/07	365	08/31/08
4.2	Study cell locomotion in electric fields	09/01/08	180	3/31/209
4.3	Study cell adhesion and migration on nanopatterned substrates	04/01/09	365	03/31/10
4.4	Fabrication of functional materials for cell sorting	09/01/09	365	08/31/10
5	**Project 5: Tunable multifunctional nano- and heterostructures for high frequency applications**			
5.1	Synthesis of ferrite nanoparticles and polymer nanocomposite films	09/01/07	365	08/31/08
5.2	Growth/characterization of ferromagnetic /ferroelectric nano and heterostructures.	01/01/08	365	12/31/08
5.3	Fabrication of multiferroic devices	01/01/09	635	08/31/10
6	**Project 6: Flexible photonic materials for solar cell devices**			
6.1	Growth and characterization of quantum dot/polymer hybrid structures	09/01/07	730	08/31/09
6.2	Fabricate and evaluate tandem structures.	09/01/09	365	08/31/10
7	**Project 7: Solid-state materials for power generation and refregiration**			
7.1	Growth of nanocomposite thermoelectrics	09/01/07	365	08/31/08
7.2	Investigate thermoelectric core-shell nanocomposites	09/01/08	365	08/31/09
7.3	Design of prototype devices	09/01/09	365	08/31/10

II. Technical Description of Research Progress

The following discussion details the progress made on each of the Tasks during the third year of research:

Task I: Nanostructured materials for biomedical diagnostics and chemical sensing

[A]   Functional magnetic fluids for biomedical applications

(a) Synthesis and characterization of magnetic nanostructures:

The goal of this project is to synthesize and characterize advanced magnetic nanostructures for biomedical applications. Graduate student Mr. Sayan Chandra received support and worked on this project during this quarter. In addition, undergraduate student Ms. Daria Karpenko, graduate student Ms. Kristen Stojak and postdoctoral researchers Dr. Susmita Pal and Dr. Manh-Huong Phan were key contributors to the project.

Cobalt ferrite (CFO) nanocrystals - shape control and magnetism:

The shape of nanomaterials can be a vital issue in determining the novelty and uniqueness of material properties. Synthesis of shape controlled nanocrystals is a great challenge to materials scientists. Here we report the synthesis, structural and magnetic characterization of spherical and cube shaped $CoFe_2O_4$ nanocrystals.

Fig. 1: XRD of CFO nanoparticles

Synthesis procedure:
In a typical synthesis, 2 mmol of Cobalt (II) acetylacetonate [Co(acac)$_2$] and Iron (III) acetylacetonate Fe(acac)$_3$] were taken in 1:2 ratio [1] 10 mmol 1,2-hexadecanediol, 6 mmol oleic acid, 6 mmol oleylamine and 20 ml benzyl ether were added to Iron (III) acetylacetonate and Cobalt (II) acetylacetonate mixture. The mixture was stirred magnetically under a flow of argon. The mixture was heated to 200 ^{0}C for 2 h and then refluxed at 300^{0}C for another 1 hr in presence of argon. The reaction mixture was cooled to room temperature by removing the heat source. Under ambient conditions, 40 ml ethanol was added to the mixture and a black precipitate was separated by centrifugation. The black product was dissolved in hexane in presence of oleic acid ($\sim$0.05 ml) and oleylamine ($\sim$0.05 ml). The product of 8nm $CoFe_2O_4$ particle was then precipitated with ethanol, centrifuged to remove the solvent and redispersed into hexane.

We have characterized these samples by XRD and TEM and magnetic characterizations were done using the PPMS.
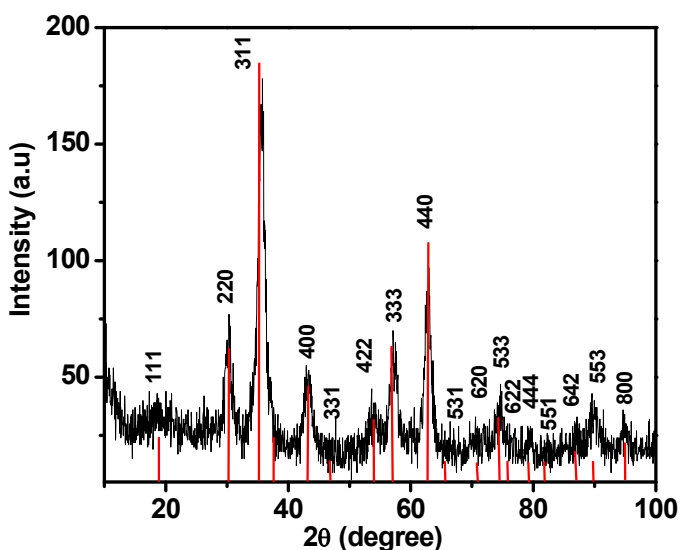
Structural characterization:

The XRD pattern of as-synthesized nanoparticles were identified as the cubic spinel structure of $CoFe_2O_4$ (Figure 1). The particle size, shape and distribution were determined from TEM experiments. Figure 2 show the TEM image of spherical and cube shaped monodisperse nanocrystals with diameter of 8 nm± 1 nm.
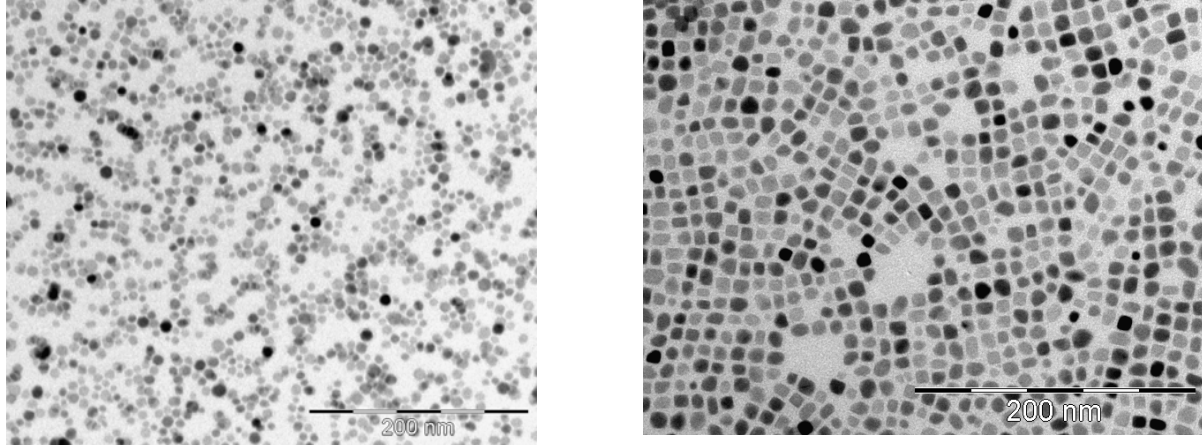

Fig. 2: (a) spherical CFO (b) cube-shaped CFO

Magnetic characterization:

The temperature and magnetic field variation of the magnetization of the nanocrystals were studied using our PPMS. Figure 3 show the zero field cooling (ZFC) and field cooling (FC) M-T
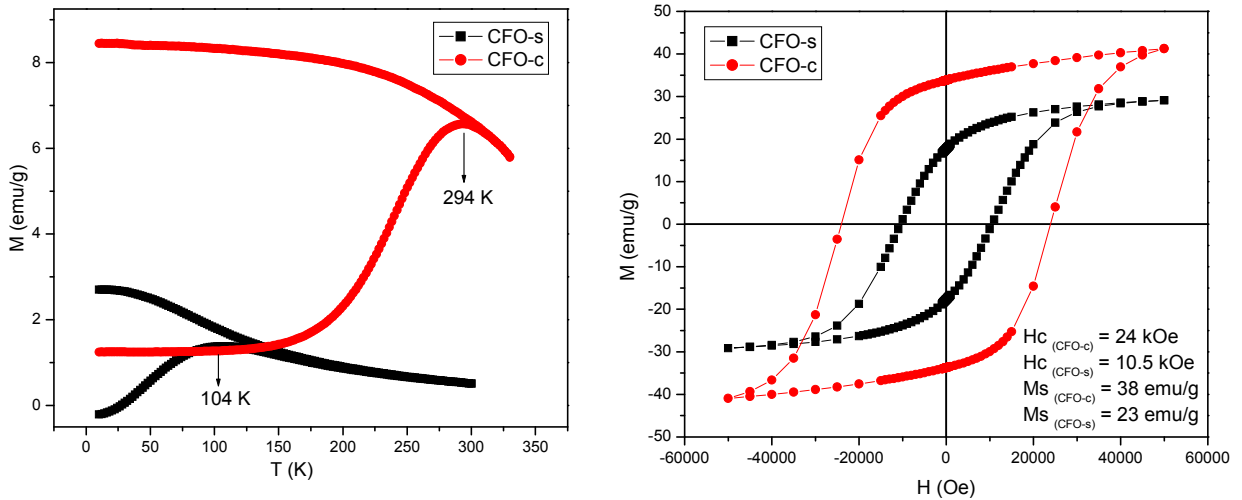
Fig. 3: Comparison of M-T and M-H data for spherical and cubic $CoFe_2O_4$ nanocrystals

curves as well as the M-H loops at 10K for spherical and cubic nanocrystals.

The blocking temperature (T_B) of spherical $CoFe_2O_4$ (CFO-s) is 104 K and T_B of cubic $CoFe_2O_4$ (CFO-c) is 294 K. The saturation magnetization (Ms) and coercivity (Hc) values of the nanocubes are significantly higher than the spherical nanocrystals. The M_s and H_c values for CFO-c is 41 emu/g and 24 kOe whereas the M_s and H_c of CFO-s are 29 emu/g and 10.5 kOe.

The significant increase in T_B, H_c and M_s in cubic particles is due to the enhancement of magnetic anisotropy compared to spherical particles. The room temperature M-H data for CFO-c The significant increase in T_B, H_c and M_s in cubic particles is due to the enhancement of magnetic anisotropy compared to spherical particles. The room temperature M-H data for CFO-c and CFO-s do not show any coercivity, which indicate both the systems are superparamagnetic in nature.

Synthesis and magnetic properties of cobalt ferrite and cobalt ferrite-PZT core shell nanotubes:

Multiferroic composite materials consisting of both ferro/ferrimagnetic and ferroelectric phases have drawn an increasing amount of interest due to their capability of efficient energy transfer between electric energy and magnetic energy, and their potential applications in many multifunctional devices. Such materials can display the magnetoelectric effect, a dielectric polarization variation as a response to an applied magnetic field, or an induced magnetization by an external electric field.

Fig. 4: Room temperature M-H loops exhibit superparamagnetism for nanospheres and nanocubes

In this work we report the synthesis method of core-shell nanorod structures with $CoFe_2O_4$ (CFO) core and $Pb(Zr_{0.52}Ti_{0.48})O_3$ (PZT) shell using alumina template and their structural and magnetic characterization.

Experiment:
A 0.3M PZT precursor with the molar ratio of 1.1:0.52:0.48 was prepared by dissolving lead acetate $Pb(CH_3CO_2)_2 3H_2O$, zirconium propoxide $Zr(CH_2CH_2CH_3O)_4$, and titanium butoxide $Ti(C_4H_9O)_4$ into 2-methoxyethanol [2,3]. An alumina (AAO) template with pore diameter of 200 nm was immersed into the PZT precursor solution for 20 min then the wet template was baked in air at 300 °C for solvent removal and annealed in air at 725^0C for 1 h to grow the PZT nanorods. After annealing the alumina template, a few drops of $CoFe_2O_4$ ferrofluid (synthesized in our lab) was deposited on to the membrane keeping a permanent magnet ($\mu_0 H = 0.4$ T) underneath the template. $CoFe_2O_4@PZT$ core-shell nanorods were collected from the AAO template by dissolving the template in NaOH solution.

Characterization:
XRD has been done on PZT nanorods and $CoFe_2O_4$ separately and the perovskite PZT phase (Figure 5) and spinel $CoFe_2O_4$ phase were observed. TEM images show the CFO and CFO filled PZT nanorods. Magnetic measurements were done using the commercial Physical Property Measurement System (PPMS).
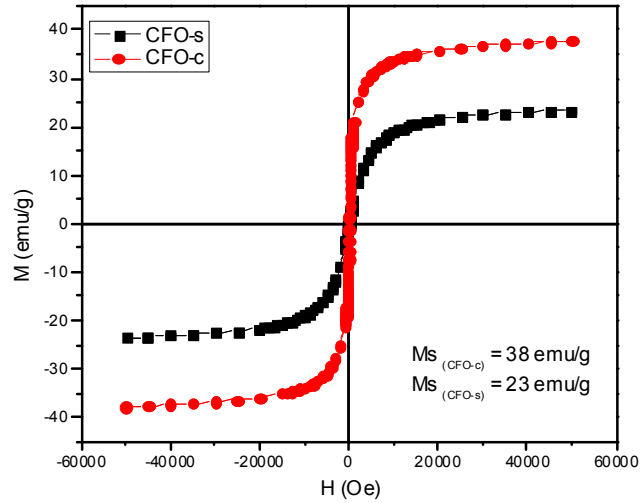
Results and Discussion:

The transmission electron microscope (TEM) image of $CoFe_2O_4$ and $CoFe_2O_4$ filled PZTs are shown in Figure 5 also. TEM image shows the cube shape CFO nanoparticles with average particle size 8 ± 1 nm. Figure 1b shows that particles are nicely packed inside the PZT. The average length of PZT is 4-5 μm and diameter is 250-300 nm with 30 nm wall thickness. So the aspect ratio of these magnetic nanotubes comes out to be ~ 20.
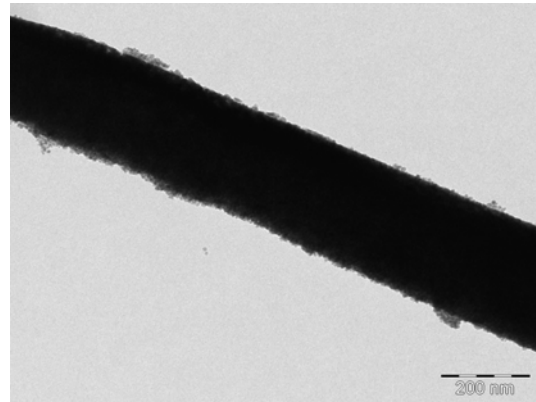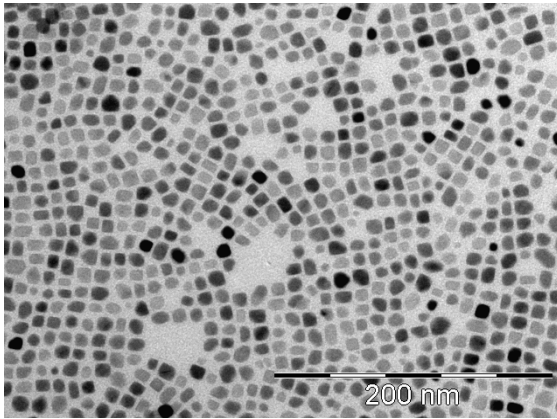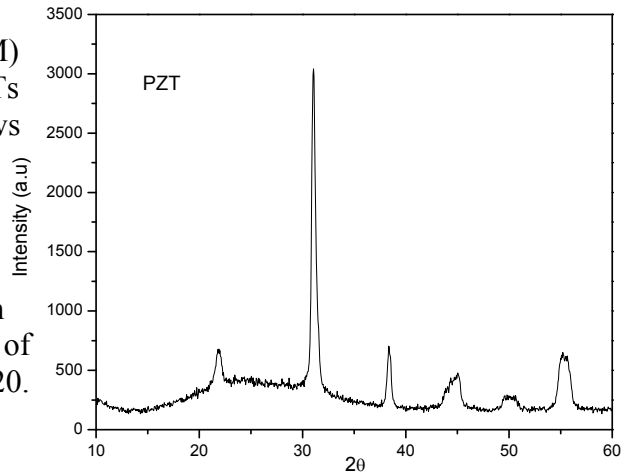

Fig. 5: XRD of PZT nanotubes; TEM images of CFO nanoparticles and the PZT nanotubes filled with nanoparticles

Magnetic characterization:

All the magnetic measurements including the temperature dependence of zero field cooled (ZFC) and field cooled (FC) susceptibility, M-H hysteresis loop measurements were done using a PPMS over a wide range of temperature and magnetic fields. For these measurements, the dry samples were loaded in a standard, non magnetic gelatin capsule. The blocking temperature is T_B ~ 294 K for $CoFe_2O_4$ NPs and 307 K in $CoFe_2O_4$ filled PZT nanotubes. The small increase in T_B indicates that the anisotropy energy density of the nanoparticles increase This may due to the confinement of the nanoparticles inside the PZT nanorods.

M versus H measurements at 10K in ZFC mode show a hysteresis loop with larger value of coercivity (H_c) for both CFO and CFO-PZT samples (Figure 6). The coercivity of $CoFe_2O_4$ NPs is ~ 24 kOe and for CFO-PZT sample H_c ~ 21 kOe. The saturation magnetization M_s of CFO is 41 emu/g and it is almost same in CFO-PZT system (M_s = 38 emu/g). The room temperature M-H data shows no coercivity for both the samples, indicating the superparamegnetic nature of the nanoparticles. From the magnetization results it is worth mentioning that the coercivity as well as the saturation magnetization does not change

considerably in CFO-PZT system which is a very promising observation from magnetic-field guided applications point of view.
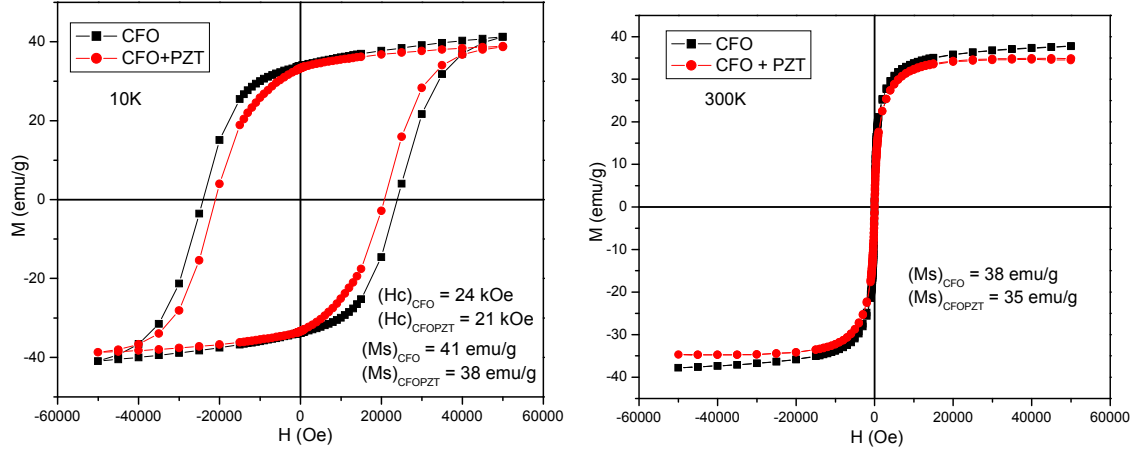

Fig. 6: M-H loops at 10K and 300K for the CFO and CFO-filled PZT nanotube samples

Manganese ferrite (MFO) nanoparticles - size control and magnetism:

Here we report the synthesis, structural and magnetic characterization of spherical and cube shaped $MnFe_2O_4$ nanoparticles.

Synthesis procedure:

In a synthesis process similar to that used for the CFO nanocrystals, 2 mmol of Manganese (II) acetylacetonate [$Mn(acac)_2$] and Iron (III) acetylacetonate Fe(acac)$_3$] were taken in 1:2 ratio [1] 10 mmol 1,2- hexadecanediol, 6 mmol oleic acid, 6 mmol oleylamine and 20 ml benzyl ether were added to Iron (III) acetylacetonate and Cobalt (II) acetylacetonate mixture. The mixture was stirred magnetically under a flow of argon. The mixture was heated to 200 ^{0}C for 2 h and then refluxed at 300^{0}C for another 1 hr in presence of argon. The reaction mixture was cooled to room temperature by removing the heat source. Under ambient conditions, 40 ml ethanol was added to the mixture and a black precipitate was separated by centrifugation. The black product

was dissolved in hexane in presence of oleic acid ($\sim$0.05 ml) and oleylamine ($\sim$0.05 ml). The product of 6nm $MnFe_2O_4$ particle was then precipitated with ethanol, centrifuged to remove the solvent and redispersed into hexane.

We have characterized these samples by XRD and TEM and magnetic characterizations were done using the PPMS.

Structural characterization:

The XRD pattern of as-synthesized nanoparticles were identified as the cubic spinel structure of $MnFe_2O_4$ (Figure 7). The particle size, shape and distribution were determined from TEM experiments. Figure 8 show the TEM image of spherical monodisperse nanocrystals with diameter of 6 nm$\pm$ 0.5 nm.
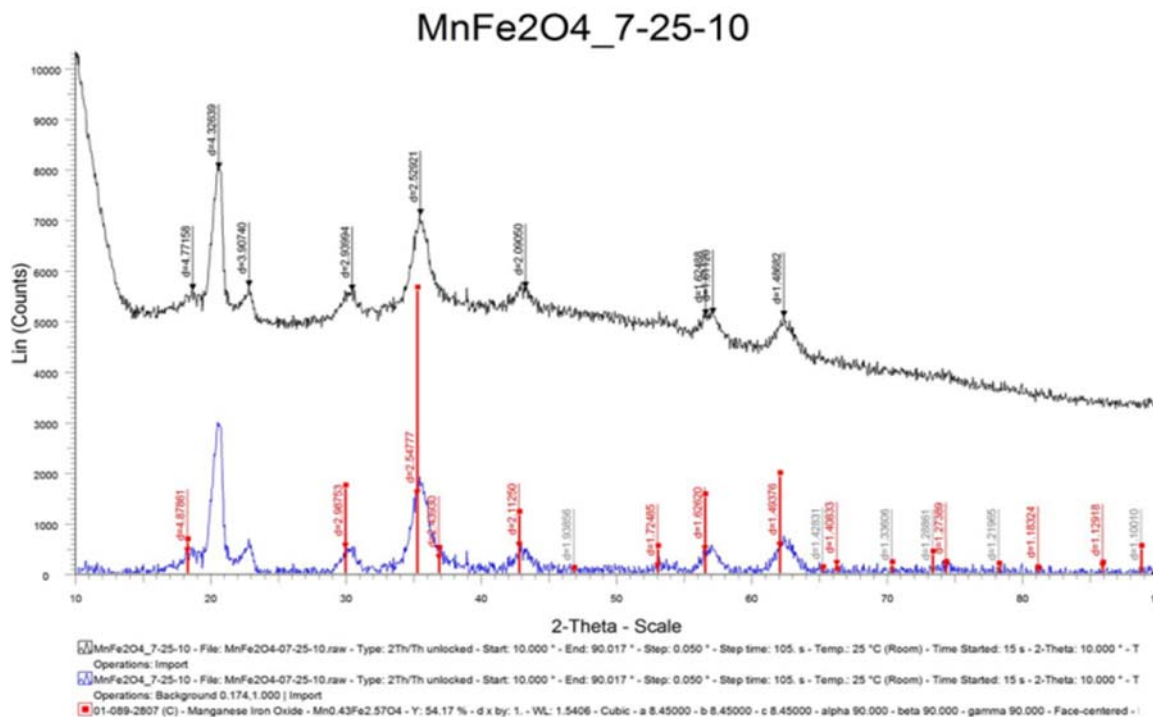
Fig. 7: XRD of MFO nanoparticles

<u>Magnetic characterization:</u>

The temperature and magnetic field variation of the magnetization of the nanocrystals were studied using our PPMS. Figure 9 show the zero field cooling (ZFC) and field cooling (FC) M-T curves as well as the M-H loops at 10K for spherical nanocrystals.

The blocking temperature (T_B) of spherical $MnFe_2O_4$ (MFO) is 32 K. The saturation magnetization (Ms) and coercivity (Hc) values of the nanoparticles are 56 emu/g and 100 Oe. There is a significant decrease in T_B and M_s and a decrease in H_C in the MFO nanoparticles as compared to the CFO counterparts. The room temperature M-H data MFO does not show any coercivity, which indicate the system is superparamagnetic in nature.
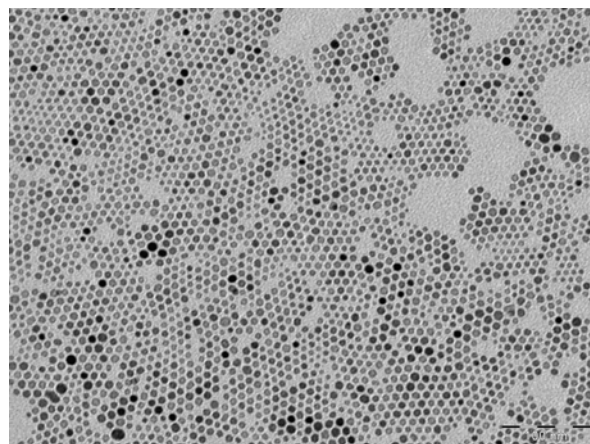
Fig. 8: TEM image of spherical MFO

Magnetic Polymer Nanocomposites:

Polymer nanocomposites have been paid much attention because of their unique electrical, thermal, mechanical, and optical properties. Polyvinyledene fluoride (PVDF) is one of
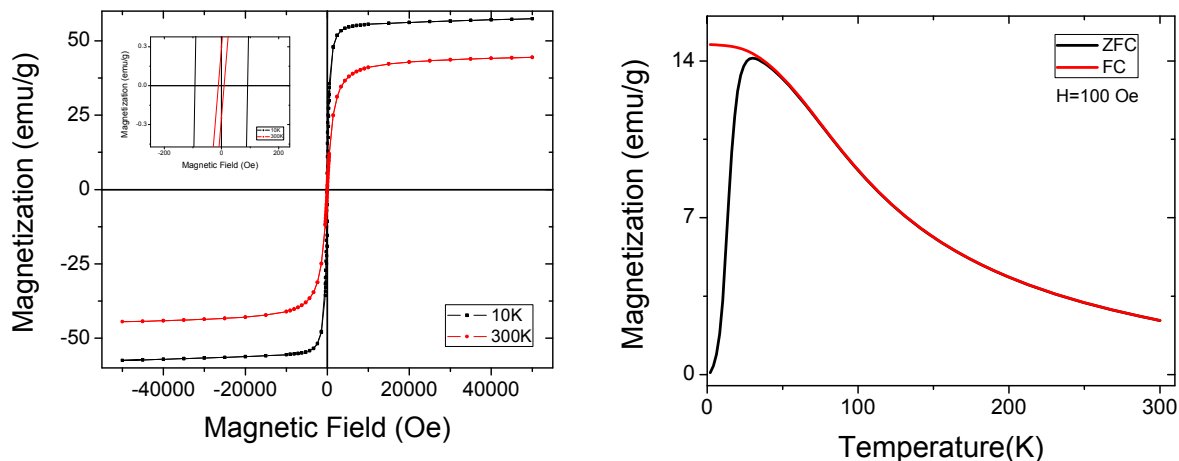
Fig. 9: Comparison of M-T and M-H data for spherical $MnFe_2O_4$ nanocrystals

the promising systems for different types of sensor applications. It is a ferroelectric polymer exhibiting efficient piezoelectric and pyroelectric properties. These characteristics make it useful in sensor and battery applications. However, the dispersion of nanoparticles into a polymer matrix has been a bottleneck for nanocomposite fabrication. One of the best ways to uniformly disperse nanoparticles in a polymer matrix is to functionalize the particle surface with organic surfactants. If the particles are surface functionalized with organic surfactants, they will become more compatible with the polymer matrix, resulting in a homogeneous dispersion of nanoparticles. Here we report the synthesis of PVDF-Fe_3O_4 nanocomposites. First we have made Fe_3O_4 nanoparticles and functionalized them with Polyethylene glycol (PEG). PEG is an amphiphilic polymer and coating on Fe_3O_4 by PEG makes iron oxide nps soluble in different solvents. Synthesis procedures are outlined below:

Synthesis of Fe_3O_4 nanoparticles:

2 mmol of Fe(acac)$_3$ was dissolved in a mixture of 10 ml benzyl ether and 10 mL oleylamine. The solution was dehydrated at 110 °C for 1 h, and was quickly heated to 300 °C and kept at this temperature for 2 h [4]. Ethanol was added into the solution after it was cooled to room temperature. The precipitate was collected by centrifugation and was washed with ethanol three times. Finally, the product was dried at room temperature.

Surface Modification of Fe_3O_4 Nanoparticles:

Polyethylene glycol (M = 3000), *N*-hydroxysuccinimide, *N,N'*-dicyclohexylcarbodiimide and dopamine hydrochloride were dissolved in a mixture solvent containing CHCl$_3$, DMF and anhydrous Na$_2$CO$_3$. The solution was stirred at room temperature for 2 h before Fe_3O_4 nanoparticles were added, and the resulting solution was stirred overnight at room temperature under Ar protection. The surface modified Fe_3O_4 nanoparticles were precipitated by adding hexane and dried under Ar.

Synthesis of PVDF-Fe_3O_4 nanocomposites:

Dried Fe_3O_4 were added to the dimethylformamide solution of PVDF by 30 wt%, 50 wt% and 80 wt% ratio. The polymer nanocomposites were dried at room temperature. We have characterized these samples by XRD, TEM (Figure 11). Magnetic properties were studied using our PPMS.
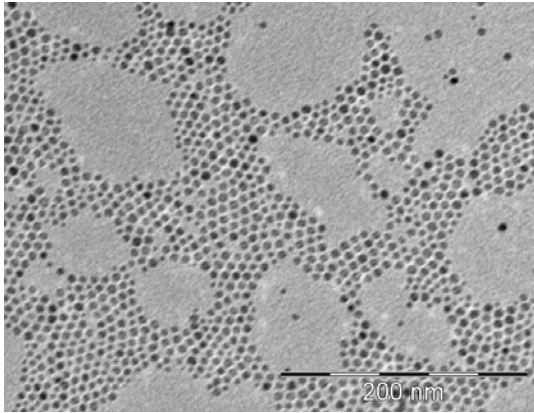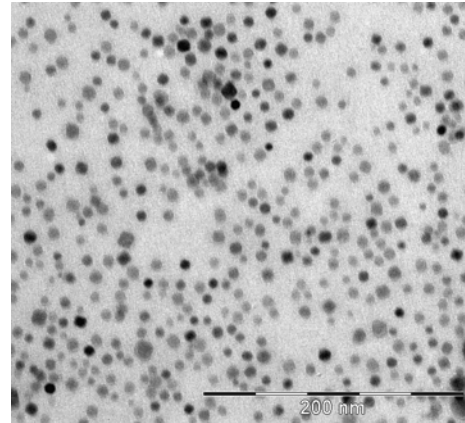
Fig. 10a: TEM image of Fe_3O_4 nps   Fig. 10b: TEM image of PVDF-Fe_3O_4

The TEM image (Fig 10a) shows that the average particle size of Fe_3O_4 is ~ 7 nm with uniform dispersion. TEM image (Fig 10b) of PVDF-Fe_3O_4 composite shows that the particles are well dispersed in the polymer matrix.

Magnetic characterization:

All the magnetic measurements including the temperature dependence of zero field cooled (ZFC) and field cooled (FC) susceptibility, M-H hysteresis loop measurements were done using a Physical Properties Measurement System (PPMS) over a wide range of temperature and magnetic fields. For these measurements, the dry samples were loaded in a standard, non-magnetic gelatin capsule. The blocking temperature (T_B) is ~ 40 K for Fe_3O_4 NPs and T_B is same (40K) for all the samples. M versus H measurements at 10K in ZFC mode shows the coercivity
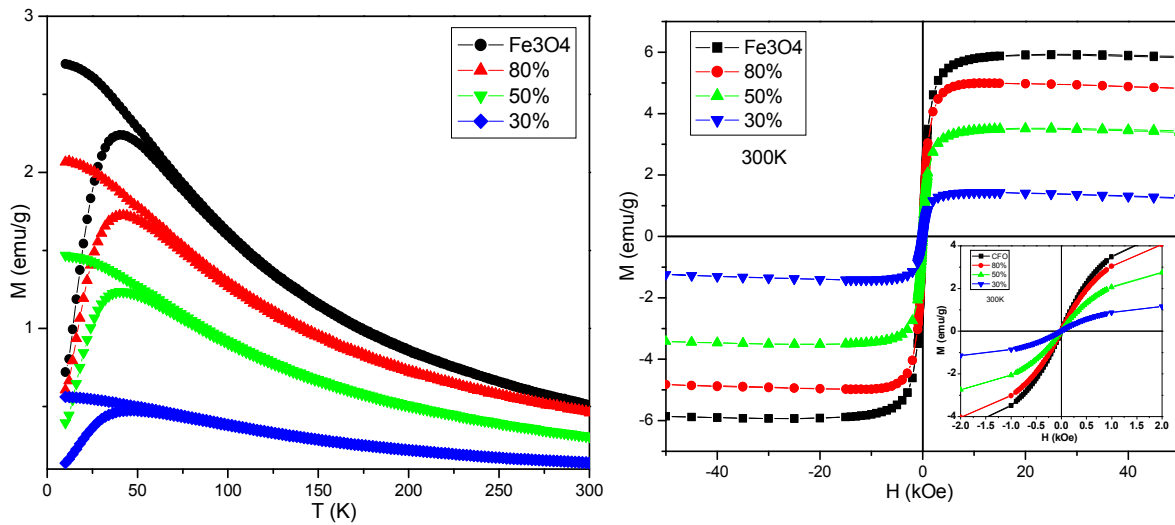

Fig. 11: (Left) M-T data of PVDF-Fe_3O_4 nanocomposites. (Right) M-H curves at 300K showing classic superparamagnetic response in all the composites

14

(H_c) for Fe_3O_4 and PVDF-Fe_3O_4 samples. The coercivity of Fe_3O_4 NPs and all the PVDF-Fe_3O_4 composites are ~ 185 Oe. The saturation magnetization (M_s) of Fe_3O_4 is 7 emu/g and the M_s values decrease with decreasing the percentage loading of Fe_3O_4 in the PVDF-Fe_3O_4 composites. The room temperature M-H data shows no coercivity for all the samples, indicating the superparamagnetic nature of the nanoparticles (Figure 11).

Rogers – $CoFe_2O_4$ nanocomposites:

The second system we worked on is making polymer nanocomposites with tunable microwave properties. The polymer used here is a commercial low-loss polymer from Rogers Corporation. It is a durable polymer that can survive the post-processing. We have chosen cobalt ferrite because it has higher saturation magnetization and a lower magnetic loss when compared with magnetite. Another advantage of using cobalt ferrite NPs is that it has higher blocking temperature, which is significantly higher than the blocking temperature of magnetite NPs. Thus the magnetic properties of polymer nanocomposite formed by cobalt ferrite can be controlled easily by controlling the temperature as the nanoparticles change from superparamagnetic to ferromagnetic in the vicinity of room temperature which would make them useful for sensor applications.

Synthesis:
Synthesis of 5nm $CoFe_2O_4$ nanoparticles:
$CoFe_2O_4$ nanoparticles were synthesized by taking 2 mmol mixture of cobalt (II) acetylacetonate and iron (III) acetylacetonate in 1:2 ratio by weight.[1] Then the mixture was added to 10 mmol 1,2- hexadecanediol, 6 mmol oleic acid, 6 mmol oleylamine, and 20 ml benzyl ether. The mixture was heated at 200°C for 2 h with constant stirring and then refluxed at 300°C for 1 hr in presence of Ar gas. Then 40 ml ethanol was added to the cooled mixture and the black precipitate was separated by centrifugation. The black product was dissolved in hexane in the presence of oleic acid (~0.05 ml) and oleylamine (~0.05 ml).

Synthesis of polymer nanocomposites:
The polymer nanoparticle composites (PNCs) (Rogers polymer, a commercial copolymer provided by the Rogers Corporation and cobalt ferrite) were prepared by adding calculated amount of cobalt ferrite in the polymer by weight to get the desired compositions. Nanocomposites with 30 wt%, 50 wt% and 80 wt% of cobalt ferrite in Rogers were prepared. Both the polymer and the nanoparticles were dissolved in hexane and magnetically stirred overnight to obtain uniform dispersion.

Results and discussion:
Structural characterization:
Figure 3a shows the transmission electron microscopy (TEM) image of $CoFe_2O_4$ nanoparticles with particle size 9 nm in diameter and are well separated from each other. TEM image of 80 wt% PNCs are depicted in Figure 12a. From Figure 12b it can be observed that the particles are evenly dispersed throughout the polymer matrix.
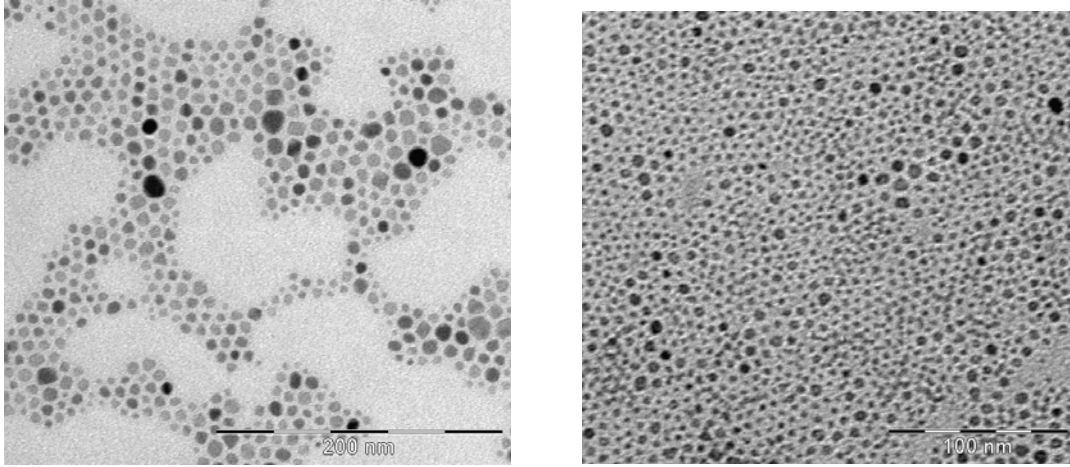
Fig. 12(a): TEM image of as synthesized CoFe$_2$O$_4$ nanoparticles. 12(b): Particles dispersed in Rogers polymer showing excellent dispersion

Magnetic measurements:

The magnetization (M) measurements were done at temperature (T) range starting from 300K down to 10K and magnetic field (H) up to 50 kOe using Physical Properties Measurement System (PPMS). The DC magnetic characterizations were done using field cooled – zero field cooled (FC-ZFC) M-T and M-H hysteresis loop measurement at ZFC mode. The blocking temperature (T$_B$) is ~ 298 K for CoFe$_2$O$_4$ NPs and T$_B$ is same for all the Rogers-CFO nanocomposites as shown in Figure 13.

M versus H measurements at 10K in ZFC mode shows the high coercivity (H$_c$) for CoFe$_2$O$_4$ and Rogers-CFO samples (Figure 14). The coercivity of CoFe$_2$O$_4$ NPs is ~18 kOe and
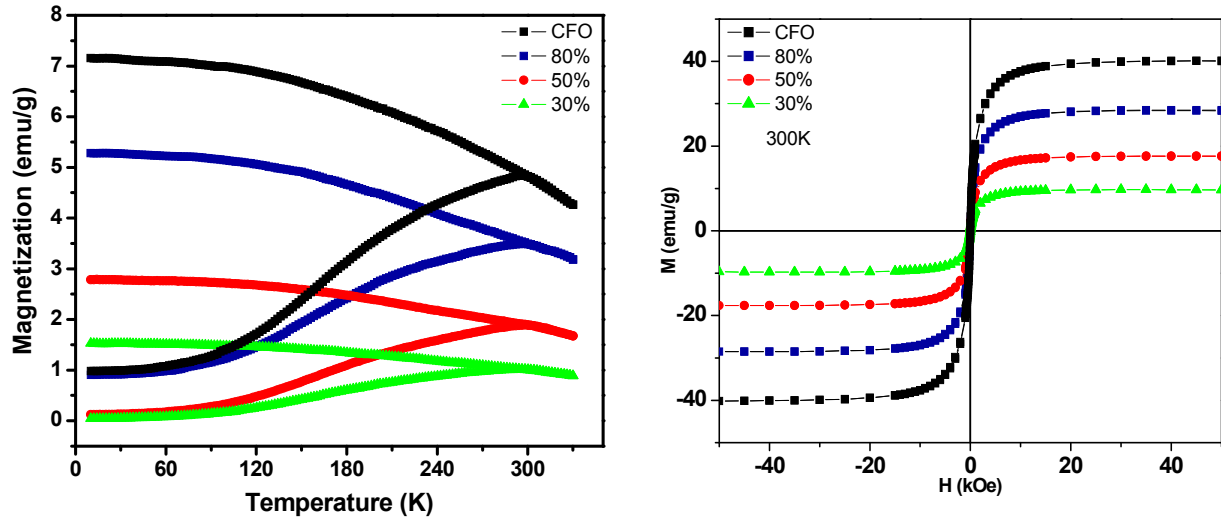

Fig. 13: (Left) ZFC and FC magnetization for CFO and polymer nanocomposites. Blocking temperature is close to room temperature which makes it useful for applications. (Right) M-H curves at 300K showing superparamagnetic response without hysteresis

16

the coercivity does not change in the Rogers-CFO composites. Note that the large coercivity in this system is expected because of large magnetic anisotropy of the cobalt ferrite system. The saturation magnetization (M_s) of $CoFe_2O_4$ is 45 emu/g and the M_s values decrease with decreasing the percentage loading of $CoFe_2O_4$ in the composites.

Overall, we have demonstrated excellent control over nanoparticle dispersion in two polymer nanocomposite systems. Our work in this quarter shows the potential of these tunable magnetic polymers for applications in biomedical sensing and microwave communication devices.
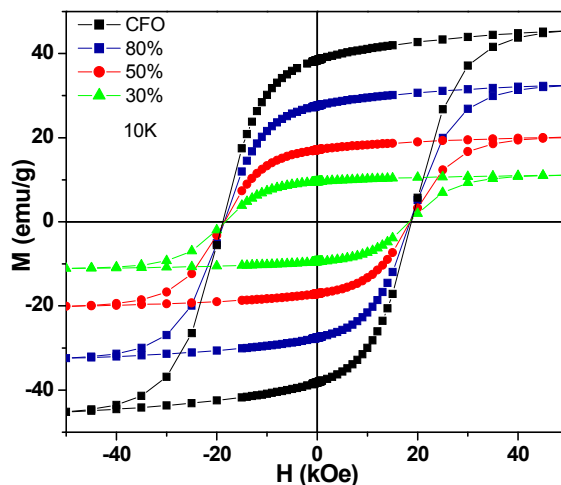

Fig. 14: Hysteresis loops for the CFO polymer nanocomposite system showing large coercivities at 10K in the blocked state.

(b) Graphene – fabrication and characterization:

In our project on carbon nanotube sensors, we have embarked on a new and exciting area in 2010 which involves synthesizing high quality graphene which is a topical material currently receiving a lot of attention. We are pleased to report the success in our efforts primarily due to the work done by CIFM graduate student Sayan Chandra who is working on this system towards his Ph.D. degree.

Graphene is a material of great interest primarily because of its unique electronic [5], mechanical [6] and optical [7] properties. Different growth mechanisms have been found in recent years, but the challenge remains to produce high quality mono-layer graphene over a large area. Our aim here is to grow graphene over a large area and then study the interactions of
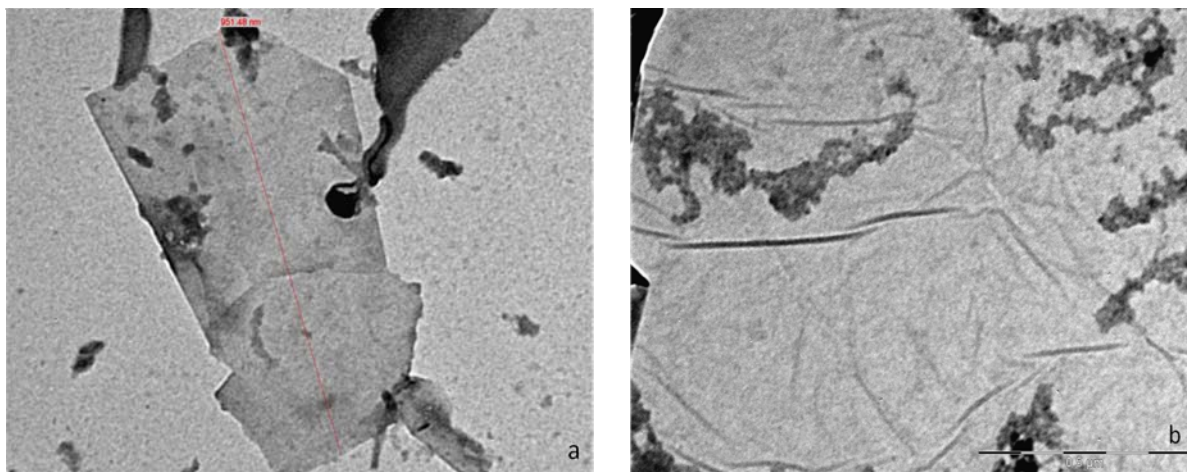

Fig. 15: TEM image of graphene (a) 1 micron single layer graphene flake, (b) ripples observed on a monolayer.

magnetic nanoparticles dispersed across graphene at room temperature. This study can give us information and a basic understanding as how well can we control the spin-orbit interactions for future applications in spintronics and advanced magnetic sensors.

We have adapted a simple thermal decomposition synthesis procedure for graphene growth. Methane is passed over a thin film of Ni on a SiO_2/Si substrate at 900 °C, and as the methane molecules break at such high temperatures, the carbon diffuses into the Ni. During the cooling process, carbon precipitates out as graphene. The number of layers in graphene formed can be controlled by the cooling rate. It is found that cooling at 10°C/s produces high quality graphene [6].

Our goal is to use graphene as a functional substrate on which magnetic nanoparticle assemblies can be created using Langmuir-Blodgett deposition of monolayers and multilayers. We intend to control the interparticle separation by changing concentration of the ferrofluids and look at the interaction of the nanoparticles in the 2D arrangement and how it changes as the number of layers is increased. We believe that as we keep increasing the number of monolayers, after a critical value is reached, the interactions will show a transition from 2D to 3D like behavior. This critical value of number of layers, will give us insight into the length of the dipolar interactions and ordering between the nanoparticles. With a series of experiments we can see if the interactions and the critical number of layers changes from highly conducting graphene substrate to a non-conducting substrate.

We were able to produce continuous sheets of 1 x 1cm^2 of graphene with layer variation up to 10 layers. Figure 15 shows the TEM image of a single layer graphene. Monolayers up to a few microns in length were achievable. We were unable to get larger monolayer sheets because its size is limited by the size of the Ni grains which acts as the substrate. Ripples and stacking of layers were observed at the grain boundaries because of the difference in thermal expansion co-efficient of graphene and nickel.

Raman spectroscopy was done on the samples prepared and shown in Fig. 16. The 2D peak at 2700 cm^{-1} confirms graphene. Since this peak is symmetric and has no bump at the left side, we can safely say that the grown material is not graphite but graphene. The G peak at 1580 cm^{-1} is expected for any carbon material. Three different samples were synthesized by varying
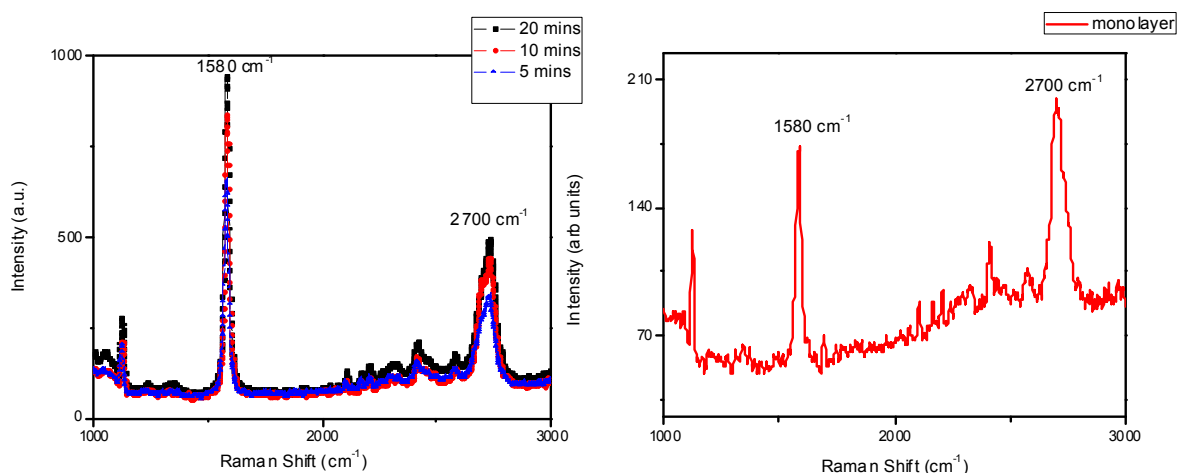

Fig. 16: Raman Spectra of segregated carbon on Ni surface with different cooling rates.

the growth time. The number of layers of graphene is reflected by the ratio of the height of G:2D peaks. For all the three samples, the ratio is about 1.9. So, we can say that the variation in growth time did not alter the quality of graphene formed. The number of layers estimated from the height ratio of the G and 2D peaks is 5-10 layers. However, we have found areas of monolayer which have shown a G:2D value less than 1 as shown in Fig. 16. The Raman signal appears to be noisy because of the substrate.

AFM images show flat regions with mean roughness of 6.5 nm in the selected area as seen in Figure 17(a). The graphene sheets were transferred to a quartz substrate. The transferred graphene sheets showed a mobility of 800 $cm^2V^{-1}s^{-1}$ over a sample area of $1cm^2$. The mobility observed was relatively low because of the large sample area which is expected due to the presence of ripples and defects in the grain boundaries. Once the graphene sheet was transferred onto quartz substrate, multiple layers of 9nm Fe_3O_4 were patterned on the grapheme sheet by Langmuir-Blodgett technique. Figure 17(b) is a 3D AFM image of 10 layer Fe_3O_4 patterned on graphene sheet. We can see even distribution of Fe_3O_4 NPs except accumulation at the grain boundaries.
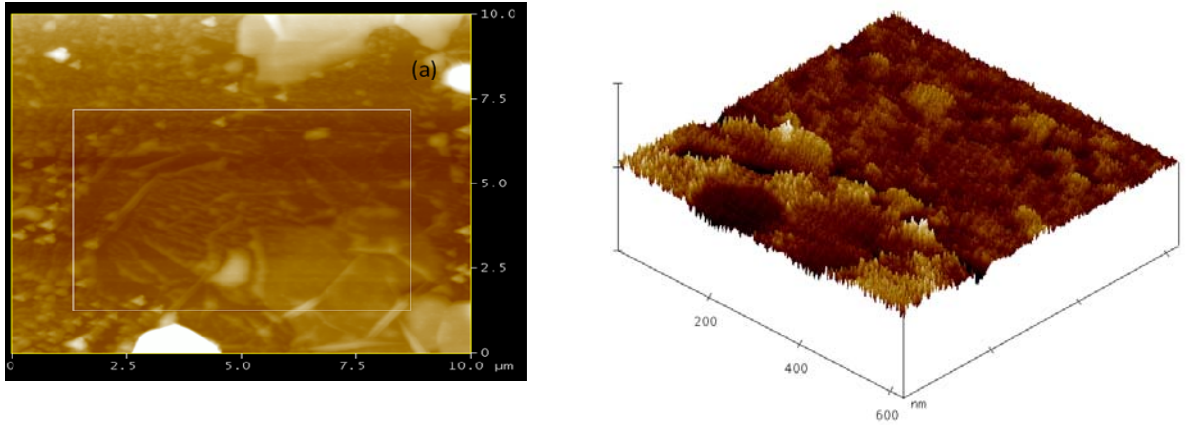

Fig. 17: AFM image of graphene (a) transferred to quartz substrate, (b) 10 layer Fe_3O_4 patterned on graphene.

High quality Fe_3O_4 nanoparticles (Fig. 18a) were prepared by a method similar to the one described by Sun *et. al* .[8]. The average particle size was estimated to be 9 ± 0.5 nm. The
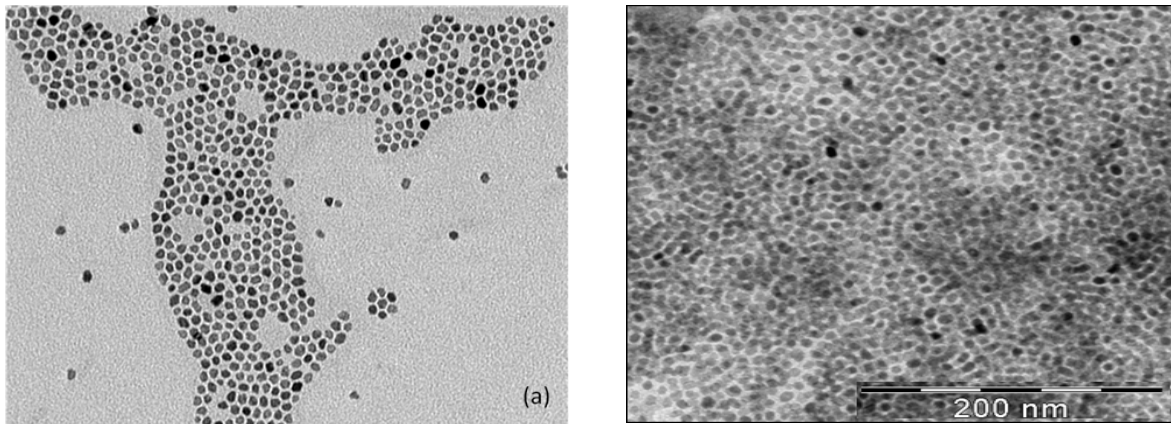

Fig. 18: TEM image of (a) 9nm Fe_3O_4 (b) 10 layer Fe_3O_4 on

nanoparticles prepared were dissolved in hexane and oleic acid and oleylamine were used as surfactants which prevent the agglomeration of the nanoparticles and ensure even dispersion.

We are in the process of measuring the magnetic properties of the graphene-Fe_3O_4 composite and the change in effective anisotropy of the system and spin relaxation time of the nanoparticles on graphene. We expect to see a drop in the blocking temperature and anisotropy with lesser number of layers as the dipolar interactions decrease.

We are also in the process of making graphene-lead selenide(2nm) nanocomposites to look into the optical and transport properties. These results will be reported in the next quarterly report.

(c) Giant Magneto-Impedance (GMI) effect for sensor applications:

Research on soft ferromagnetic materials with giant magnetoimpedance (GMI) effect for making highly sensitive magnetic sensors is of current interest. The overall goal of our research is to investigate the GMI effect in a variety of magnetic materials to explore its potential for applications ranging from magnetic sensors to bio-molecular detection.

Effect of critical length on GMI in magnetic amorphous ribbons:

GMI is a large change in the ac impedance of a ferromagnetic conductor subject to a dc magnetic field. This effect strongly depends on the geometrical dimensions of the samples. However, understanding the sample length (L) dependence of GMI in different types of samples remained incomplete.
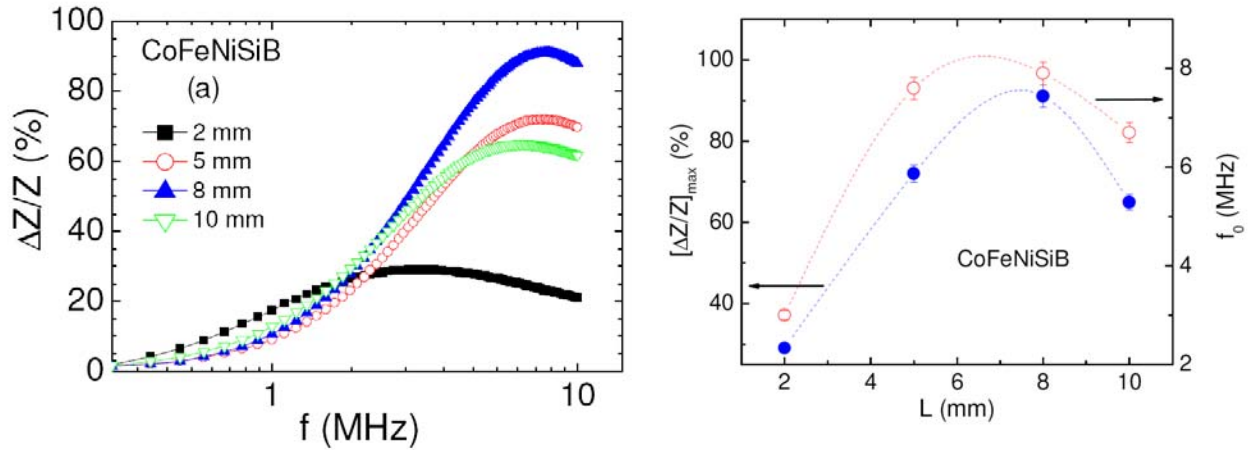

Fig. 19: Frequency dependence of GMI ratio for $Co_{69}Fe_{4.5}Ni_{1.5}Si_{10}B_{15}$ samples with different lengths (left panel). Sample length dependences of maximum GMI ratio and critical frequency.

We have addressed this issue through our systematic studies of the influence of sample length (L = 2, 5, 8, and 10 mm) on the GMI effect and magnetic response (η) in $Co_{69}Fe_{4.5}Ni_{1.5}Si_{10}B_{15}$ amorphous ribbons over a frequency range of 0.1 − 10 MHz. As shown in Fig. 19, we demonstrate the existence of a critical length ($L_0 \cong 8$ mm), where the largest GMI effect is achieved. Below the critical length ($L < L_0$), the GMI effect decreases with decreasing

sample length, resulting from the formation of closure domain structures near the ends of the sample due to the demagnetization effect. Above the critical length ($L > L_0$), the GMI effect increases with decreasing sample length and this can be attributed to the decrease of electrical resistivity. In addition, the critical frequency (f_0) reaches the largest value for samples with $L = L_0$ and shifts to lower values for samples with $L < L_0$ and $L > L_0$. These findings point to the importance of the geometrical dimensions of samples for optimizing GMI effect for making highly sensitive GMI-based magnetic sensors. The results have been published in Materials Science and Engineering B in 2010 (*Materials Science and Engineering B 172, 146 (2010)*)

Correlation between the magnetic softness and GMI effect in magnetic ribbons:

A relationship between the soft magnetic properties and GMI effect has been established in $Co_{69}Fe_{4.5}R_{1.5}Si_{10}B_{15}$ (R = Ni, Al, Cr) amorphous ribbons. Our studies have shown that the high value of transverse anisotropy is needed for obtaining large values of GMI in the high frequency range. The surface roughness plays an important role in the high frequency range, where the skin effect is strong and the skin depth is small approximately to magnetic irregularity. This provides a good guidance on developing GMI materials for high frequency magnetic sensor applications. These results have been published in Physica B: Condensed Matter in 2010 (*Physica B: Condensed Matter 405, 2836 (2010)*. Some representative results are shown in Fig. 20.
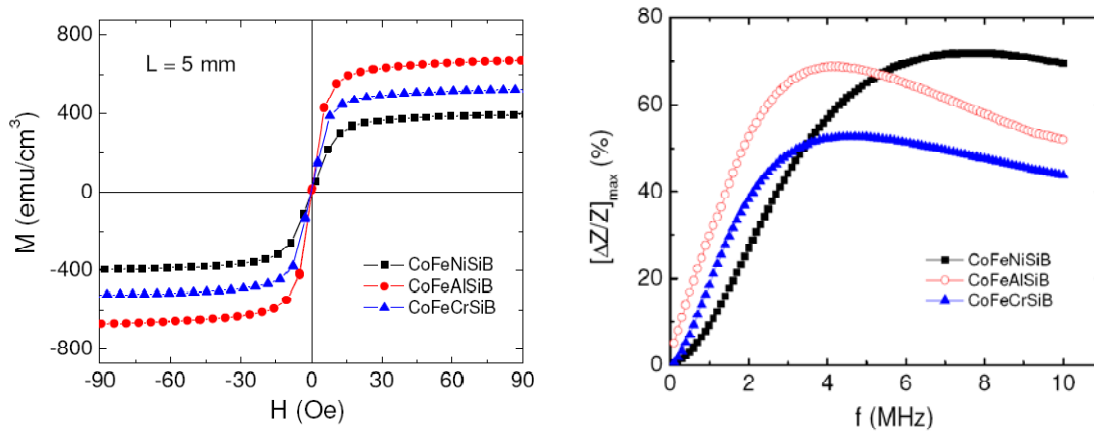

Fig. 20: shows magnetic hysteresis loops (left panel) and frequency dependence of maximum GMI ratio (right panel) for the $Co_{69}Fe_{4.5}R_{1.5}Si_{10}B_{15}$ (R = Ni, Al, Cr) samples.

Giant magneto-impedance as a biosensor:

Ferrofluids are potentially important materials for biomedical applications, such as cancer treatment either by hyperthermia using the change of magnetization in an AC magnetic field to heat the tissue, or by drug targeting. In this case, it is necessary to use an external magnetic field to sense cells that have taken up magnetic nanoparticles.

We demonstrate the possibility of using GMI as a biosensor. We have studied the GMI effect in Co-based magnetic ribbons with and without Fe_3O_4-based ferrofluid over a frequency range of 0.5 Hz – 13 MHz. The GMI effect has been found to be sensitive to magnetic signals coming from magnetic nanoparticles on top of the ribbon. The effect is only significant at high frequency where the skin effect is strong (Fig. 21). Overall, the high-frequency GMI technique can be used as a biosensor for biomedical applications such as bio-molecular detection.

Our current efforts are to develop new GMI material systems with improved GMI effect and sensitivity. For instance, we are fabricating and investigating the GMI effect in magnetic ribbon/metal bilayer and multilayer structures using sputtering. We are also studying the effect of layers of nanoparticles patterned on magnetic ribbons on GMI for biosensor applications.

Fig. 21: Frequency dependence of maximum GMI ratio and the inset shows the magnetic field dependence of GMI ratio.

[B] Functional materials for affecting cell attachment and proliferation

This project is an investigation of the combined effects of physical and biochemical stimuli on adhesive mammalian cells *in vitro*. Polypeptide multilayer films provided a means of controlling substrate charge, viscoelasticity, and functionalization. Adhered collagen I (CI)-derived peptides and soluble vascular endothelial growth factor (VEGF) represented means of controlling exposure of cells to specific biochemical cues. All polymers utilized for film fabrication were produced synthetically; VEGF was recombinant. This work focused on human umbilical vein endothelial cells (HUVECs) as a model cell type.

HUVECs are commonly employed in physiopharmacological investigations such as bioactive-molecule transport, blood coagulation and fibrinolysis [9-11]. These cells respond to cytokine concentration, cell adhesion molecule surface density, and other environmental stimuli [12-14] Under some conditions, proliferative cell morphology can be transformed into tubular structures, as in neovascularization, a usual prerequisite for tumor progression [15,16]. HUVEC culture conditions are thus determinative of cell fate.

Responses of cells to mechanical properties of the adhesion substrate have been investigated for many years [17-21]. Such studies have shown that adherent cells tend to spread more, adhere better, and survive longer on comparatively stiff substrates. Similar tendencies have been found for polyelectrolyte multilayer film-coated materials [22]. Multilayer films made of polyaminoacids (e.g., PLL) and polysaccharides (e.g., chitosan) show poor cell adhesion or anti-adhesion if the films are "thick", i.e., consist of more than 12 "layers" [22-25]. Surprisingly, the present study has revealed that HUVECs adhere less to multilayer films of any thickness than tissue-culture poly(styrene) (TCPS), despite the apparent greater similarity of a polypeptide multilayer film than TCPS to the extracellular matrix. HUVECs also appear to proliferate rapidly on TCPS than the films.

Cell adhesion:

Fig. 22 shows HUVEC adhesion on various PLL/PLGA films after 1 day of culture in serum-containing medium. Varying the number of polypeptide adsorption steps led to differences in HUVEC behavior. Specifically, cell adhesion decreased on increasing the number of adsorption steps (decreasing substrate rigidity). The buildup of PLL/PLGA proceeded exponentially (Fig. 23), similar to various reported polyelectrolyte systems [26-30]; film
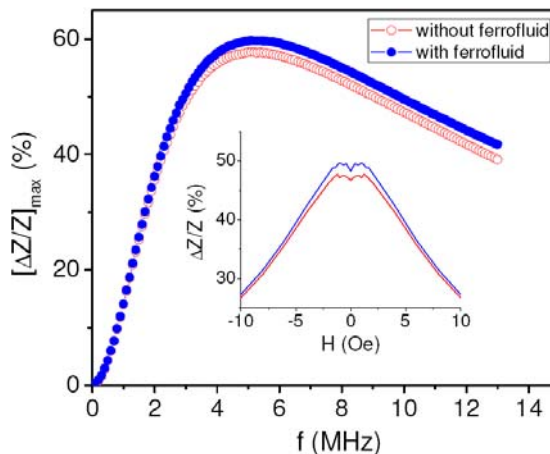
thickness increased with the number of adsorption steps. As expected, thicker films were softer than thinner films (Fig. 24).
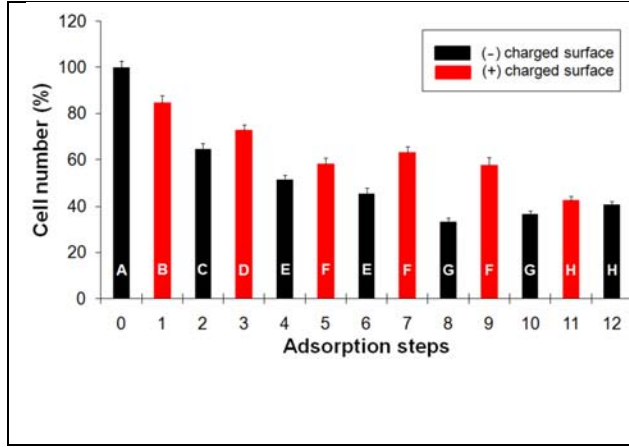

Fig. 22: HUVEC proliferation on various non-functionalized PLL/PLGA multilayer films after 1 day in culture. Cell number is shown as the number of HUVECs on films relative to the number of cells on TCPS in the *absence* of $VEGF_{165}$. Bar shading indicates film surface polarity. The seeding density was 5×10^3 cells/well in the presence of 2% (v/v) fetal bovine serum. Cell number was quantified with CyQuant®. Letters A-H indicate a significant difference in cell number from the other groups with $p < 0.05$.
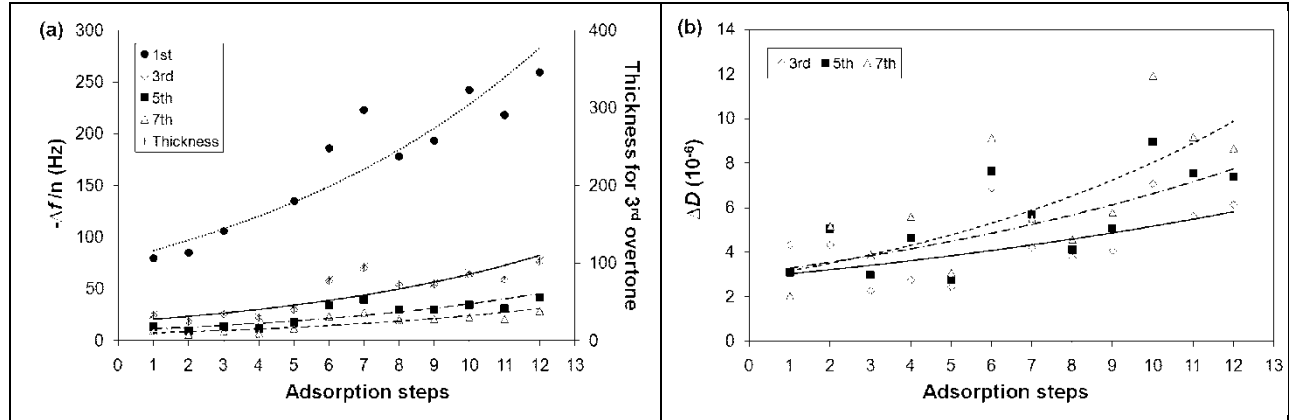

Fig. 23: Film buildup as monitored by QCM-D. (a) Measured frequency shift ($-\Delta f/n$) for different overtones and calculated hydrated film thickness for the 3rd overtone (eq. 2) as a function of PLL/PLGA film buildup, (b) measured dissipation shift (ΔD) for different overtones. All lines are fits of an exponential model to empirical data points. The fundamental frequency was 5 MHz; the overtones were 15 MHz, 25 MHz and 35 MHz.

Cell behavior on a given substrate is well known to depend heavily on cell type. Nevertheless, HUVEC attachment to 7-adsorption-step poly-(D-lysine)/PLGA films ($78 \pm 10\%$), reported by Boura et al. (2003), resembles attachment to 7-adsorption-step PLL/PLGA films in this work ($63 \pm 7\%$ relative to TCPS). The first polymer 5 adsorption steps in the Boura et al. work consisted of one precursor layer of poly(ethylenimine) followed by two bilayers of poly(sodium 4-styrenesulfonate)/ poly(allylaminehydrochloride). The "5-layer" film was then coated with poly-(D-lysine) and PLGA. Surprisingly, Boura et al. found that cell count had increased after 3 days in culture relative to TCPS, despite decreased rigidity relative to the corresponding PLL/PLGA film substrate in this work. The difference from the present results can perhaps be ascribed to film architecture. Films made of strong polyelectrolytes tend to be stiffer and thinner per adsorption step than ones made of weak polyelectrolytes like PLL and PLGA [31,32]. Nevertheless, the present data make it difficult to understand how HUVECs could display increased proliferation on a less rigid substrate after 1 day of culture. Several
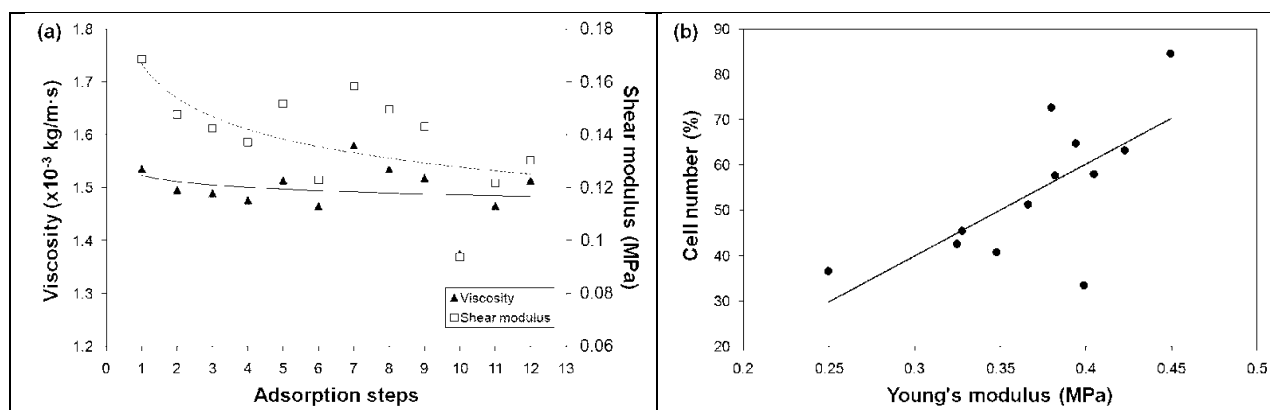
Fig. 24: Mechanical properties of various non-functionalized PLL/PLGA films and their relationship to HUVEC proliferation. (a) Viscosity and shear modulus and (b) the relationship of Young's modulus to cell proliferation. Data from the 5th and 7th overtones were used for viscoelasticity modeling. Cell number is shown as the number of HUVECs on films with respect to the number of cells on TCPS in the *absence* of VEGF after 1 day in culture (Fig. 22). All curvilinear lines are visual aids. The straight line in panel (c) was obtained by regression analysis.
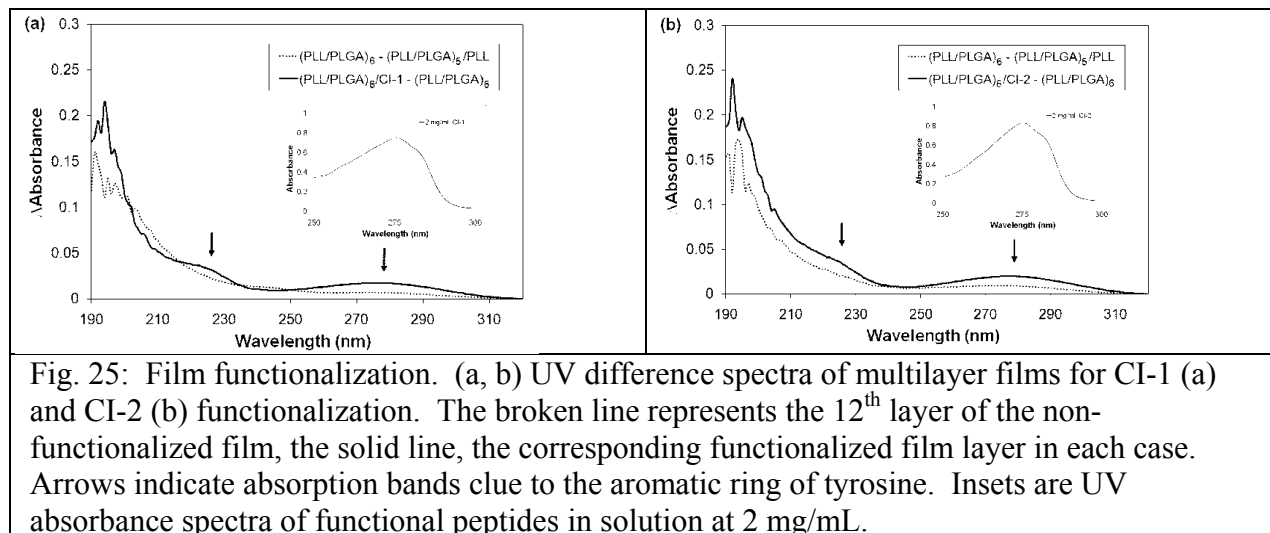
studies have increased multilayer film rigidity by covalent crosslinking, for instance, by EDC and sulfo-NHS chemistry [23, 25,33-35]. Stiffer substrates have consistently promoted cellular attachment and growth, despite the greater similarity of a polyelectrolyte multilayer film than TCPS to key properties of the extracellular matrix.

PLL-ending films gave greater cell proliferation than PLGA-ending films in the presence of serum. The result may be explained by the sign of the surface charge. Richert et al. (2002) found that chondrosarcoma cells bound more strongly to films with a positive (PLL) surface than a negative (PLGA) surface in a serum-free environment. Although the zeta potential of PLL-ending films decreased after exposure to serum-containing medium, cell attachment to PLL-ending films was still higher than for PLGA-ending films. Ideally, one could dissect the binding affinity of cells from the number of sites, an extensive quantity and site occupancy. In Kim et al. (2009), HUVEC attachment to a polyelectrolyte hydrogel increased on increasing the positive charge concentration [36]. Hydrogel, even if highly charged, is obviously more flexible than TCPS. A similar tendency was found when a negatively charged polyurethane membrane was coated with a positively charged polyelectrolyte [37]. HUVECs anchored to the substrate and spread well when the substrate surface charge was changed from negative to positive.

Film functionalization:

Multilayer films have been functionalized with specific biochemical signals by different investigators in different ways. One approach has been to conjugate a short peptide to a long polymer (e.g., PLGA), and to adsorb the resulting branched structure onto the film surface [22,33,35]. For example, a 14-amino-acid peptide containing the laminin-5 sequence or a 15-amino-acid peptide containing the RGD sequence of fibronectin have been grafted to PLGA with the crosslinking reagents EDC and sulfo-NHS. Film functionalization resulted from a subsequent grafted-polymer adsorption step. A downside of the approach is the need for conjugation and separation steps. The present study took a simpler route. 12 lysine residues at the N-terminus of designed peptides CI-1 and CI-2, which are based on collagen I, were for

binding to a negatively charged surface. The functional regions of the same peptides were for increased control over cell adhesion and proliferation. Film functionalization was achieved by LBL, the same process used to make the underlying film. No peptide grafting or corresponding separation step was required. The UV absorption data shown in Fig. 25 indicate that the functional peptides remained bound to the film at equilibrium subsequent to several rinse steps. Such functional peptides can be adsorbed onto virtually any oppositely-charged surface, regardless of film architecture or surface roughness. Moreover, the peptides are readily utilized

Fig. 25: Film functionalization. (a, b) UV difference spectra of multilayer films for CI-1 (a) and CI-2 (b) functionalization. The broken line represents the 12th layer of the non-functionalized film, the solid line, the corresponding functionalized film layer in each case. Arrows indicate absorption bands clue to the aromatic ring of tyrosine. Insets are UV absorbance spectra of functional peptides in solution at 2 mg/mL.

individually or in combination and under considerable control over a broad range of surface densities and molar ratios.

The data show that film functionalization with CI-1 and CI-2 had a significant impact on adhesion and other aspects of cell behavior. There was at least 25% increase in HUVEC adhesion after 2 h of culture (Fig. 26). The GFPGER sequence, included in peptide CI-1, corresponds to a high-affinity binding site in collagen type I and IV for integrin $\alpha_2\beta_1$ and in collagen type I for $\alpha_1\beta_1$ [38]. GFPGER-peptide coatings have previously been employed to elicit a specific osteogenic cellular response and promote bone tissue ingrowth into scaffolds [39, 40]. Bone formation occurred significantly faster on GFPGER-coated scaffolds than uncoated scaffolds in the absence of exogenous growth factors [32]. A GFPGER peptide has also been found to increase HUVEC attachment and spreading on stiff polyacrylamide gels [41]. GTPGPQGIAGQRGVV (P15)-coated materials have been shown to enhance cell adhesion and proliferation *in vitro*. P15 promoted the growth of primary HUVECs and the proliferation of endothelial cells on P15-treated expanded polytetrafluoroethylene (ePTFE) grafts compared to untreated controls. [42] The GTPGPQGIAGQRGVV sequence motif was included in peptide CI-2.
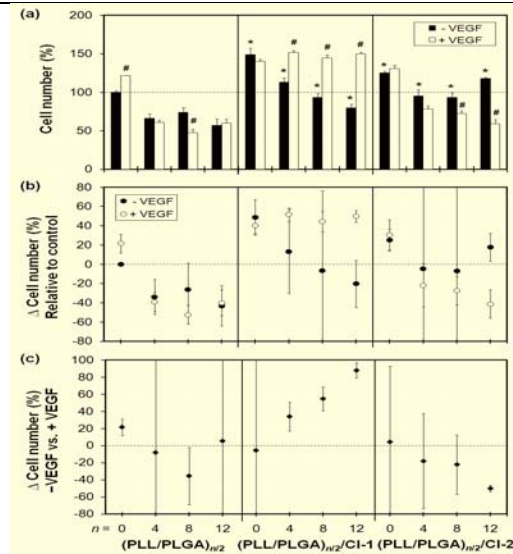
Fig. 26: Short-term HUVEC adhesion on functionalized films. Cells were incubated 2 h in culture medium on different film architectures. (a) HUVEC cell number adhered to various substrates, (b) HUVEC adhesion difference relative to TCPS in the *absence* of $VEGF_{165}$ and (c) VEGF effect on cell adhesion after 2 hr incubation. TCPS and 4-, 8- and 12-adsorption-step films, which have a negative surface charge, were functionalized with CI-1 or CI-2 as in Fig. 4. Black bars represent cells cultured in the absence of $VEGF_{165}$; white bars, with $VEGF_{165}$. The seeding density was 3×10^4 cells/well. An asterisk (*) indicates a significant difference in proliferation between the functionalized film and the corresponding non-functionalized film with $p < 0.05$. A pound sign (#) indicates a significant difference between the *presence* and *absence* of $VEGF_{165}$ in culture medium with $p < 0.05$.

Despite initial enhancement of attachment on CI-1- or CI-2-functionalized PLL/PLGA films, HUVEC density decreased with time (Fig. 27). Only a few cells remained after 7 days in culture. Increasing the number of adsorption steps resulted in somewhat fewer cells adhered after 1 day in culture and a dramatic decrease in cell density after 7 days. On TCPS, by contrast, cells proliferated and became confluent with time, with or without functional peptide coatings. It therefore appears that substrate stiffness had a greater effect on cellular behavior on the films than the chemical stimulus provided by the functional peptides.

It has been suggested that the spacing between a peptide sequence and its anchoring moiety could influence functionality [43]. Presumably, a specific attachment peptide will have to be sufficiently prominent on a substrate surface to attach to the corresponding cell receptor. Here, the lysine residues of the attachment region of designed peptides will have formed a complex with PLGA molecules on the film surface. There was a 9-residue "linker" $((GPO)_3)$ between the film and the functional region of CI-1, and no linker in CI-2. The present results may therefore be attributable to linker length in some measures. Examples are known of effective cell adhesion in the absence of a linker in an RGD peptide [44], and increasing linker length has been found to reduce cell attachment [45]. Picart et al., using a 15-amino-acid RGD peptide (CGPKGD***RGD***AGPKGA), found improved osteoblast adhesion on functionalized 12-adsorption-step PLL/PLGA films [33]. The same study found that film crosslinking had a comparable effect to biochemical functionalization on cell adhesion. It therefore seems that no definite conclusion can be reached at this time, concerning the linker length and the adhesion data of the present work.

Exponential growth of multilayer films is well known for different polyelectrolyte systems [26-30, 46]. It is probable that the number of functional peptide binding sites increases
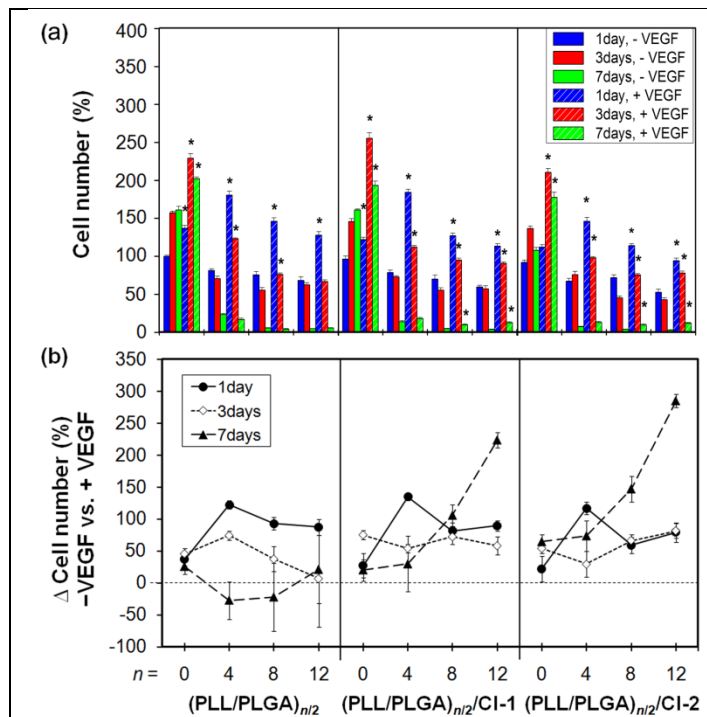

Fig. 27: Long-term HUVEC proliferation on multilayer films. (a) HUVEC adhesion after 7 days relative to TCPS in the *absence* of $VEGF_{165}$ and (b) VEGF effect on cell adhesion over time. TCPS and 4-, 8- and 12-adsorption-step films were functionalized with CI-1 or CI-2. The seeding density was 3×10^4 cells/well. An asterisk (*) indicates a significant difference for cells without and with $VEGF_{165}$ in culture medium with $p < 0.05$.

with film thickness in such cases. One might therefore expect a greater surface density of functional peptides on 12-adsorption-step than 4- or 8-adsorption-step PLL/PLGA films. In the present work, nevertheless, there was no clear difference in peptide-specific biochemical effects for the various film thicknesses. The reasons are uncertain. Future experiments could increase the emphasis on known details of receptor-ligand interactions.

The effects of $VEGF_{165}$ in this work cannot be distinctly separated from the effects of substrate mechanics and chemical signaling. VEGF had inconclusive impact on the short-term adhesion of HUVECs on the various multilayer systems. While film functionalization with CI-1 and CI-2 improved cell adhesion, synergism of the film-bound biochemical signals with soluble VEGF is less certain. Cells on CI-2-functionalized films showed similar trends with regard to adhesion as non-functionalized films and bare TCPS, whereas cells on CI-1-functionalized films displayed a significant increase in cell numbers on films in the presence of VEGF (Fig. 26).

Fig. 27 shows how VEGF affected HUVEC proliferation over 7 days in culture. In general, this endothelial cell-specific mitogen and angiogenic factor [47-49] increased cell survival after 1 day in culture. VEGF is well known to regulate endothelial cell survival, proliferation, migration and differentiation. Nevertheless, there was little evidence that VEGF influenced HUVEC proliferation beyond the first day of culture. It seems probable that more cells remained at later time points in VEGF-treated cell populations because of increased initial cell adhesion after 1 day of culture, not because of effects of VEGF on adhered cells. In any case, soluble VEGF is a means of controlling cell behavior on multilayer films.

Cell morphology and cytoskeletal organization:

A qualitative comparison of cell morphology and cytoskeletal organization was done to gain further information on possible synergistic effects of mechanical stimuli, substrate-bound biochemical stimuli and soluble biochemical stimuli (Fig. 28-30). That endothelial cells are

mechano-sensitive is well known. In 2- and 3-dimensional models of *in vitro* angiogenesis, capillary-like structures are favored on or in more flexible substrates [50-52].
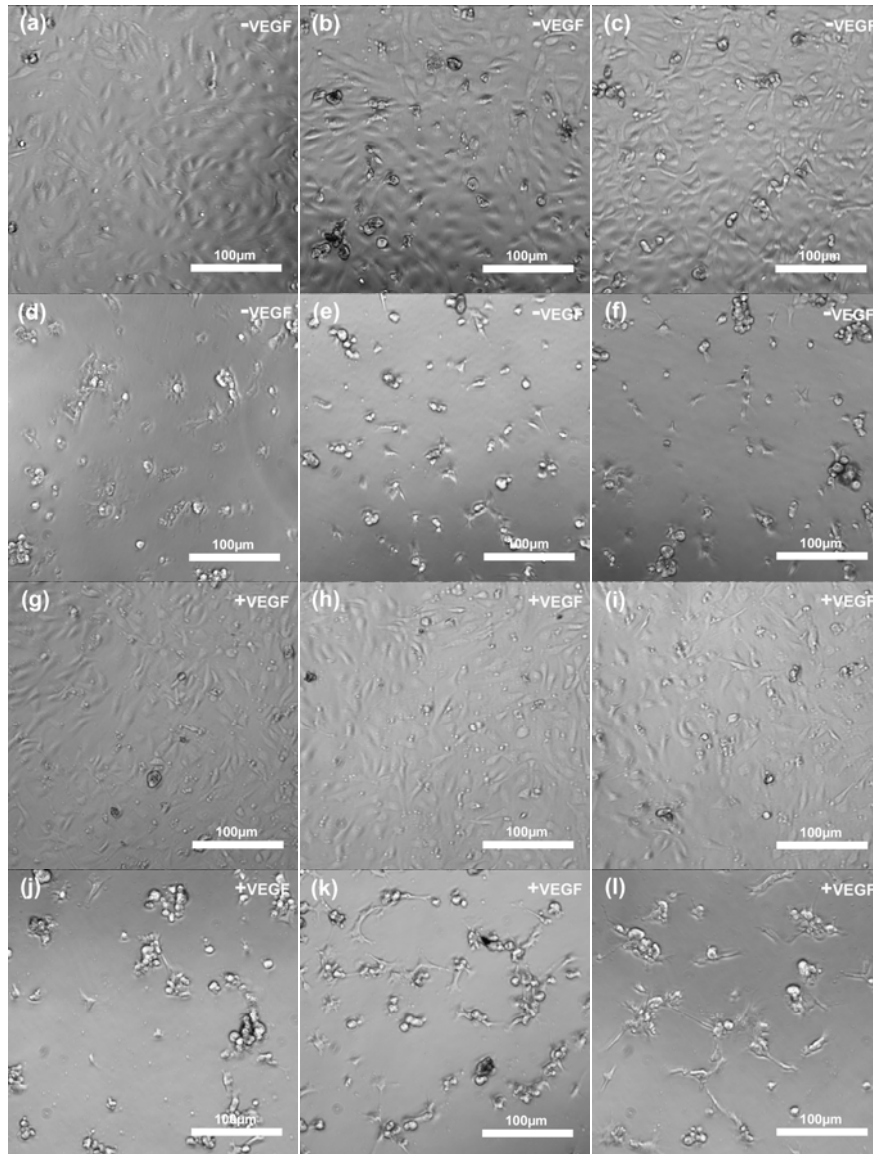

Fig. 28: HUVEC density and morphology on multilayer films after 1 day in culture. The films were built on a 96-well plate. The seeding density was 3 x 10^4 cells/well on (a, g) TCPS, (b, h) CI-1-functionalized TCPS, (c, i) CI-2-functionalized TCPS, (d, j) 12-adsorption-step, non-functionalized films, (e, k) CI-1-functionalized 12-adsorption-step films, and (f, l) CI-2-functionalized 12-adsorption-step films. VEGF$_{165}$ was absent (a-f) or present (g-l) in the culture medium. The phase contrast images were obtained at a magnification of 10×. Scale bars, 100 μm.

Saunders et al. have reported stable network formation by HUVECs on gels with a Young's modulus of 140 Pa, whereas gels with a Young's modulus of 2.5 kPa supported cell attachment but showed no cell organization into vascular networks, with or without VEGF and basic fibroblast growth factor [41]. Under the cell culture conditions of this work, for which Young's modulus was close to 0.4 MPa, HUVECs did not form vascular networks on non-functionalized or functionalized 12-adsorption-step films, regardless of VEGF treatment (Fig. 28(d-f)). Nor was there evidence of angiogenesis, nevertheless, HUVECs did seem to migrate, especially on functionalized films in the presence of VEGF (Fig. 28(j-l)). VEGF-stimulated migration may decrease the stability of cell networks, as it leads to crawling along adjacent cells or stretching/moving [41]. If the cell density is relatively low, as on the 12-adsorption step films of the present study, cells are all the less apt to form a network assembly [53].

VEGF-stimulated cell migration is associated with regulation of the cytoskeleton and long and highly structured actin stress fibers [46-48]. As shown in Fig. 29, VEGF-treated cells displayed long and condensed stress fibers reaching into the cell body. VEGF had a striking effect on cells cultured on 12-adsorption-step films: fibers were disorganized throughout the cells on non-functionalized and on functionalized films in the absence but not the presence of VEGF (Fig. 29(g-i)). VEGF is also known to induce cell edge ruffling [46]. In the present work, VEGF-untreated groups showed more edge ruffles on multilayer films than TCPS, consistent with the view that effects due to substrate mechanical properties dominated effects due to VEGF. The immune-cytochemistry data show that the distribution of vinculin, a focal adhesion protein, correlated with substrate stiffness. For VEGF-treated HUVECs on non-functionalized or functionalized 12-adsorption-step films, vinculin was irregularly distributed throughout the cell, despite the presence of actin filament bundles. As before, although VEGF influenced the reorganization of actin filaments, it would appear the mechanosensitivity of HUVECs was greater than their responsiveness to the soluble growth factor, and that focal adhesion stability decreased with decreasing film stiffness. The present data are consistent with other studies [17,18].
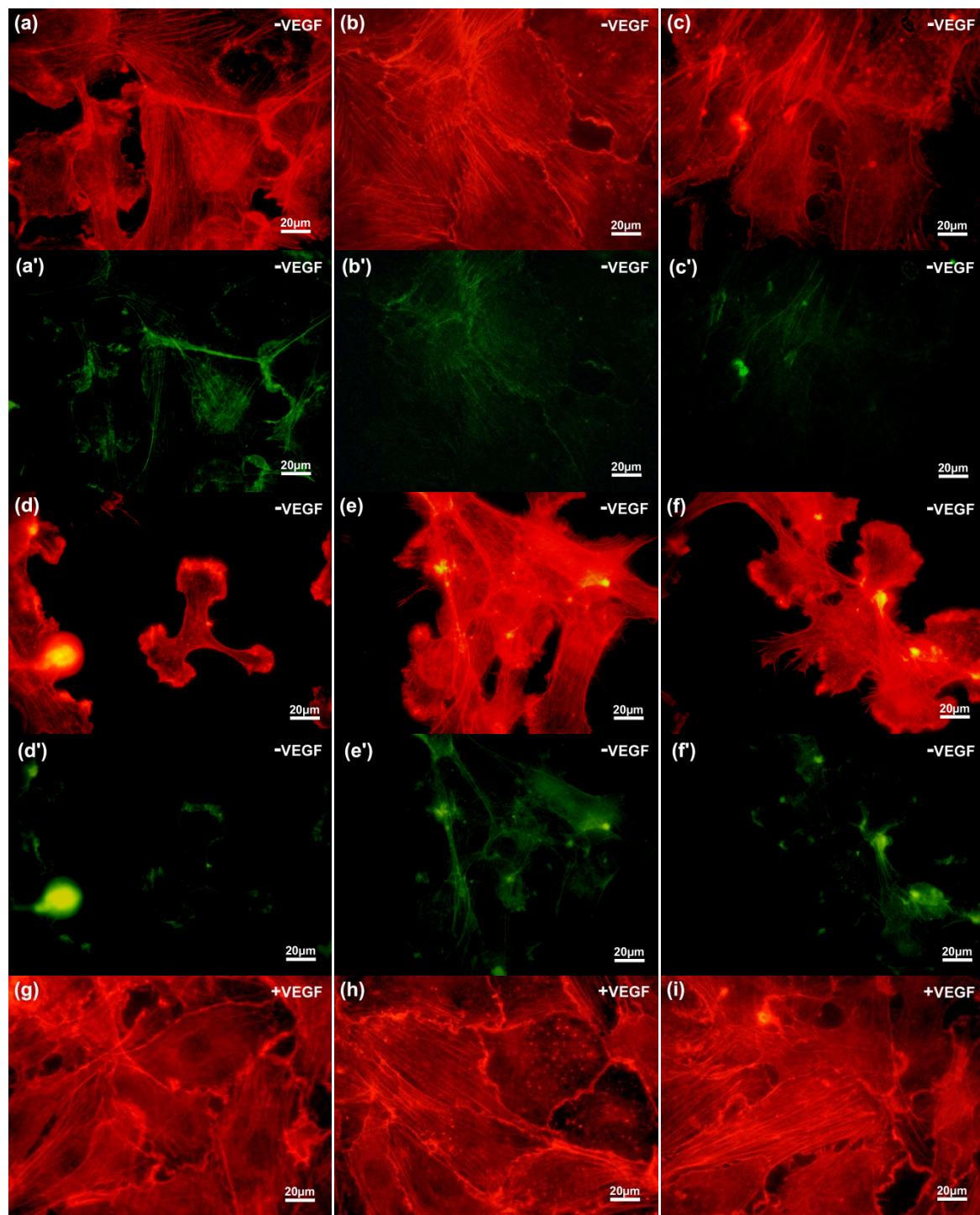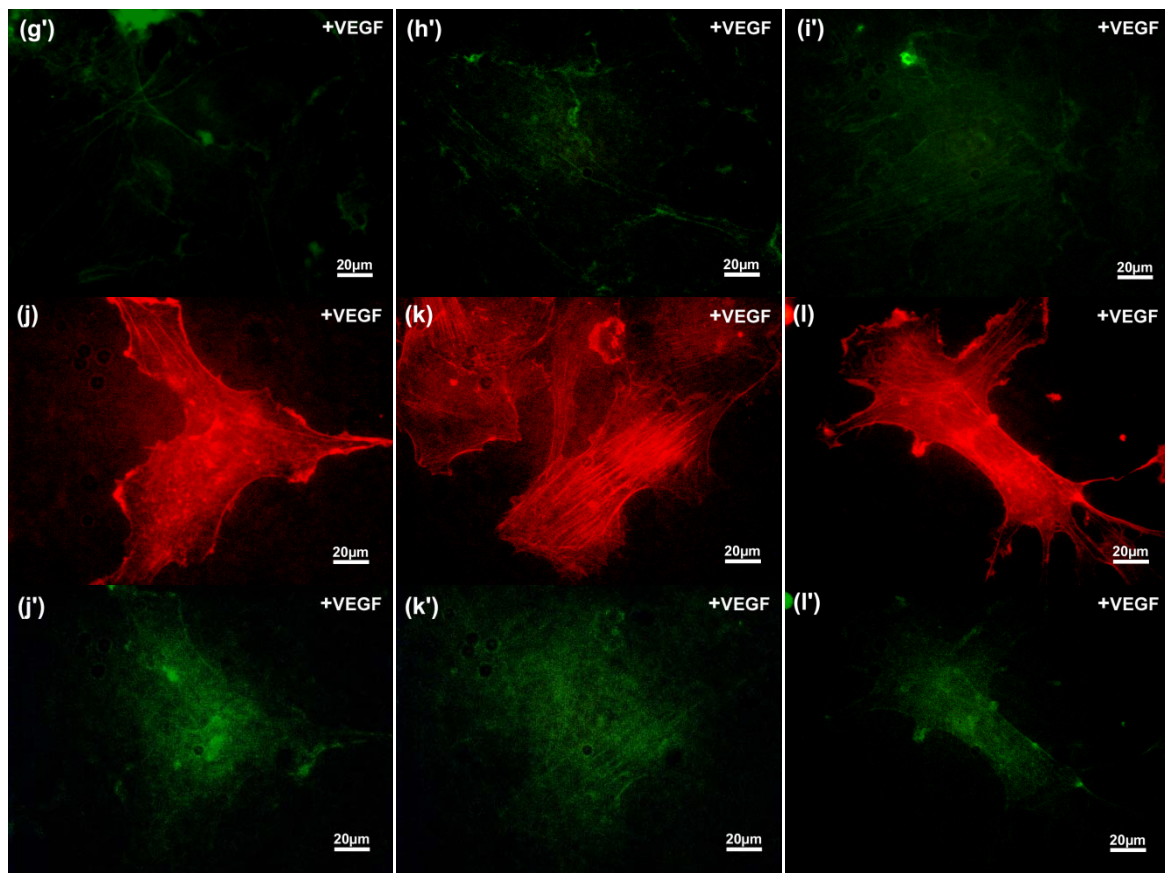
Fig. 29: F-actin organization and distribution of vinculin in HUVECs on multilayer films after 1 day in culture. The films were built on microscope cover glass. The seeding density was 1×10^5 cells/cover glass on (a, a', g, g') TCPS, (b, b', h, h') CI-1-functionalized TCPS, (c, c', i, i') CI-2-functionalized TCPS, (d, d', j, j') non-functionalized 12-adsorption-step films, (e, e', k, k') CI-1-functionalized 12-adsorption-step films, and (f, f', l, l') CI-2-functionalized 12-adsorption-step films. Cells were stained with (a-l) rhodamine phalloidin or (a'-l') FITC-labeled anti-vinculin for visualization of microfilaments or focal adhesions, respectively. VEGF$_{165}$ was absent (a-f, a'-f') or present (g-l, g'-l') in the culture medium. Scale bars, 20 μm.

Finally, although substrate mechanical properties dominated over biochemical stimuli with regard to cell adhesion, it appears that VEGF influenced VE-cadherin abundance in cell-cell junctions (Fig. 30). An apparent locomotive effect of VEGF on cells was correlated with a decreased abundance of cell-cell junctions. A cytoplasmic target of VE-cadherin is α-catenin, which is related to F-actin [57, 58]. Details of the relationship between the abundance of cell-cell junctions and vinculin distribution will be discussed elsewhere.
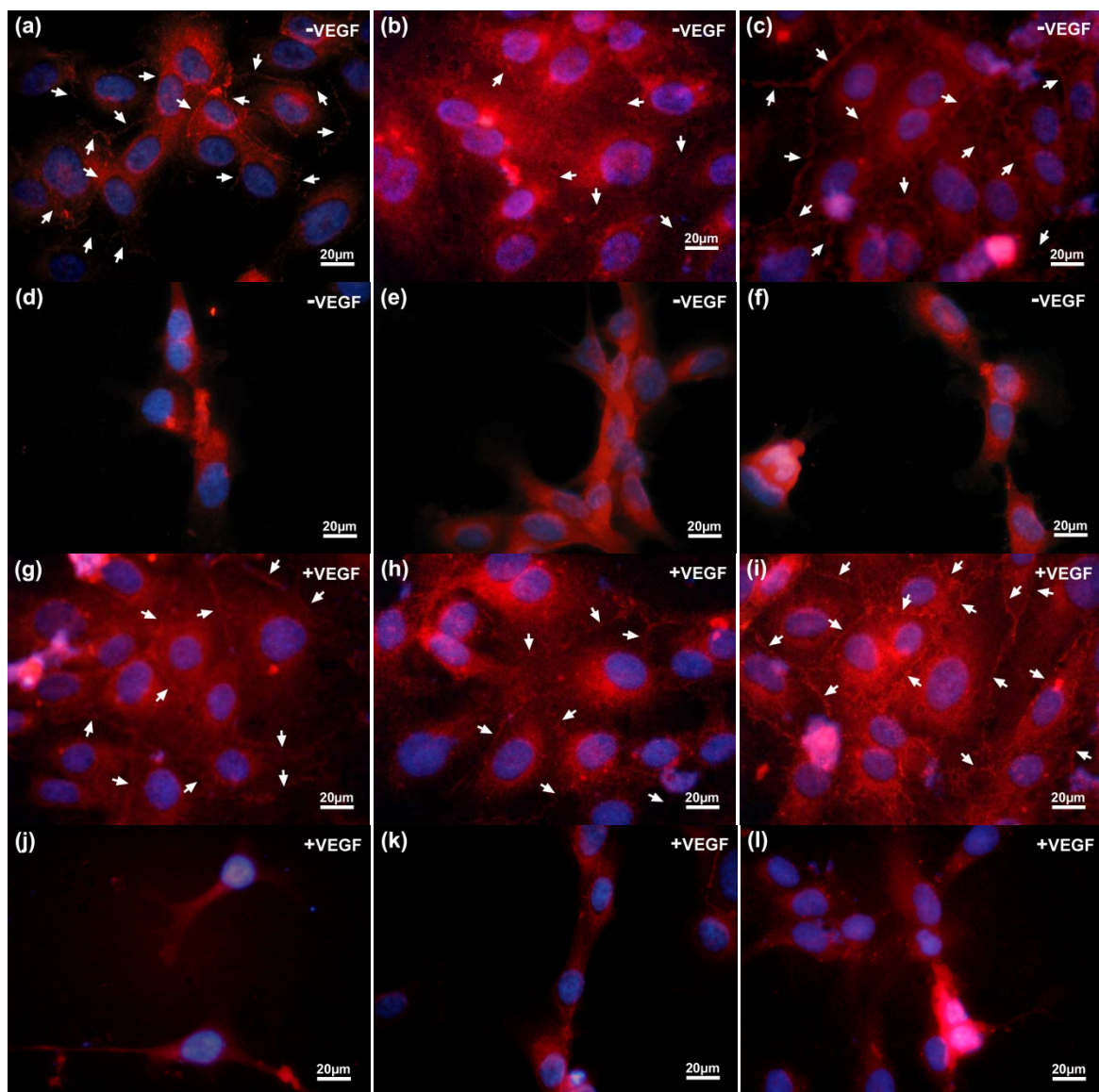
Fig. 30: VE-cadherin-mediated cell-cell adhesion in HUVECs on multilayer films after 1 day in culture. The films were built on microscope cover glass. The seeding density was 1×10^5 cells/cover glass on (a, g) TCPS, (b, h) CI-1-functionalized TCPS, (c, i) CI-2-functionalized TCPS, (d, j) non-functionalized 12-adsorption-step films, (e, k) CI-1-functionalized 12-adsorption-step films, and (f, l) CI-2-functionalized 12-adsorption-step films. Cells were stained with anti-human VE-cadherin/CD144-PE and DAPI for visualization of adhesion contacts and cell nuclei, respectively. $VEGF_{165}$ was absent (a-f) or present (g-l) in the culture medium. Arrows indicate VE-cadherin staining at cell-cell junctions. Scale bars, 20 μm.

Conclusion:

Multilayer films provide a means of controlling the mechanochemical properties of the substrate for cell culture. Mechanical stimulation was achieved by changing film thickness and stiffness. Films were also functionalized by adsorbing collagen type I-derived peptides onto the surface. $VEGF_{165}$ served as a soluble biochemical stimulus. Whereas primary HUVECs adhered

poorly on all non-functionalized PLL/PLGA multilayer films in comparison to TCPS, functionalization increased adhesion in short-term culture. After 7 days in culture, however, cell density was lower on films than on TCPS, even with functionalization, even though VEGF stimulated cell growth during 1 day in culture. The mechanical properties of multilayer films therefore appear to have had a more significant long-term effect than the biochemical signals in this work. VEGF enhanced initial cell survival and stress fiber formation on films. In addition, HUVECs appeared more mobile on the softer films in the presence of VEGF. This study specifically focused on HUVEC response to the combined effects of film functionality and mechanical properties, with or without a soluble growth factor. The same mechanochemical stimuli could be applied to many other cell types, and the stimuli used here could easily be changed. The general approach is therefore a relatively straightforward means of probing the response of a cell to a controlled and specific cellular environment. The film functionalization procedure employed here is simpler than the grafted polymer approach. A strictly designed multilayer film system of mechanochemical properties could also be employed in the diagnosis of disease, perhaps in cancer research. The cellular activity, morphology and malfunction can be identified under the strict conditions.

Task II: Multifunctional composites for communication and energy applications

[C]   Tunable multifunctional nano- and heterostructures for RF and microwave applications

(a) Optimization of PZT film growth process and PZT (ferroelectric)/CFO (ferromagnetic) heterostructures:

Compensating lead depletion in PZT thin films using dual laser system:

We have investigated the Pb depletion in laser ablated PZT ($PbZr_{0.52}Ti_{0.48}O_3$) films through a systematic study of PZT target-laser interactions for both single laser and dual-laser ablation methods. The study includes films deposited from a stoichiometric and an excess PbO PZT targets. The films were deposited on single crystal $SrTiO_3$ [100] substrates at 550°C with a background oxygen pressure of 500 mT. Single laser deposited films at a laser fluence of $5J/cm^2$ produced the highest Pb content while dual-laser ablated films where an excimer and a CO_2 pulsed lasers were synchronized for ablation produced high Pb content for an excimer laser fluence of less than $2J/cm^2$. This enabled the growth of particulate-free PZT films with high Pb content. ICCD imaging of the plasma plumes showed variations in the expansion profiles at different laser fluencies that correlated well with the Pb content observed in the deposited films.

Introduction:

Pulsed laser deposition (PLD) technique offers unique advantages in the growth of thin films of multi-component ferroelectric materials such as PZT ($PbZr_{0.52}Ti_{0.48}O_3$). The most promising characteristics of the PLD technique is the stoichiometric transfer of materials from the target to the substrate. However, for oxides such as PZT which involve volatile elements like Pb, ablation of stoichiometric PZT targets causes preferential evaporation of Pb from the target at low laser fluences. In addition, Pb depletion in films was observed for typical growth temperatures of 500°C to 600°C necessary for getting crystalline films [59]. This Pb deficiency is responsible for the coexistence of a pyrochlore phase with the perovskite PZT phase, degrading the ferroelectric properties of the films. To compensate for the Pb loss it is a general practice to add excess PbO during the preparation of the dense ceramic PZT targets. Our investigations have shown that the preferential evaporation of Pb from target is suppressed at high laser fluences, but with the undesirable increase in the particulate density. On the other hand the advantages of growth of multi-component materials using dual laser ablation had been demonstrated earlier [60]. In this work we report the effectiveness of the dual laser ablation technique in producing particulate free high Pb content PZT films. Not only have the films grown by dual laser ablation retained the crystalline quality and high Pb content like the high excimer fluence single laser ablated films but also there has been a reduction in particulates on film surface.

Experimental details:

The dual laser ablation system used in our experiments has been described in detail elsewhere [61]. Briefly, a 20-ns FWHM KrF laser pulse at 248 nm overlapped a 200-ns FWHM CO_2 laser pulse of wavelength 10.6 μm at the target. Two targets, namely a stoichiometric PZT

target and a PZT target with 30 at. % excess PbO were prepared by standard ceramic procedures. First, the prepared targets were irradiated by 1000 laser pulses for various fluences with a background oxygen pressure of 500 mT using both single and dual laser ablation. After ablation, the surface morphologies and the compositions of the laser target interaction sites were examined by scanning electron microscopy (SEM) and X-ray energy dispersive spectroscopy (EDS). Time gated intensified charge-coupled detector (ICCD) images of the generated plasma plumes during ablation were captured for both ablation processes at the various laser fluences. The plume emission was collected normal to the propagation direction. The films were deposited on single crystal $SrTiO_3$ [100] substrates at 550˚C with a background oxygen pressure of 500 mT. The prepared thin films were measured by X-ray diffraction (XRD) for crystal structure. All XRD measurements were carried out with Cu Kα radiation using Bruker D8 Focus X-ray Diffractometer. The film surfaces were studied using Digital Instruments D 3100 atomic force microscope (AFM).

Results and discussion:

Laser-target interactions:

Figure 31 shows the XRD scans for the two PZT targets. Both the scans match the tetragonal $PbZr_{1-x}Ti_xO_3$ phase with x=0.48 with no other observed impurity phases besides PbO.

Figure 32 shows the SEM images of single laser target interaction sites on the PZT (30 at. % excess PbO) target surface after irradiation by 1000 pulses of the excimer laser with a range of laser fluences from 1-5 J/cm^2. We observed severe surface melting and formation of columnar structures. Two kinds of cones can be identified: one type with well defined cone tip and body with all cones having same orientation formed at low excimer fluence of 1 J/cm^2 and the other type having only a cone tip with different orientations formed at high fluences. Such conical
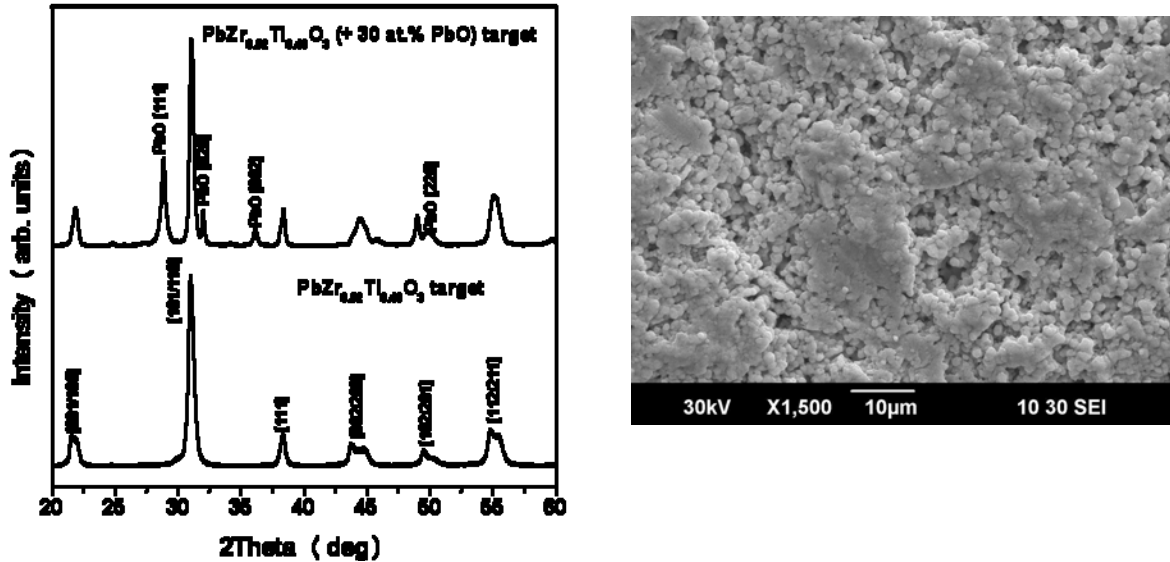

Fig. 31: (Left) XRD data for stoichiometric PZT target and PZT target with 30 at. % excess PbO (right) SEM image of typical PZT target before irradiation by excimer laser.

structures are indicative of preferential removal of highly volatile Pb during ablation. Also the higher ambient O_2 gas pressure favored the surface melt by confining the plasma expansion and facilitating the plasma absorption.
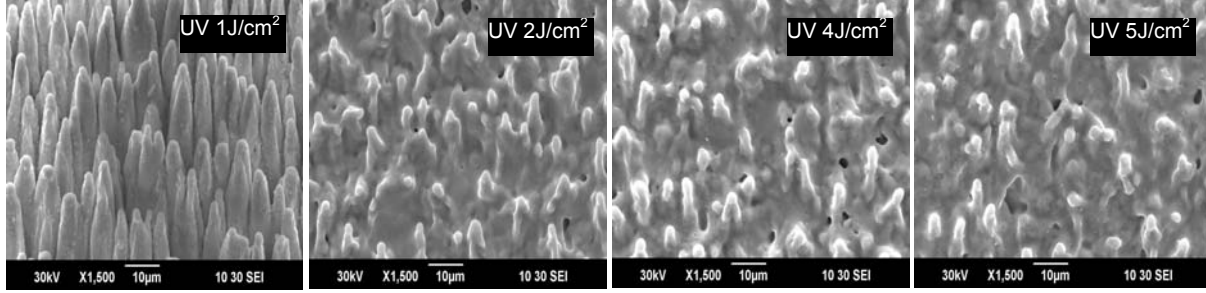

Fig. 32: SEM images of PZT (30 at. % excess PbO) target surface after irradiation by 1000 pulses of a KrF laser beam in 500 mT O_2 ambient at various UV laser fluences.

Figure 33 shows the chemical compositions measured using EDS of the laser target interaction sites for the stoichiometric PZT and the PZT (+30 at. % PbO) targets. For both the targets the lead content i.e. atomic % Pb/(Zr+Ti) increased with higher excimer fluences although the Zr and Ti content remained almost constant for the same range of fluences.
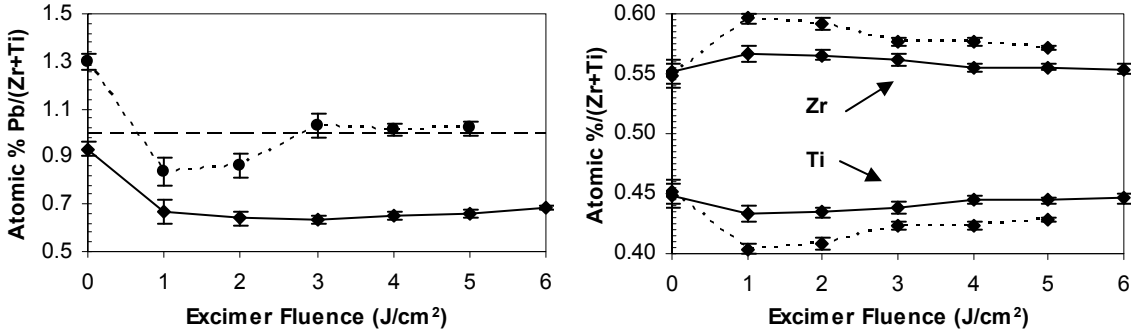

Fig. 33: Chemical compositions using EDS analysis of the ablated target surfaces versus excimer fluence for stoichiometric PZT (solid line) and PZT (30 at.% PbO) target (dotted line).

Initial studies using dual laser ablation showed that a temporal peak to peak interpulse delay of 100 ns was ideal for the efficient coupling of the CO_2 laser energy into the KrF laser ablated plasma plume [62]. Figure 34 shows SEM images of dual laser target interaction sites using a CO_2 laser fluence of 2J/cm^2 and varying the KrF laser fluence in the range 1-4 J/cm^2. Surface morphologies were similar as observed in single laser ablation.
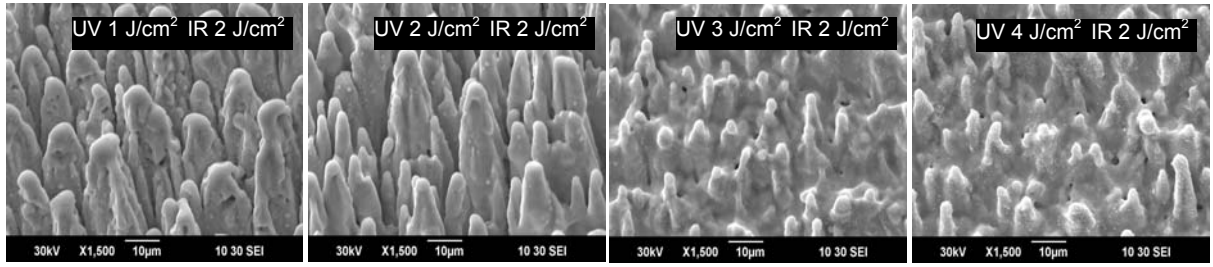
Fig. 34: SEM images of PZT (30 at.% excess PbO) target surface after irradiation by 1000 pulses of dual laser ablation using CO_2 laser fluence 2 J/cm^2 and varying excimer fluence from 1 to 4 J/cm^2 with 100 ns peak to peak interpulse delay in 500 mT O_2 ambient.

However, EDS analysis of the laser-target interaction sites showed that the amount of preferential Pb loss is lesser in dual laser ablation although the Zr and Ti contents were same in both cases as is evident in Figure 35. This happens because of the CO_2 laser energy gets absorbed into the initial excimer laser ablated plasma which causes increase in plasma temperature which increases the temperature of target surface facilitating the stoichiometric removal of materials by ablation [63].
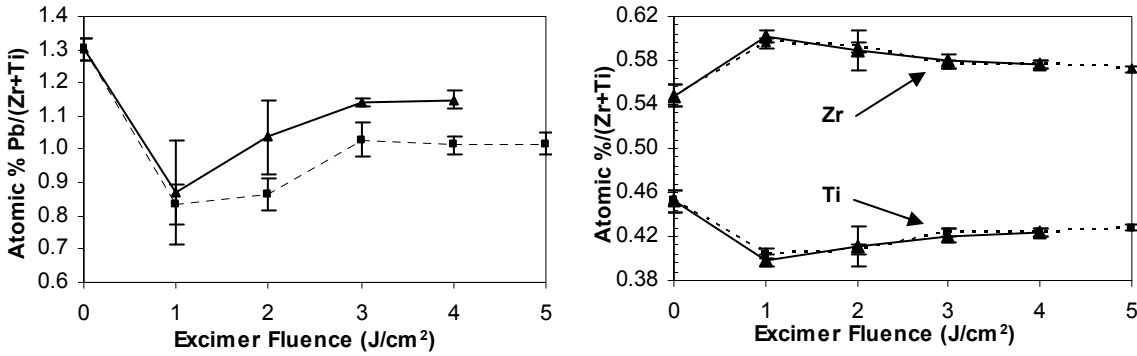

Fig. 35: Chemical compositions using EDS analysis of the ablated target surfaces versus excimer fluences for PZT (30 at.% PbO) target using single laser ablation (dotted line) and dual laser ablation (solid line) using CO_2 fluence of 2J/cm^2 and 100 ns peak to peak interpulse delay.

Plume dynamics by time-gated ICCD imaging:

ICCD images of the plasma plumes using the detector with zero gain showed that the visible plumes lasted for about 11 μs. Thus, in order to capture the complete visible emission a 20 μs gate was used.
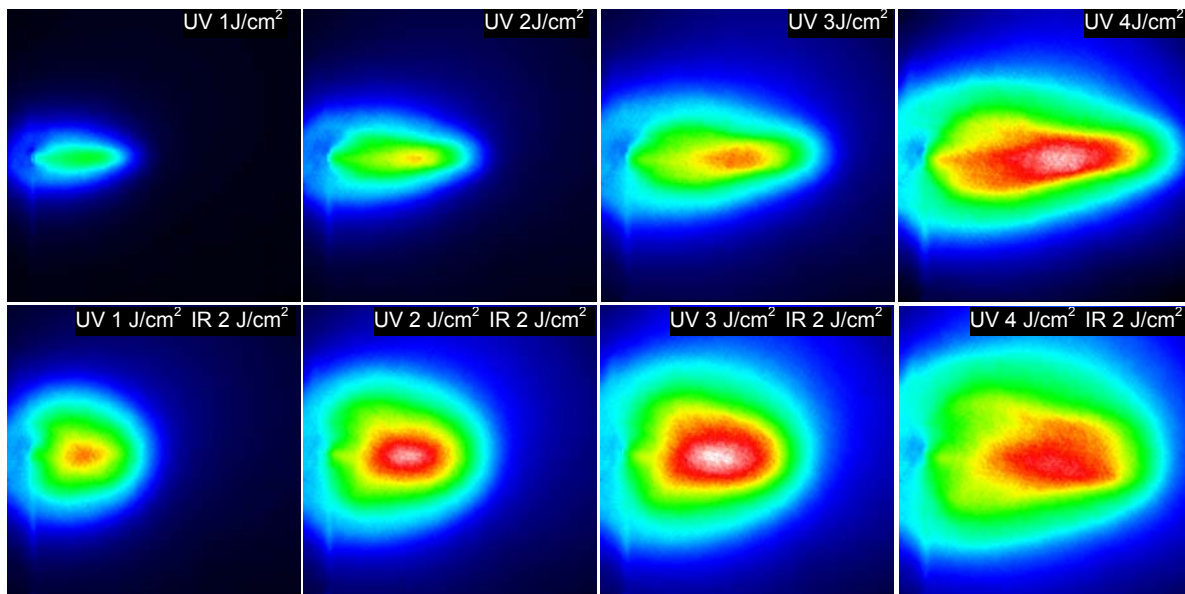
Fig. 36: ICCD images of total visible emission spectra of single laser plumes (top row) varying the excimer (UV) fluences from 1 to 4 J/cm^2 and dual laser plumes (bottom row) varying excimer fluences keeping 2 J/cm^2 CO_2 (IR) fluence and 100 ns peak to peak interpulse delay.

Figure 36 shows the ICCD images for the total visible emission spectra of the single and dual laser plumes at various fluences. The enhanced plume expansion in dual laser ablation showed the efficient coupling of CO_2 laser energy to the excimer laser ablated plume.

Thin film properties:

PZT films were grown epitaxially on single crystal $SrTiO_3$ (100) substrates at 550˚C with a background oxygen pressure of 500 mT. Initial studies indicated that the films grown from stoichiometric PZT target were Pb deficient which showed up as a pyrochlore impurity phase in XRD scans. A high O_2 pressure of 500 mT was used during growth to minimize the desorption of the high vapor pressure Pb from the film surface at 550 ˚C. Figure 37 shows the XRD scans of three films all deposited at 550˚C under 500 mT O_2 pressure, two using single laser ablation named as *S2J/cm^2* and *S5J/cm^2* i.e. using excimer fluences 2 J/cm^2 and 5 J/cm^2 respectively and one using dual laser ablation named *D1J/cm^{2}UV2J/cm^{2}IR* i.e. using KrF laser fluence 1J/cm^2 and CO_2 laser fluence 2J/cm^2 with 100 ns peak to peak interpulse delay. The films were highly textured with no observed peaks from secondary phase formation within the resolution limits of XRD. The log-scale for intensity was used to exaggerate the low intensity peaks so that if secondary phases are present, they can be identified easily. Figure 37 also shows the rocking scans about the PZT (200) plane for the single laser high fluence *S5J/cm^2* and dual laser *D1J/cm^{2}UV2J/cm^{2}IR* films both films having same thickness of about 350 nm. Both films have excellent in plane epitaxy indicated by the narrow full width half maxima of the rocking curves.
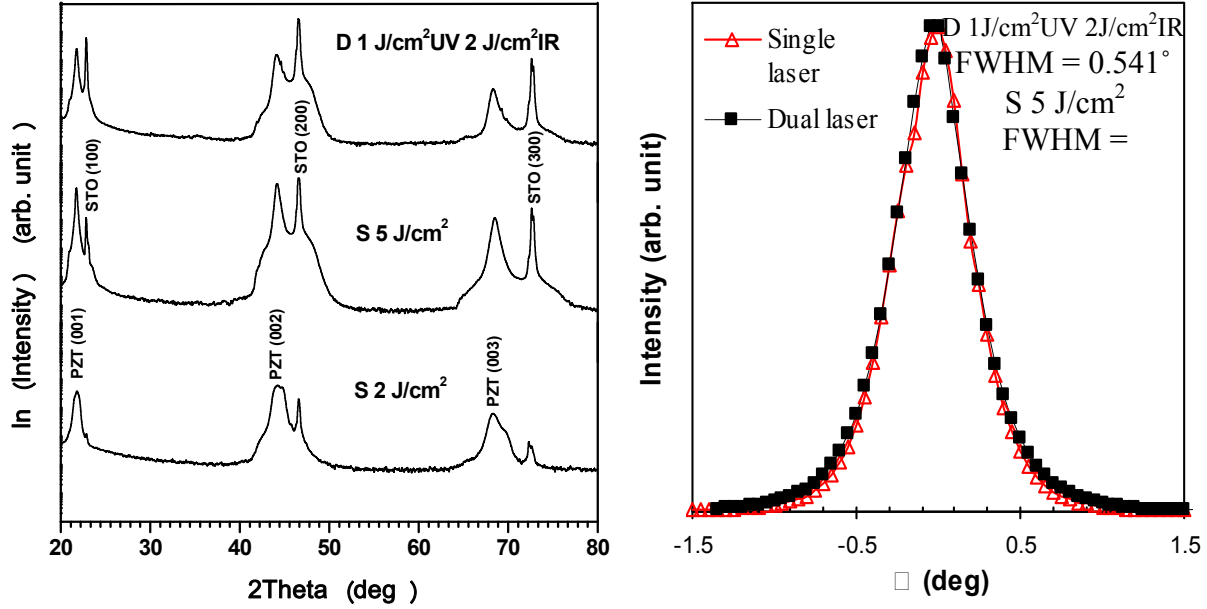
Fig. 37: (Left) XRD data for PZT films deposited on SrTiO$_3$ (STO) substrates using single laser ablation with excimer fluences of 2 J/cm^2 (S 2J/cm^2) and 5 J/cm^2 (S 5J/cm^2) and dual laser ablation with excimer fluence of 1 J/cm^2 and CO$_2$ fluence 2 J/cm^2 (D 1J/cm^{2}UV2J/cm^{2}IR). (Right) Rocking curves about PZT (200) plane for films S 5 J/cm^2 and D 1J/cm^{2}UV2J/cm^{2}IR.

EDS analysis of the films revealed that the atomic lead content Pb/(Zr+Ti) of single laser ablated film *S 2J/cm^2* was 0.39 and that for *S 5J/cm^2* was 0.85 respectively. However, the dual laser ablated film *D1J/cm^{2}UV2J/cm^{2}IR* had high Pb content of 0.84 showing the effectiveness of the method. Figure 38 shows the AFM surface images of the films under given conditions. A reduction in particulate density and surface roughness is observed in dual laser deposited film.
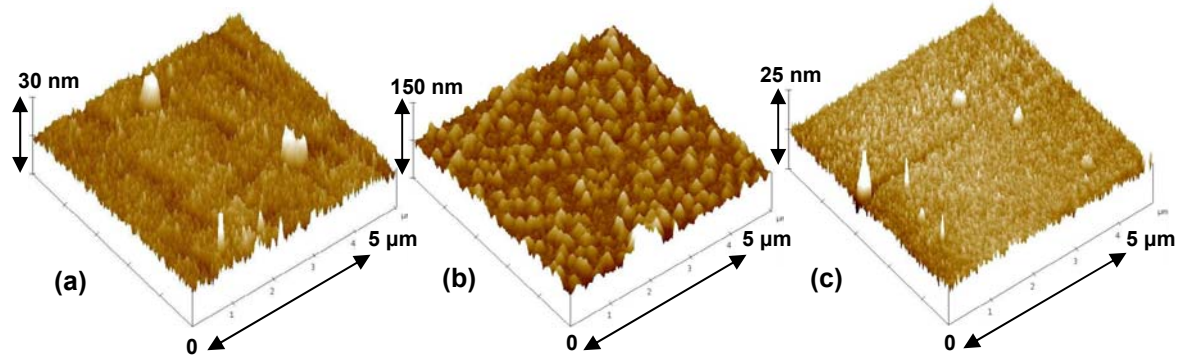
Fig. 38: AFM images of PZT films deposited using single laser ablation **(a)** *S 2J/cm^2* **(b)** *S 5J/cm^2* and **(c)** dual laser ablation *D1J/cm^{2}UV2J/cm^{2}IR*. All scan areas are 5x5 μm. Surface roughnesses for **(a)**, **(b)** and **(c)** are 3 nm, 12 nm and 2 nm respectively.

Properties of the dual-laser-deposited PZT films:

In this work, the dual-laser processed epitaxial PZT films were deposited on single crystal SrTiO$_3$ (STO) [001] substrates at 550˚C with a target-to-substrate distance of 4 cm. For

comparison, excimer single-laser (3 J/cm^2) ablated PZT films were deposited under the same conditions. In this report the nomenclature PZT$_{DL}$ and PZT$_{SL}$ refer to dual-laser and single-laser deposited films, respectively.

In order to test the polarization of the PZT capacitors, metallic oxide La$_{0.7}$Sr$_{0.3}$MnO$_3$ (LSMO) electrodes were used. LSMO/PZT/LSMO capacitors have been reported to have good fatigue endurance compared to other oxide electrodes [64]. The LSMO top and bottom electrodes were PLD deposited at 600 ˚C with the oxygen pressure fixed at 10 m Torr and using single-laser ablation (2 J/cm^2). The top LSMO electrodes were deposited in-situ using a shadow mask that produced 100 μm diameter contacts. The thicknesses of the individual LSMO and PZT layers were measured to be 100 and 500 nm, respectively.

Figures 39 (a) and (b) show the θ-2θ x-ray diffraction (XRD) scans (Cu Kα) for LSMO/PZT$_{DL}$ /LSMO/STO and LSMO/PZT$_{SL}$/LSMO/STO heterostructures, respectively. In both cases, only strong (00l) (l = 1,2, and 3) diffraction peaks of LSMO and PZT were observed
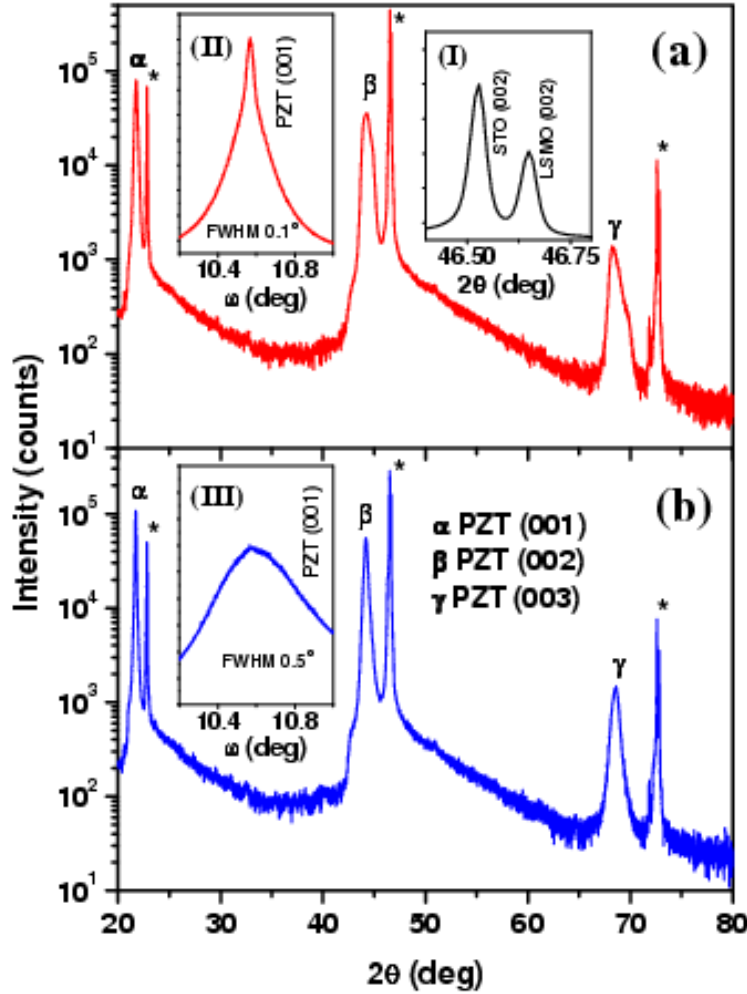
Fig. 39: X-ray diffraction θ-2θ scans of Pb(Zr$_{0.52}$Ti$_{0.48}$)O$_3$ (PZT)/La$_{0.7}$Sr$_{0.3}$MnO$_3$ (LSMO) heterostructures on (001) oriented SrTiO$_3$ (STO) substrates grown by (a) dual-laser ablation and (b) single-laser ablation. (a) Inset (I) shows the detail of STO (002) and LSMO (002) peaks around 2θ values of 46˚. (a) Inset (II) shows the (ω-scan) rocking curve of the PZT (001) peak with FWHM value of 0.1˚. (b) Inset (III) shows the rocking curve of the PZT(001) peak with the FWHM value of 0.5˚. The PZT (00l) (l = 1, 2, 3) reflections are denoted by α, β, γ and the LSMO/STO (00l) peaks are denoted by *.

along with those of the single-crystal STO substrate. This implied that the individual layers were grown epitaxially and formed highly textured films without any secondary impurity phases. Due to the very small lattice mismatch between LSMO (pseudo cubic perovskite, a = 3.876 Å) and STO (cubic perovskite, a = 3.905 Å) the (002) planes of LSMO and STO substrate are shown in detail in the inset (I) of Figure 22 (a). The PZT peaks were indexed with the tetragonal phase with space group P4mm (99). Inset (II) of Fig. 39 (a) and inset (III) of Figure 39 (b) show rocking curves (ω scans) about the PZT (001) plane for PZT_{DL} and PZT_{SL}, respectively. The smaller FWHM value for PZT_{DL} (0.1°) as compared to PZT_{SL} (0.5°) relates to better in plane orientation for the dual-laser deposited film.

Smoother surface, particulate-free film growths are unique trademarks of the dual-laser ablation process [65-67]. Figures 40 (a) and (b) shows atomic force microscope (AFM) images of the surfaces of PZT_{DL} and PZT_{SL} films, respectively. Clearly, PZT_{DL} (Figure 40 (a)) exhibits a smoother surface and smaller grain size with a root mean square (rms) roughness value of 1.6 nm compared to 11.5 nm for PZT_{SL} (Figure 40 (b)). We emphasize that the features for PZT_{DL} (z-height 75 nm) are two times smaller than those on PZT_{SL} (z-height 150 nm). Figure 41 shows the room temperature polarization versus electric field (P-E) hysteresis loops for PZT_{DL} and PZT_{SL} at an applied voltage of 9 V. The polarization values (P_{max}) at maximum applied voltage (9 V) for PZT_{DL} and PZT_{SL} were 100 $\mu C/cm^2$ and 75 $\mu C/cm^2$, respectively. The remnant polarization (P_r) values for PZT_{DL} and PZT_{SL} were 73 $\mu C/cm^2$ and 27 $\mu C/cm^2$ respectively.
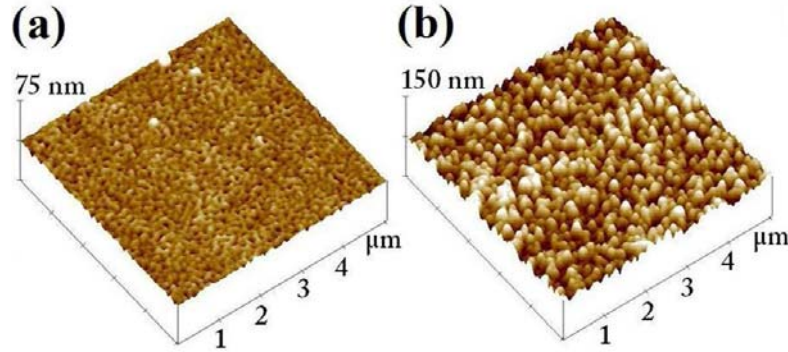
Fig. 40: AFM images of the $Pb(Zr_{0.52}Ti_{0.48})O_3$ (PZT) layer for the $PZT/La_{0.7}Sr_{0.3}MnO_3$ heterostructures on $SrTiO_3$ (STO) substrates deposited using (a) dual-laser ablation and (b) single-laser ablation. The scan areas are 5 x 5 μm. The scan height for (a) is half (75 nm) that of (b) (150 nm). The rms surface roughness values for (a) and (b) are 1.6 nm and 11.5 nm, respectively.

The P_r values for PZT_{SL} matched well with those reported by different groups for LSMO/PZT/LSMO heterostructures grown by PLD [63, 68]. Further, the PZT_{DL} capacitor had a lower leakage current of 0.2 x 10^{-9} A as compared to PZT_{SL} that had a value 0.4 x 10^{-9} A for an applied voltage of 9V for 1 second soak time. The nominal switching voltages, given by $V_c = E_c d$, where d is the film thickness and E_c is the coercive field, for PZT_{DL} and PZT_{SL} were 2.72 and 2.30 V, respectively. The E_c values, calculated using d as 500 nm for PZT_{DL} and PZT_{SL} were 54.5 and 46 kV/cm, respectively. The P-E loop for PZT_{SL} in Fig. 41 shows a slight shift towards positive voltages as a consequence of high built-in field [68]. However, the P-E curve for PZT_{DL} did not show any asymmetric behavior which could result in imprint failures.

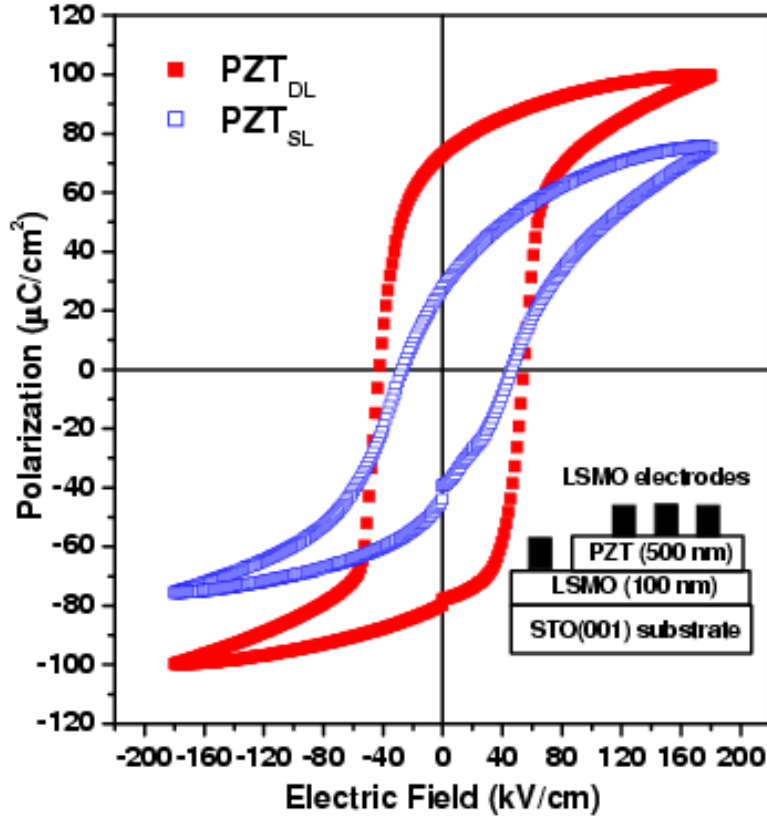Fig. 41: P-E hysteresis loops measured from Pb(Zr$_{0.52}$Ti$_{0.48}$)O$_3$ capacitors, PZT$_{DL}$ and PZT$_{SL}$, using La$_{0.7}$Sr$_{0.3}$MnO$_3$ (LSMO) top and bottom electrodes on SrTiO$_3$ (STO) substrates. PZT$_{DL}$ and PZT$_{SL}$ refer to PZT films grown by dual-laser and KrF single-laser ablation processes, respectively. The data was taken at a driving voltage of 9 V. The inset shows a schematic illustration of the LSMO/PZT/LSMO capacitors with the thicknesses of LSMO and PZT layers being 100 nm and 500 nm, respectively.

Figures 42 (a) and (b) show the fatigue (degradation) properties of PZT$_{DL}$ and PZT$_{SL}$ respectively using standard positive up negative down (PUND) testing mode to simulate ferroelectric memory operation. PUND characterization was performed using a pulse waveform of 0.01 ms pulse width and peak voltages +9 V and –9 V at 10 kHz. Figure 25 shows the (positive/negative) switching polarization (P$_{sw}$/-P$_{sw}$) and linear non-switching polarization (P$_{ns}$/-P$_{ns}$) values when a (positive/negative) read voltage (9 V/-9V) was applied to the capacitors. For device application the value of (P$_{sw}$ – P$_{ns}$) should be large enough for signal detection. Although the value of (P$_{sw}$ – P$_{ns}$) for PZT$_{SL}$ remained nearly constant between 10^4 to 10^9 cycles as has been reported earlier, [69] the P_{max} values at 9 V calculated from P_{max} (9V) = (P$_{sw}$– P$_{ns}$)/2 showed a small variation starting with a low value of ≈ 53 μC/cm^2 at 10^4 cycles, reaching a maximum of ≈ 88 μC/cm^2 at 10^6 cycles and finally ≈ 68 μC/cm^2 at 10^9 cycles, which can be easily inferred from Figure 25 (b). The P_{max} values for PZT$_{SL}$ have not been shown for clarity. This small variation was due to the higher value of P$_{ns}$ for PZT$_{SL}$ associated with higher leakage current at 9 V. On the other hand, P$_{sw}$ and P$_{ns}$ values for PZT$_{DL}$ remained constant throughout as shown in Figure 25 (a). Further, P$_{max}$ values at 9 V for PZT$_{DL}$ remained constant at ≈ 100 μC/cm^2 as was expected. From Fig. 25 it is clear that PZT$_{DL}$ exhibited a better fatigue response compared to PZT$_{SL}$. Possible explanation could be associated with a reduced number of defects within the film since defect associated electrode-film interface are similar in both the cases.
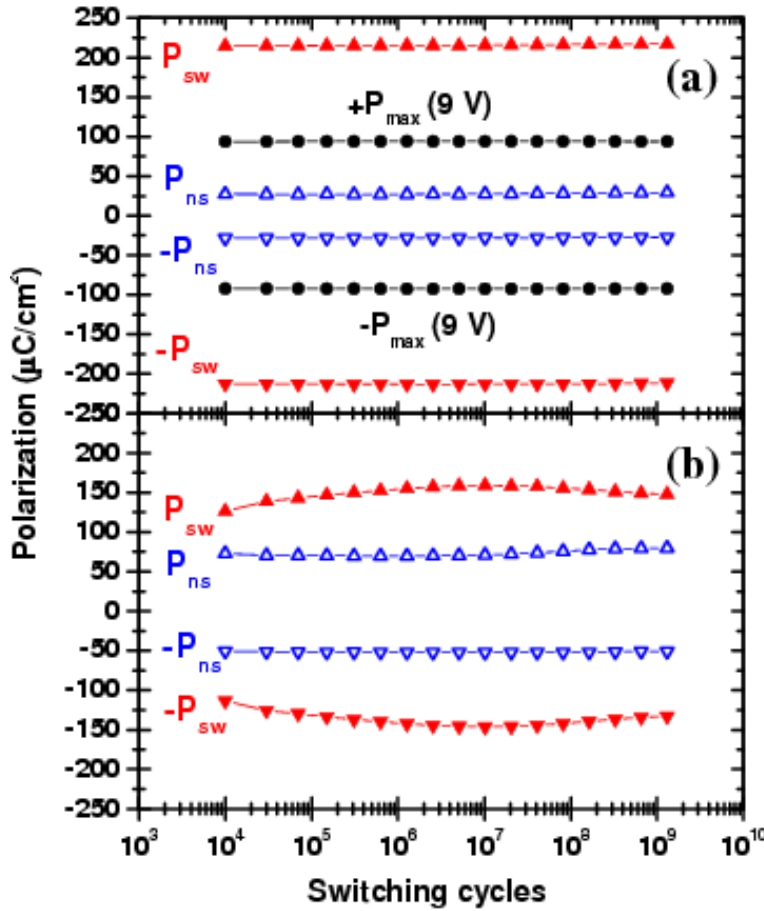
Fig. 42: Results of positive up negative down (PUND) fatigue tests at 10 kHz for $La_{0.7}Sr_{0.3}MnO_3$(LSMO) /$Pb(Zr_{0.52}Ti_{0.48})O_3$(PZT)/ LSMO capacitors grown by (a) dual-laser ablation and (b) KrF single-laser ablation. Both (a) and (b) show the variations of P_{sw}, P_{ns}, - P_{sw} and $-P_{ns}$ versus number of switching cycles. Here $-P_{sw}$ and - P_{ns} denote switching polarization and linear non-switching polarization, respectively, when a negative read voltage of – 9 V is applied to the capacitor. P_{max} (9V) = $(P_{sw} - P_{ns})/2$

In summary, using the dual-laser ablation process we have successfully grown stoichiometric, particulate-free, and smooth PZT films with the desired perovskite structure and no impurity phases as compared to single-laser PLD. The films have enhanced ferroelectric properties with high P_r and low coercive fields E_c making them feasible for device application. This technique could be generalized to all multi-component thin film growth with a high volatility element which would lead to non-stoichiometric transfer of materials in other processes.

(b) Role of epitaxy in controlling the magnetic and magnetostrictive properties of cobalt ferrite-PZT bilayers:

Introduction:

Magnetostriction is a well known property of magnetic materials associated with the change in dimensions upon magnetization [70,71]. As a result, elastic strains are developed in the crystal lattice that change the alignment of the magnetic moments and create the magnetoelastic effect in the material [72, 73]. Cobalt ferrite, $CoFe_2O_4$ (CFO), belongs to the family of spinel-type ferrites and is one of the important magnetic materials with high coercivity, moderate magnetization and highest magnetostriction coefficient (λ_{100} = -200 x 10^{-6} to -590 x 10^{-6}) [70, 74]. CFO has been

extensively explored as a promising magnetostrictive material for applications in actuators, sensors, and transducers [75-78]. It is also considered as a key component for multiferroic multilayers or composites [79]. When coupled with ferroelectric materials like $BaTiO_3$ (BTO) or $Pb(Zr,Ti)O_3$ (PZT), CFO exhibits the magnetoelectric (ME) effect [80,81]. So far, there are numerous reports on ME effect in layered CFO-PZT structures mostly grown on $Pt/Ti/SiO_2/Si$ substrates [72-87] and only a few on MgO or STO substrates [88, 89]. The residual strain at the CFO-PZT interface is the dominating factor that dictates the ferromagnetic properties in epitaxial CFO-PZT thin films [90, 91]. This suggests that 'strain engineering' is an important aspect in these ferroelectric/ferromagnetic structures. However, structural parameters that quantify this behavior have remained elusive. Hence a systematic study on the role of epitaxy in controlling the magnetic properties of CFO-PZT bilayers films would be beneficial.

In the present work, epitaxial thin films of CFO single layer and CFO-PZT bilayers were grown on single crystal MgO and $SrTiO_3$ (STO) substrates by pulsed laser deposition. The magnetic properties of the as-grown thin films were measured at 10 K and 300 K by applying magnetic fields both parallel and perpendicular to the film planes. The CFO-PZT bilayer films showed enhanced or reduced values of magnetization as compared to that of the CFO single layer films depending on the substrate of deposition. A strain compression-relaxation mechanism has been proposed in order to explain the structure-property relationships in the CFO-PZT bilayer thin films.

Experimental:

Pulsed laser deposition (PLD) technique was adopted to grow the epitaxial CFO single layer and bilayer thin films on 1cm x 0.5 cm^2 single crystalline MgO (100) and SrTiO3 (STO) (100) substrates. Henceforth, the nomenclature CFO/MgO and CFO/STO for CFO single layer thin films on MgO and STO substrates, respectively, will be used in the text. Similarly, the CFO-PZT bilayer thin films grown on MgO and STO substrates will be referred as PZT/CFO/MgO and PZT/CFO/STO, respectively. The deposition chamber was attached to a custom-built multi-target holder that allowed for the in-situ deposition of multilayers with clean interfaces. A distance of 6 cm was maintained between the substrates and the targets during deposition. Compressed powder targets of CFO and $Pb(Zr_{0.52}Ti_{0.48})O_3$ were ablated using a KrF excimer laser (λ = 248 nm) operating at 10 Hz. All the films were deposited with an energy density of 2 J/cm^2 at the target surface. For the PZT/CFO/MgO and PZT/CFO/STO thin films, the CFO layer was deposited at 450°C, 10 mTorr O_2 pressure and at an average deposition rate of 0.1 Å/pulse. A 200 nm layer thickness was achieved through these parameters. The subsequent PZT layer of same thickness was deposited at 550 °C, 300 mTorr O_2 pressure. CFO/MgO and CFO/STO films of similar thicknesses were prepared under the same experimental conditions for comparison. The crystallinity and the in-plane epitaxy of the deposited thin films were confirmed by θ-2θ scans, rocking curve analysis and φ (azimuthal) scans using X-ray diffraction (XRD) (Bruker D 8 Focus and Philips X'pert Diffractometer). Peak shifts due to sample misalignment was taken care of while performing the XRD scans. The surface morphologies were studied using Atomic Force Microscope (AFM, Digital Instruments). The magnetization measurements of the thin films were performed using a commercial Physical Property Measurement System (PPMS) from Quantum design.

Results and discussion:

Crystallinity and surface morphology:

The small lattice mismatch (0.04 %) between PZT (tetragonal perovskite, lattice parameters, a=b= 4.036 Å, c= 4.146 Å) and CFO (face-centered cubic, lattice parameter, a = 8.391 Å) as well as between CFO and the substrates allowed for the growth of the epitaxial films. Figures 43 (a) and 43 (b) show the XRD θ-2θ spectra for PZT/CFO/MgO and CFO/MgO, respectively. XRD spectra for PZT/CFO/STO and CFO/STO are shown in Figures 43(c) and 43(d), respectively. In all the samples the single phase nature and epitaxial relationship with the substrates were observed. The XRD peak in CFO was assigned to the (400) plane, corresponding to the face-centered cubic (fcc) phase of CFO with space group Fd-3m (227). For PZT/CFO/MgO and PZT/CFO/STO films, the PZT peak was indexed to the (100) plane of tetragonal PZT with space group P4mm (99) (Figure 43(a) and (c)). Due to the small lattice mismatch between MgO (face-centered-cubic, 2 x lattice parameter = 8.42 Å) and CFO, the MgO (200) and CFO (400) peaks were in close occurrence to each other in the θ-2θ spectra. Insets to the Figures 43(a) and (b) visibly show the MgO and CFO peaks in the samples. However, due to the larger lattice mismatch between STO (primitive cubic, 2 x lattice parameter = 7.81 Å) and CFO, the (400) peaks of CFO were shifted significantly (Figures 43(c) and (d)) as compared to the peaks of polycrystalline CFO [92, 93]. The out-of-plane lattice parameter ($a_\perp$) for CFO was calculated from the XRD θ-2θ scans (see Table 1).

In order to verify the in-plane epitaxial relationship and cubic symmetry for the CFO and PZT layers, φ scans were performed. Figures 44(a) and (b) show the φ scan spectra from the PZT (101) plane for PZT/CFO/STO and PZT/CFO/MgO, respectively. Figures 44(c) and (d) show the φ scan spectra from the CFO (311) plane for PZT/CFO/STO and PZT/CFO/MgO, respectively. Figures 44(e) and (f) show the φ scan spectra from the CFO (311) plane for CFO/STO and CFO/MgO, respectively. In all cases, the peaks in the φ spectra occurred at intervals of 90° suggesting four-fold cubic symmetry and cube-on-cube growth. Figures 44(g) and (h) show the rocking curves (ω scans) about the CFO (400) planes for PZT/CFO/STO and CFO/STO, and PZT/CFO/MgO and CFO/MgO, respectively. The small full-width at half maximum (FWHM) values (< 1°) of the rocking curves confirmed a good degree of in-plane orientation for CFO in all the samples (see Table 1 for FWHM values). However the (400) texture was sharper in the films grown on MgO which may be attributed to the smaller lattice mismatch between CFO and MgO. In addition, the degree of (400) texturing of CFO weakened slightly in PZT/CFO/STO and PZT/CFO/MgO compared to PZT/STO and PZT/MgO, respectively. Figures 44(i) and (j) show the asymmetric scans of (511) and (440) planes of CFO for CFO/STO and CFO/MgO, respectively. Figures 44(k) and (l) show the similar asymmetric scans for PZT/CFO/STO and PZT/CFO/MgO, respectively. For Figures 44(i) to (l) the left peaks are from CFO (511) plane and the right peaks are from CFO (440) planes. The average in-plane lattice parameters (a_η) for CFO in the samples were calculated from the asymmetric scans shown in Figures 44 (i) to (l) (see Table 1).
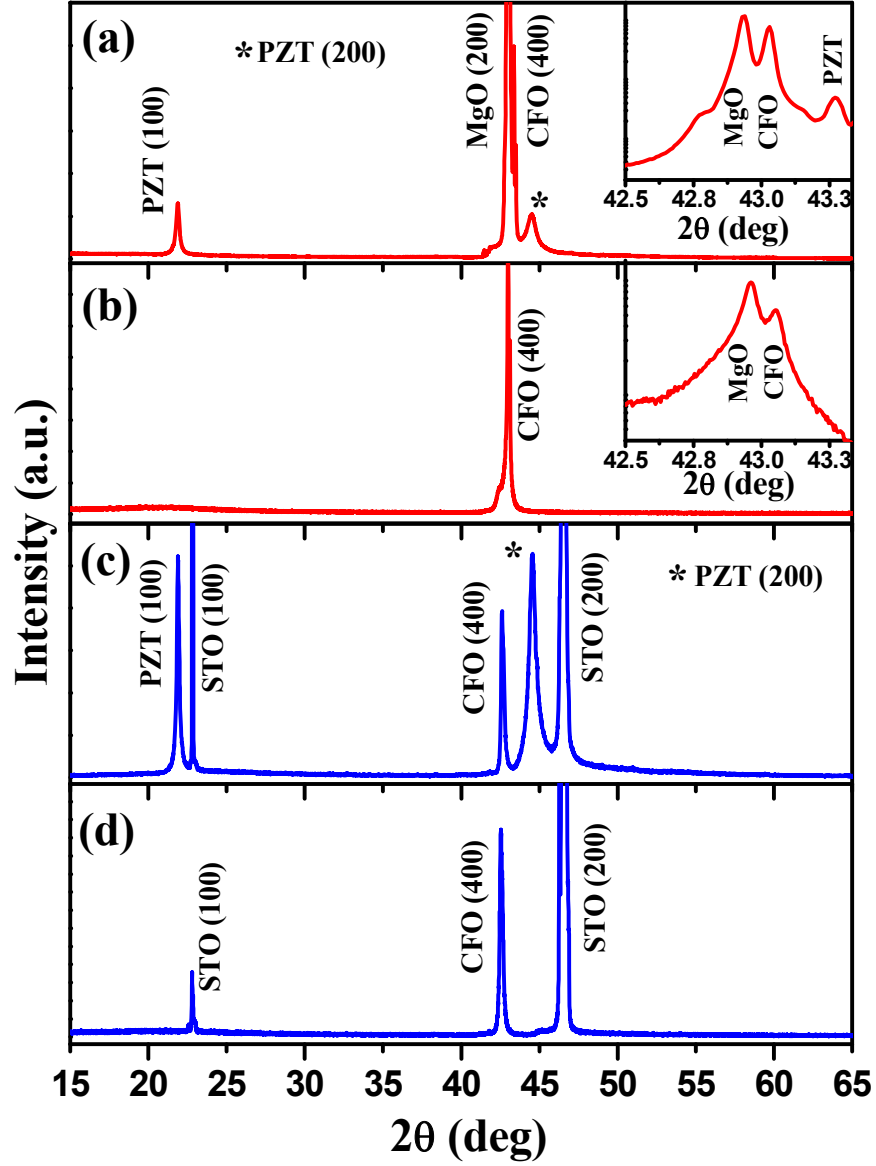
Fig. 43: XRD θ-2θ scans for single layer CFO and bilayer CFO-PZT films grown on MgO (a and b) and STO substrates (c and d), respectively. The insets to (a) and (b) show the details of the MgO (200), CFO (400) and PZT (200) peaks around 43˚.

The strain (ε) in the CFO layer was calculated by using the formula $\varepsilon = (a-a_o)/a_o$, where a is out-of-plane ($a_\perp$) or in-plane (a_η) lattice parameter and a_o is the bulk unstressed lattice parameter of CFO (a_o = 8.39 Å) [93]. The in-plane stress (σ_η) in the film was calculated using the relation $\sigma_\eta = Y \, \varepsilon_\eta$ where ε_η is the in-plane strain (ε) and the Young's modulus value for CFO(Y = 1.5 x 10^{12} dyne/cm^2) [92]. Table 1 summarizes the lattice parameters and strains calculated for the out-of-plane and in-plane configurations.
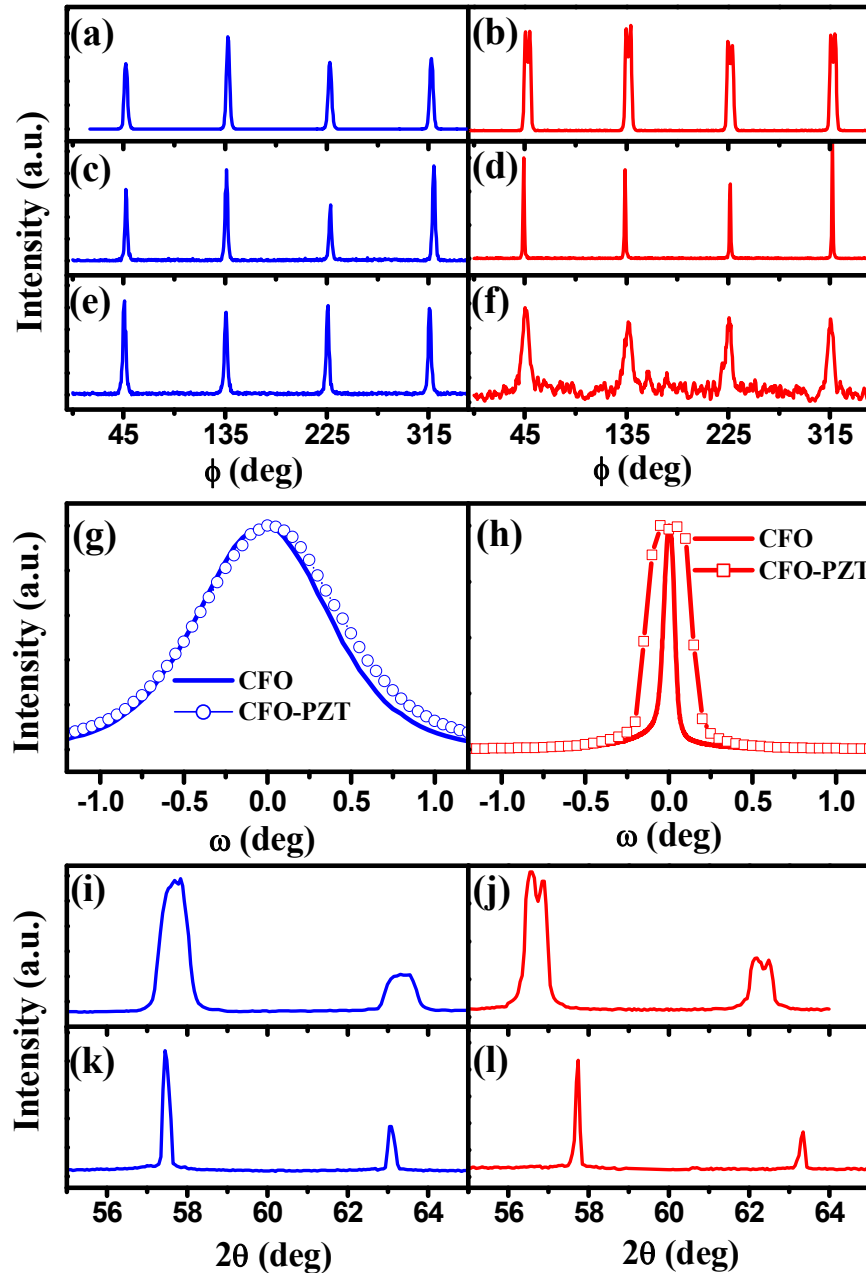
Fig. 44: Left and right columns represent the films grown on STO and MgO substrates respectively. (a and b) are φ scan spectra from PZT (101) reflection in CFO-PZT bilayer film. (c and d) and (e and f) are φ scan spectra from (311) CFO reflection in CFO-PZT bilayer and single layer CFO films respectively. (g and h) are rocking curves of CFO (400) peaks. (i and j) and (k and l) are asymmetric scans of (511) and (440) CFO planes for single layer CFO films and bilayer layer CFO-PZT films respectively. (i − l) Left peaks are from CFO (511) plane and the right peaks are from CFO (440) planes.

From the strain values listed in Table 1 it is seen that the CFO/MgO films grew with slight in-plane tensile ($\varepsilon_\eta = 0.0015$) and out-of plane compressive ($\varepsilon_\perp = $ -0.0005) strains. On the other hand, the CFO/STO film grew with larger in-plane compressive ($\varepsilon_\eta = $ -0.0116) and out-of plane tensile ($\varepsilon_\perp = 0.0124$) strains. This could be attributed to the different lattice mismatches of CFO with MgO and STO substrates. The lattice mismatch at room temperature was calculated using the relation $(a_s - a_o)/a_s$ (%) where a_s is the lattice parameter of the substrate. The calculated values for CFO/MgO and CFO/STO were 0.36% and 7.8%, respectively. It was also observed that the in-plane lattice parameter (a_η) of CFO for the PZT/CFO/MgO film ($a_\eta = 8.294$ Å) was smaller than that of the CFO/MgO film ($a_\eta = 8.403$ Å). This suggested that possibly with the deposition of the PZT layer on top, the CFO layer experienced an in-plane compression that compelled it to match its a_η to the smaller lattice parameter of PZT ($a = b = 4.036$ Å, $c = 4.146$ Å). As a consequence the in-plane strain and consequently the stress was amplified in PZT/CFO/MgO. However, an opposite trend was observed for the films grown on STO substrates. The CFO/STO film was already highly strained due to the large mismatch between the STO substrate and CFO. With PZT layer on top of it, the PZT/CFO/STO film was slightly relaxed to a lower strain state.

Table 1. FWHM of rocking curves about CFO (400) plane, in-plane (a_η) and out-of-plane ($a_\perp$) lattice parameters obtained from XRD peaks, in-plane (ε_η) and out-of-plane ($\varepsilon_\perp$) strains calculated using $\varepsilon = (a-a_o)/a_o$, where a is a_η or $a_\perp$ and a_o is the bulk lattice parameter of CFO ($a_o = 8.39$ Å), and the in-plane stress calculated from in-plane strain and Young's modulus of CFO ($Y = 1.5 \times 10^{12}$ dyne/cm^2) for CFO and CFO-PZT films on MgO and STO substrates.

Sample	FWHM of Rocking curve (°)	$a_\perp$ (Å)	Out-of-plane strain $\varepsilon_\perp$	$a_\parallel$ (Å)	In-plane strain $\varepsilon_\parallel$	In-plane stress (dyne/cm^2)
CFO/MgO	0.076	8.386	-0.0005	8.403	0.0015	2.25×10^9
PZT/CFO/MgO	0.321	8.338	-0.0062	8.294	-0.0114	-17.1×10^9
CFO/STO	0.915	8.494	0.0124	8.292	-0.0116	-17.5×10^9
PZT/CFO/STO	0.986	8.479	0.0106	8.33	-0.0071	-10.7×10^9

In order to analyze the surface morphologies of the thin films and predict their mechanisms of growth, AFM was employed. Figure 45(a) illustrates an AFM image of the CFO
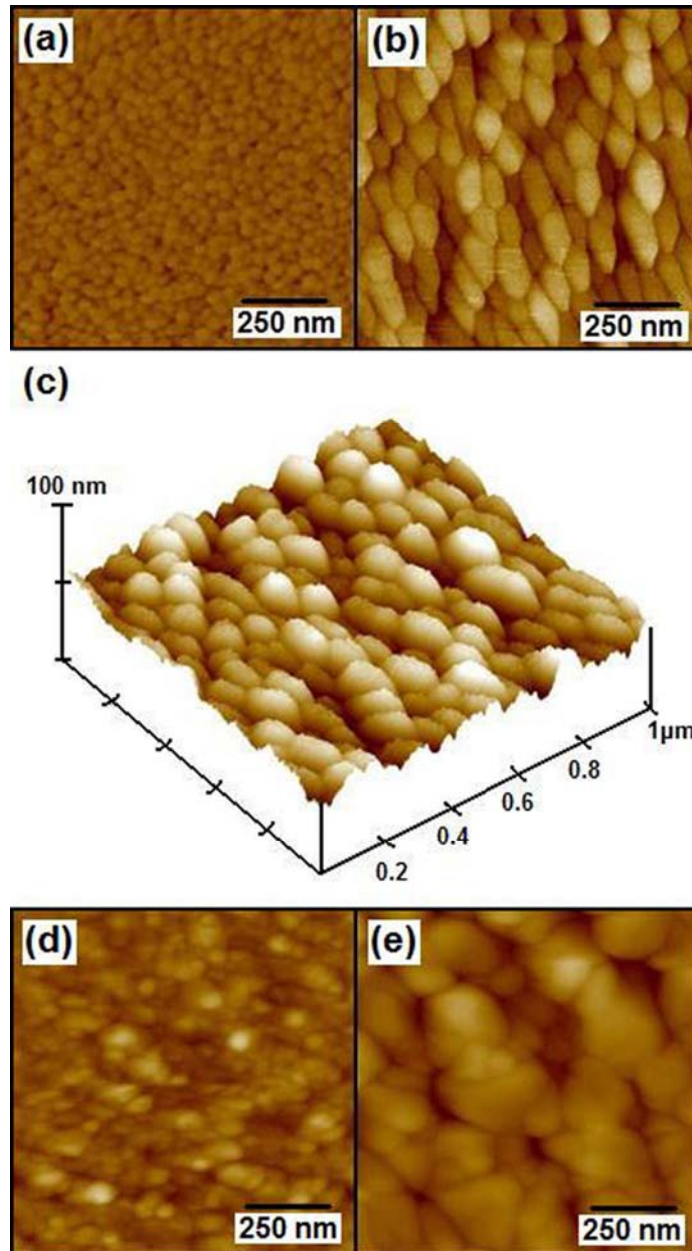
top layer for CFO/MgO film. The image revealed a very smooth and compact surface with a root mean square roughness (R_{rms}) value of 2.084 nm and small grain size with relatively uniform size distribution. As reported earlier such a flattened surface could be indicative of a layer-by-layer growth mechanism [93]. Figure 45(b) shows an AFM image of the PZT top layer for PZT/CFO/MgO film.

The PZT layer was relatively less smooth with R_{rms} value of 11.456 nm and larger grain size as compared to CFO/MgO. Uniform grain size distribution was also observed for PZT. The surface exhibited a texturing which could be reminiscent of epitaxial growth. Additionally, the grains appeared to be preferentially elongated in one in-plane orientation. This effect could be correlated to the larger difference in the a_η (8.294 Å) and $a_\perp$ (8.338 Å) values of the CFO layer in PZT/CFO/MgO (Table 1). From Figure 45(c), which is a 3 dimensional projection of the PZT top layer shown in Figure 45(b), distinct cusp (or valleys) and dome features were observed to be exposed on the film surface. It has been reported earlier that such cusps are associated with high stress concentration regions [94, 95] which increase of the surface energy and gets compensated by the decrease of strain energy via elastic strain relaxation in the films. This strain relaxation of the top PZT layer suggested that probably the bottom CFO layer was more strained. Films grown on STO substrates showed distinctively different surface morphology. Figure 45 (d) shows the surface of CFO/STO film. The surface appears rougher than CFO/MgO with R_{rms} value of 7.502 nm. It also consisted of grains with various shapes and sizes. This could be attributed to the island growth mode [93, 95]. Figure 45 (e) shows the PZT top surface for PZT/CFO/STO film. The various grain sizes with larger grain growth and R_{rms} value of 22.683 nm still conformed to the island growth mechanism.

Magnetization measurements:

Figure 46 shows the magnetization (M) - magnetic field (H) hysteresis loops for PZT/CFO/MgO and CFO/MgO, respectively. Similarly, Figure 47 shows the M-H loops for PZT/CFO/STO and CFO/STO, respectively. The in-plane and out-of-plane configurations
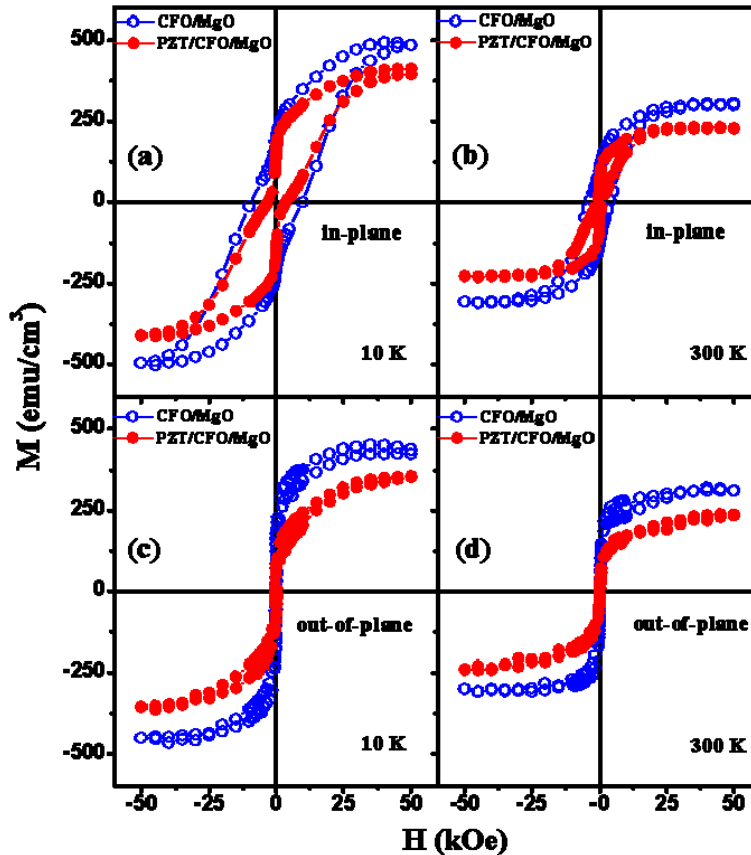

Fig. 46: M-H loops measured at (a and c) 10 K and (b and d) 300 K for the CFO-MgO and PZT-CFO-MgO films, respectively. The in plane and out of plane denote directions for the magnetic field applied parallel or perpendicular to the film plane, respectively.

symbolized by וו and ⊥, respectively, represent the application of the magnetic fields parallel and perpendicular to the film planes. The hysteresis loops were acquired after the removal of the diamagnetic contribution from the substrates. In addition since the thickness of CFO layer was kept constant in all the films, the magnetization values were only normalized to the volume of the CFO layer assuming no magnetic contribution from the PZT layer. Table 2 summarizes the saturation magnetization (M_s), ratio of remnant magnetization (M_r) to M_s and the coercivity (H_c) for all the samples at 300 K and 10 K. The M_r/M_s ratio provides an estimate of the degree of squareness of the loops.

The magnetic measurements were performed both at 300 K and 10 K to emphasize the consistency of the underlying mechanisms. The M_s values for CFO films on STO substrates were larger than those on MgO substrates [95]. The M_s value for the PZT/CFO/STO film was about 5.8 μ_B per Co^{2+} site which is much higher than the theoretical bulk value of 4 μ_B per Co^{2+} site [95].

Table 2. Summary of saturation magnetization (M_s), ratio of remnant magnetization (M_r) to M_s and the coercivity (H_c) for CFO and CFO-PZT films on MgO and STO substrates measured at 300 K and 10 K. The in-plane and out-of-plane directions have been denoted by the symbols וו and ⊥, respectively.

	300 K							
Sample	$M_s\|$ (emu/cm^3)	$M_s\|$ (μ_B/Co^{2+})	$M_r/M_s\|$ (%)	$H_c\|$ (kOe)	$M_s\perp$ (emu/cm^3)	$M_s\perp$ (μ_B/Co^{2+})	$M_r/M_s\perp$ (%)	$H_c\perp$ (kOe)
CFO/MgO	305 ± 4	2.4	37.6	3.8	310 ± 6	2.5	<13.9	< 0.03
PZT/CFO/MgO	228 ± 2	1.8	25.8	1	234 ± 5	1.8	<5.9	<0.03
CFO/STO	478 ± 5	3.8	53.9	3.5	> 164	> 1.3	>21.6	3.0
PZT/CFO/STO	592 ± 5	4.7	53.6	3.4	190	1.5	41.5	0.1

	10 K							
Sample	$M_s\|$ (emu/cm^3)	$M_s\|$ (μ_B/Co^{2+})	$M_r/M_s\|$ (%)	$H_c\|$ (kOe)	$M_s\perp$ (emu/cm^3)	$M_s\perp$ (μ_B/Co^{2+})	$M_r/M_s\perp$ (%)	$H_c\perp$ (kOe)
CFO/MgO	>497	>3.9	>41.3	10	441 ± 12	3.5	30.9	0.3
PZT/CFO/MgO	>400	>3.2	>39.6	4	353 ± 3	2.8	18.1	0.3
CFO/STO	541 ± 9	4.3	63.1	11	> 164	> 1.3	>14.6	0.7
PZT/CFO/STO	728 ± 9	5.8	65.6	11	206	1.6	28.8	0.5

From Figure 46 it could be observed that the magnetization of CFO reduced in PZT/CFO/MgO film as compared to that in CFO/MgO film both at 300 K and 10 K. Around 25% decrease in the M_s values was observed for CFO/MgO film with the deposition of the PZT top layer top both in the in-plane and out-of-plane directions at 300 K (see Table 2). However the H_c values still remained about the same. The out-of-plane anisotropy exhibited by the CFO/MgO film could be clearly seen in the M-H loops measured at 10 K (Figures 46(a) and (c)). The in-

plane magnetization did not show any saturation even at 50 kOe while on the other hand the out-plane magnetization showed well behaved saturation. This behavior was preserved in the M-H loops of PZT/CFO/MgO films. This suggested that the easy axis of magnetization of CFO/MgO film did not change with deposition of the PZT top layer. In short, the net effect of addition of the PZT layer on top of CFO/MgO film was an observed decrease in magnetization with nominal change in coercivity and squareness.

In contrast, magnetization of CFO/STO film increased with the addition of PZT on top as shown in Figure 47. Around 25% and 34% increase in the in-plane M_s could be estimated for PZT/CFO/STO at 300 K and 10 K, respectively (see Table 2). The out-of-plane M_s also increased by 25% at 10 K in the PZT/CFO/STO film as compared to CFO/STO film. The CFO/STO film exhibited strong in-plane anisotropy with well saturated loops in the in-plane direction (Figures 47(a) and (b)) and almost no saturation in the out-of-plane direction (Figures 47(c) and (d)). However, from Figure 47 (d) it is evident that the out-of-plane magnetization at
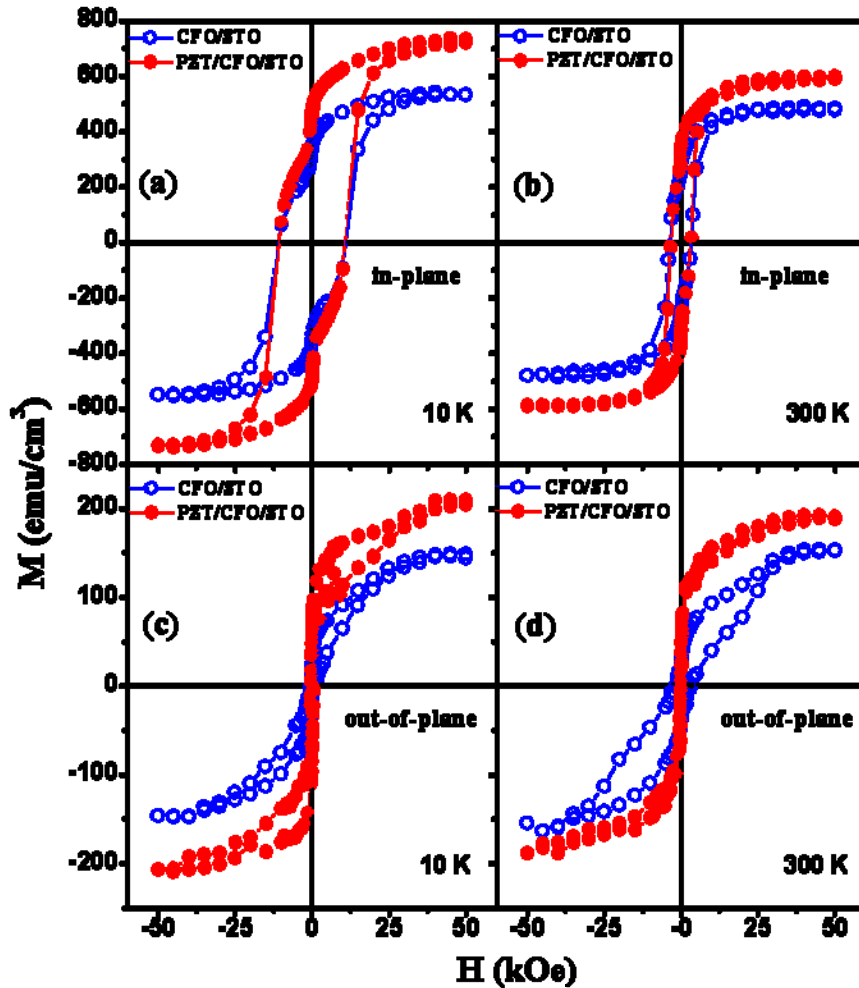

Fig. 47: M-H loops measured at (a and c) 10 K and (b and d) 300 K for the CFO-STO and PZT-CFO-STO films, respectively. The in plane and out of plane denote directions for the magnetic field applied parallel or perpendicular to the film plane, respectively.

300 K for PZT/CFO/STO showed well saturated behaviour with an almost double M_r/M_s ratio (see Table 2) compared to CFO SL film on STO. A similar trend was observed at 10 K (Figure 47 (c)). This could possibly indicate a reorientation in the direction of the easy axis of magnetization for CFO/STO film with the deposition of the PZT top layer. Thus the net effect on the magnetic properties of CFO/STO film with PZT top layer is an increase in magnetization and change in direction of magnetic anisotropy.

The effect of stress (σ) on the magnetization of a magnetostrictive material can be understood from the following thermodynamic relation [96,97]:

$$\frac{1}{l}\frac{\partial l}{\partial H} = \frac{1}{4\pi}\frac{\partial B}{\partial \sigma}$$

where B is the magnetic induction , σ is the stress, l is the length of the material and H is the external applied magnetic field. From equation (1) it is observed that the magnetization is decreased (increased) by tension (compression) if the magnetostriction ($\Delta l/l$) is negative (positive) when $\partial\sigma$ is positive (negative). Since CFO is a negative magnetostrictive material the magnetization would be reduced by stress (tensile).

The CFO/MgO film was under in-plane tensile stress (see Table 1), due to the lateral stretching along the film plane which resulted in the a_η (8.403 Å) being larger than $a_\perp$ (8.386 Å). With the addition of a top PZT layer the in-plane residual stress might be increased which resulted in reduced magnetization in PZT/CFO/MgO. On the contrary, the CFO/STO film was under large in-plane compressive stress with $a_\perp$ (8.494 Å) larger than a_η (8.292 Å). With the deposition of the PZT layer, the stress was released making the a_η (8.330 Å) in PZT/CFO/STO larger than that in CFO/STO. Thus strain relaxation enhanced the magnetization in PZT/CFO/STO film. The results matched well with the negative magnetostriction of CFO.

An increase in the residual stress due to the top PZT layer on the CFO layer and its effect on magnetization has been reported earlier on the polycrystalline films grown on silicon [83]. Sim et. al. had suggested that the residual stress in the CFO films on Si could be intrinsic and associated with the orientation change or defect incorporation or non-equilibrium phase formation. However the stress mechanisms were complicated and difficult to quantify [83]. In this work the residual stress could be estimated due to epitaxial growth. The investigation may provide a comprehensive direction towards tailoring the magnetic anisotropy of CFO epitaxial thin films for potential device applications.

Conclusions:

In conclusion, epitaxial bilayers of CFO and PZT were successfully grown on single crystal substrates MgO and STO substrates by PLD technique. The films grown on MgO (100) showed better in-plane epitaxy compared to the films grown on STO (100). In-plane strain on the CFO film grown on MgO increased with the deposition of PZT layer on top. This increase in stress in the CFO layer in PZT/CFO/MgO resulted in lowered saturation magnetization compared to the CFO/MgO film. In the case of the films grown on STO (100), the strain was already high in the CFO/SO film due to the larger film-substrate lattice mismatch. With the deposition of the PZT top layer the in-plane strain reduced slightly, which in turn resulted in higher saturation magnetization. The strain-modulated magnetism suggested possible

magnetoelastic coupling in these bilayers. This work provides useful insight into the role of interfacial stress in epitaxial CFO-PZT bilayers.

(c) Enhancement of ferroelectricity in V-doped ZnO:

We report evidence of enhancement in ferroelectricity in thin films of vanadium (V) doped ZnO grown at higher oxygen pressures. This process reduces the intrinsic oxygen deficiencies and the material becomes very insulating, which in turn lowers the leakage current through the ferroelectric capacitor.   2 at. % V doped ZnO films with thicknesses of approximately 1 μm were grown epitaxially on c-cut sapphire (Al_2O_3) (0001) at a growth temperature of 600°C. X-ray analysis showed the layers to be epitaxial where the (0002) diffraction peak had a rocking curve FWHM below 1°. The films with higher oxygen pressure were more insulating than those grown with lower oxygen pressure. The saturation polarization was seen to double when the growth pressure was increased from 300 mT to 500 mT. Time gated ICCD imaging of the ablated plasma during various O_2 pressures was used to study the plasma expansion dynamics and the effect on film quality.

Introduction:

Wide band gap semiconductor ZnO has sustained research interest for quite some time because of its multifunctionality like ferromagnetism [98], piezoelectricity [99], optoelectronic [100], gas sensing [101], photocatalysis [102] etc. In this work we investigate the piezoelectricity and spontaneous polarization properties of ZnO and how it can be affected by dopants and growth conditions.   It has been found that ZnO has the strongest piezoelectric response among the tetrahedrally bonded semiconductors [103]. This property of ZnO makes it a suitable material for technological application that require strong electromechanical coupling such as sensors and actuators [104]. Recently, Yang et al. [104, 105] reported an electromechanical d_{33} coefficient of V-doped ZnO to be as high as 110pC/N. This value is an order of magnitude higher compared to the d_{33} coefficient of bulk ZnO [104] which is 9.9 pC/N. Yang et. al. further showed that the d_{33} coefficient has a maximum value for 2.5 at. % of V doping. Another significant property due to V doping is reported to be the switchable spontaneous polarization. A butterfly like displacement graph is reported as the signature of spontaneous polarization [105]. Doping divalent cation Zn sites by V ions creates a mixed valency as well as strain in the original ZnO hexagonal structure because of the reduced ionic size of vanadium. It is reported that the V ions which replace the Zn sites are in 5^+ valency state [106]. The mixed valency creates charge polarity between Zn-O and V-O bonds. This charge polarity and the rotation of the nonlinear V-O bonds w.r.t. Z-O bonds under electric field gives rise to the enhanced ferroelectricity [105].

In addition to V-doping, the films have to be insulating to further improve ferroelectric properties by reducing the leakage current. The conductivity in ZnO arises from oxygen deficiencies and thus the oxygen vacancies have to be reduced to enhance film resistance. We have grown epitaxial V-doped ZnO film under different oxygen pressure from 100 mT to 500 mT using pulsed laser ablation to investigate the effect of growth parameters on the film resistance. The films with higher oxygen pressure are more insulating than the one grown with lower oxygen pressure. The saturation polarization is higher for the film grown at higher pressure.

Experimental details:

Thin films of V doped ZnO were grown using pulsed laser ablation technique. For this a ceramic target of $Zn_{1-x}V_xO$ (x=0.02) was first prepared by standard solid state reaction method. Pure (99.99%) powders of ZnO and V_2O_5 were mixed in stoichiometric proportion and well ground and mixed before calcination in air for 6 hrs at 600°C. The calcined mixture was ground again and cold pressed under a pressure of 90 MPa into a one inch diameter and a quarter inch thick target. The pressed target was sintered at 1000°C in air for 12 hrs. A KrF excimer laser of wavelength 248 nm was used to ablate the compressed target. The chamber was pumped to a base pressure of 4 x 10^{-6} Torr and the films were grown at a pressure of 100 mT to 500mTorr of oxygen while heating the substrate to 600°C. The repetition rate of the laser pulse was kept at 10 Hz and the fluence at the target surface was chosen to be 2J/cm^2. The distance between the substrate and the target was 4 cm. Under these growth conditions, the rate of growth was measured to be approximately 0.1 Å/pulse. The film crystallinity and orientation were assessed by conventional θ-2θ x-ray diffraction (XRD) methods. The polarization hysteresis measurements were performed using the Precision LC from Radiant Technologies, which included a Sawyer-Tower Circuit.

Results and discussion:

The growth parameters were optimized by first studying the laser-target interaction. At the same time, the ablated plume profile was studied at various combinations of laser fluences and oxygen pressure. The following subsections provide a detailed account of laser-target interaction, characterization of the thin films grown and the observed electric polarization as a function of oxygen pressure during the growth.

Laser-target interaction:
Laser pulses of varying fluences from 1J/cm^2 to 5J/cm^2 were impinged separately on the fresh target surfaces to study the target surface morphology and the stoichiometry by using energy dispersive spectroscopy (EDS). Figure 48 shows an SEM micrograph of the zinc oxide target surface before and after the laser ablation. The ablated region shows a melted surface with hexagonal facets characteristic of zinc oxide. To study how the Vanadium (V) content changes in the target, EDS was performed on V-doped ZnO target surface irradiated with laser fluences from 1J/cm^2 to 5J/cm^2. The Vanadium content did not change with the fluence. The standard deviation for the Vanadium content (at.%) on the target after laser ablation was 0.21. However, for larger fluence, large particulates appeared to come out of the target surface leaving behind voids of micron sizes. Although Vanadium content remained same for all the fluences, the ablated target surface looked smoothest and almost void free as shown in Figure 48 for low fluence (2J/cm$^{2)}$. Thus 2J/cm^2 fluence was fixed for the film growth and the thin films grown had smooth surface and better crystallinity.
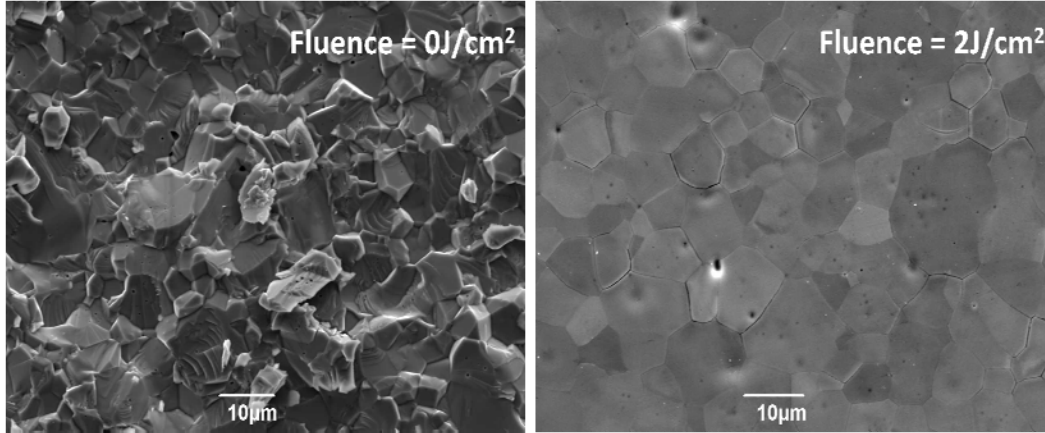
Fig. 48: SEM pictures of unablated (left) and 2J/cm^2 ablated surface of ZnO ceramic target. 1000 laser pulses were used to ablate the target

Thin film growth:

To reduce the oxygen deficiency and eventually to reduce leakage current through the ferroelectric capacitor we grew thin films with various oxygen pressures from 100 mT to 500 mT. Keeping the laser fluence at 2J/cm^2, the laser ablated plumes were photographed by time gated Intensified Charge Coupled Detector (ICCD).

The induced plasma images were taken for the duration of 20µs to capture the full expansion profile for all oxygen pressures from 100 mT to 500 mT. As shown in Fig.49, the plasma is more expanded for 100 mT oxygen pressure, but gets confined in forward direction as the oxygen pressure increases. Thin films of 2 at. % V-doped ZnO were grown at 100 mT, 300mT and 500mT on sapphire substrate heated at 600°C. As the growth pressure rises, more particles appear on the surface (Fig.49). For higher O_2, the plasma plume is more forward-directed and this tends to create nucleation sites on the film where the particles appear to grow faster. Total emission intensity for 100 mT O_2 was the greatest, indicating highest excitation and ionization. Total emission intensity of 300 mT O_2 is 62% of 100mT O_2 and that of 500 mT O_2 is 45%. In addition the full width at half maximum (FWHM) for 500mT of O_2 pressure is the lowest (0.54 cm) at 2 cm from the target which in turn leads to a lower growth profile. A roughness analysis was performed on these films. It is found that the root mean square roughness (Rq) for the films grown at 100mT, 300mT and 500mT was 17.5 nm, 33.5 nm and 55.8 nm, respectively. The Rq increased by three fold as the oxygen pressure increased from 100 mT to 500 mT.

To confirm the crystallinity and the epitaxy, X-ray diffraction measurements were done. Figure 49 shows the standard θ-2θ scan of the three films (grown at 100 mT, 300mT and 500mT) grown on c-cut sapphire (Al_2O_3) (0001) in which ZnO grows epitaxial along the (002) direction.
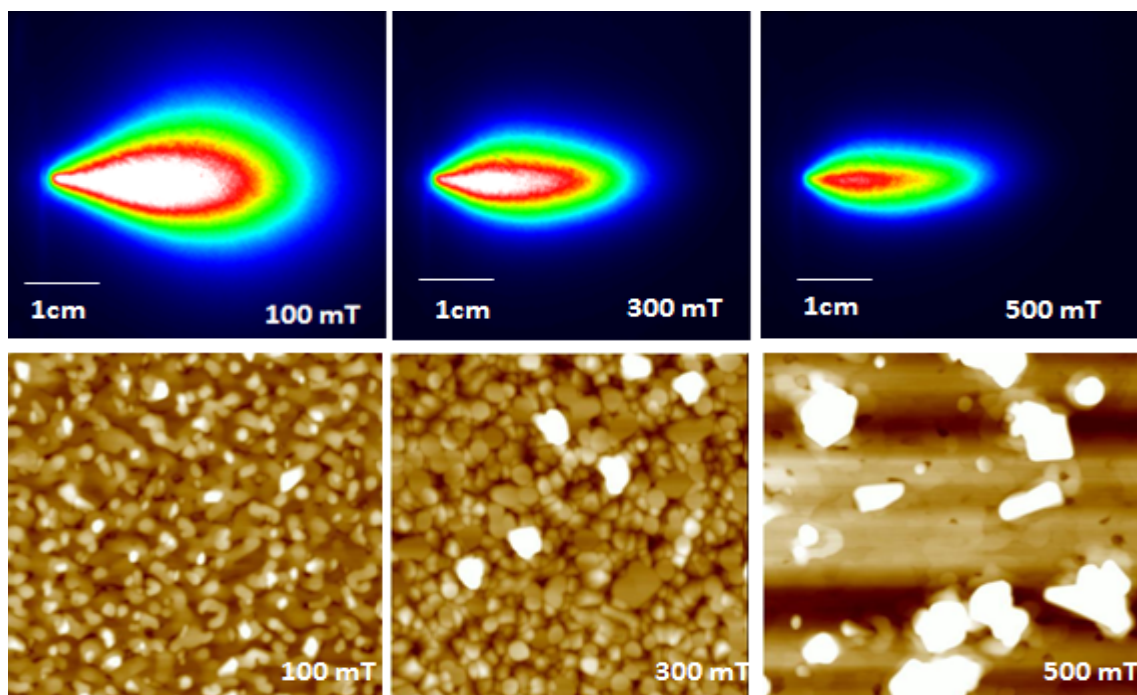
Fig. 49: Laser ablated plume images taken by ICCD for various oxygen pressures. 2 cm from the target, the FWHMs of the expansion profiles for 100mT, 300mT and 500mT Oxygen (O_2) pressure are 1.10 cm, 0.71 cm and 0.54 cm respectively. The lower panel shows the corresponding AFM images (5µm x 5µm) of the films grown on c-cut sapphire (Al_2O_3) substrates.
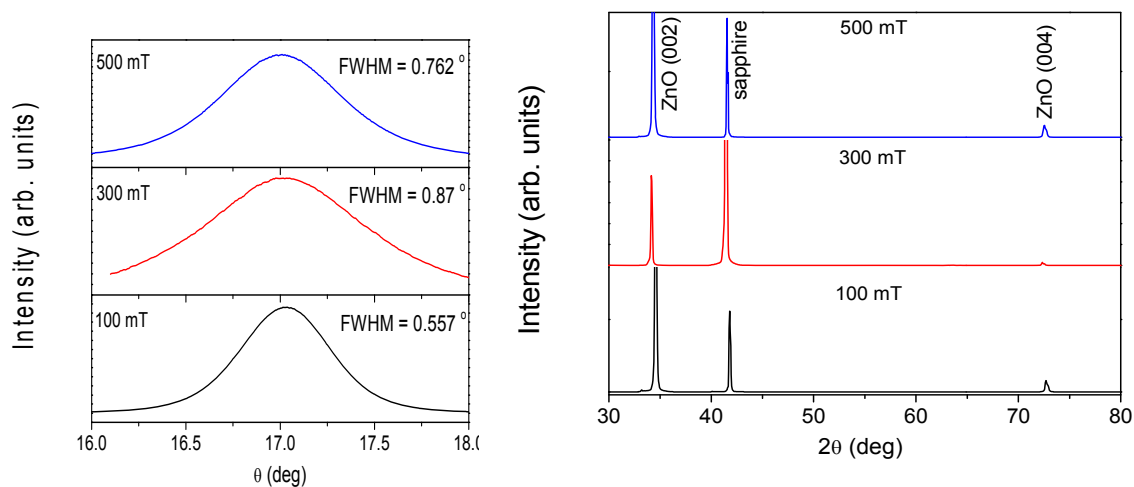
Fig. 50: XRD peaks of 2 at. % V-doped ZnO grown on c-cut sapphire substrate. The right panel shows the rocking curves of (002) ZnO peak showing FWHMs.

All the films show (002) orientation. The rocking curves of the lattice-matched films are below 1 degree. However, FWHMs of the films grown at 300mT and 500mT are higher than the one grown at 100 mT (Fig.50).

Electric polarization:

The resistivity and carrier concentrations were obtained by using Van der Pauw method. The films grown at higher O_2 pressure were more insulating and had less number of charge carriers. The results are summarized in Table 3. Since the film grown at 500mT was very insulating, it was not possible to obtain reliable data. As we can see from the table, the film grown at 100mT has low resistivity whereas the resistivity of the film grown at 300mT is increased by five orders of magnitude. With the increase in resistivity of 300 mT film, the carrier concentration has reduced by about 4 orders of magnitude compared to the film grown at 100 mT of O_2 pressure.

Table 3: Resistivity and Hall measurement using Van der Pauw Technique

Background Pressure (mT)	Sheet resistance $R_S(\Omega)$	Resistivity $\rho(\Omega cm)$	Carrier Conc. n_C (cm^{-3})	Mobility μ_H (cm^2/Vs)
100	2.76×10^2	8.82×10^{-3}	2.66×10^{19}	26.51
200	2.38×10^5	7.61	3.08×10^{17}	2.67
300	1.19×10^7	4.53×10^2	3.76×10^{15}	3.65

For electric polarization measurement, we fabricated a capacitor by depositing gold palladium electrodes on top of the film. Planar electrodes were used for both top and bottom electrodes because of the insulating substrate. Fig.51 shows the electric polarization for the three films. It can be seen that the polarization is the largest for the film grown at 500mT. It is reported that V doped ZnO thin films show ferroelectricity due to the strain in the Zn-O bond where the Zn site is replaced by the smaller size V ion
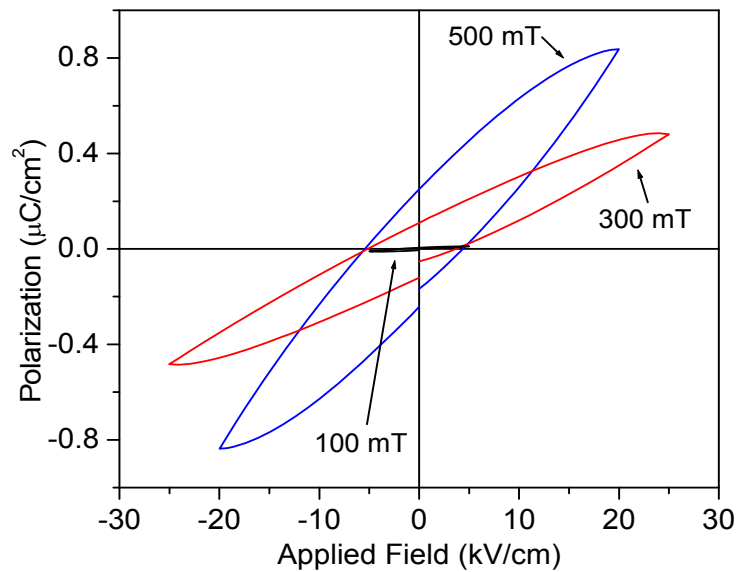

Fig. 51: Electric Polarization as a function of applied electric field for the films grown at various oxygen pressures

[107]. We further enhanced this polarization by growing the films at oxygen reach environment. With high oxygen pressure, we could grow films with less oxygen deficiency thus reducing the defects across the film. This reduced the leakage through the capacitor and we could measure the polarization at higher drive voltage.

The maximum value of saturation is approximately $1\mu C/cm^2$ which is comparable to the published result [108]. Other parameters like the coercivities, remanant polarizations are summarized in Table 4 below.

Table 4: Saturation and remanant polarization and coercivities

Background Pressure (mT)	Saturation Polarization P_S ($\mu C/cm^2$)	Remnant Polarization P_R ($\mu C/cm^2$)	Coercive Field E_C (kV/cm)
100	0.01	0.0045	2.05
300	0.48	0.1	4.4
500	0.83	0.24	4.9

Conclusion:

Ferroelectric switching was obtained in ZnO by doping it with penta-valent V ion. Higher saturation polarization was obtained for the film grown at higher oxygen pressure because of the more insulating nature of the film. The ICCD imaging of the plasma expansion showed broader expansion for low O_2 pressure and narrower expansion for higher O_2 pressure, which correlated well with the roughness of the film surface as obtained from AFM measurement.

[D]   Flexible photonic materials for solar-based energy sources

PbSe/TiO$_2$/PEDOT : PSS structures for flexible solar devices:

Introduction:

In this project PbSe quantum dots (QDs), titanium dioxide (TiO$_2$) nanorods and the semiconductor polymer Polyethylenedioxythiolphene (PEDOT) are combined to form a composite structure for harnessing solar energy. PbSe QDs have been synthesized from a novel procedure with 2 nm average diameter. The primary focus is to tune the size of the PbSe QDs such that the band gap off-set (0.35 eV) with the host TiO$_2$ nanorods would promote preferential injection of electrons to allow ballistic transport to the fluorine-doped tin oxide (FTO) electrode. PbS quantum dots with average diameter of 4 nm have been made in preparation for a comparative study with the PbSe/TiO$_2$ versus PbS/TiO$_2$ nanocomposites.   Several samples of

TiO$_2$ nanorods of average length 2 μm and well controlled density (for maximum PbSe monolayer distribution) have been prepared. PbS at the 4 nm range is well-suited for e$^-$ injection into carbon nanotubes (CNTs), so a CVD system has been put together in order to synthesize in-house CNTs of various wall thickness and lengths. Utilizing seeded growth techniques vertically aligned CNTs have been produced, from which the PbS/CNT [109] structure is being studied. All of the aforementioned structures are highly reproducible. Figure 52 shows the schematic diagram for Homo**,** Lumo, and work functions of the CNT nano-composite and Figure 53 is the band diagram with PbSe QDs, indicating relevant level transitions of carriers.
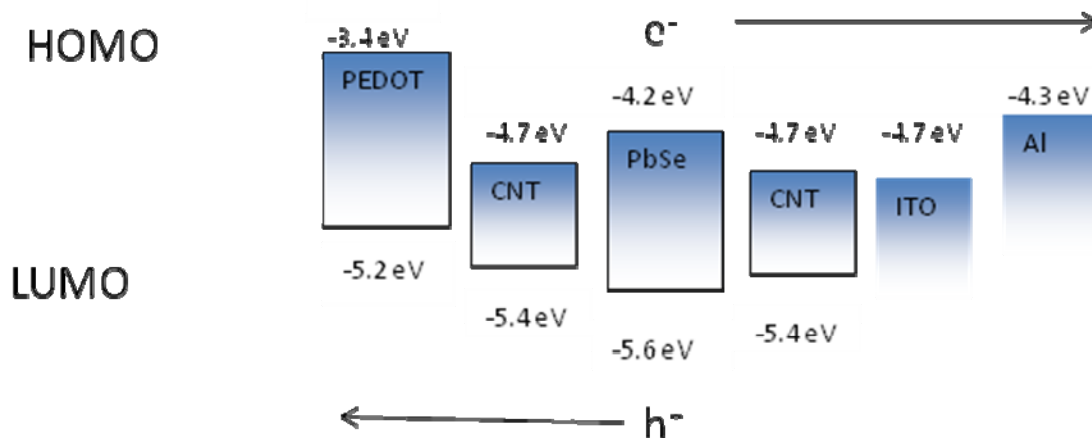

Fig. 52: HOMO, LUMO, and work functions of the CNT nano-composite.
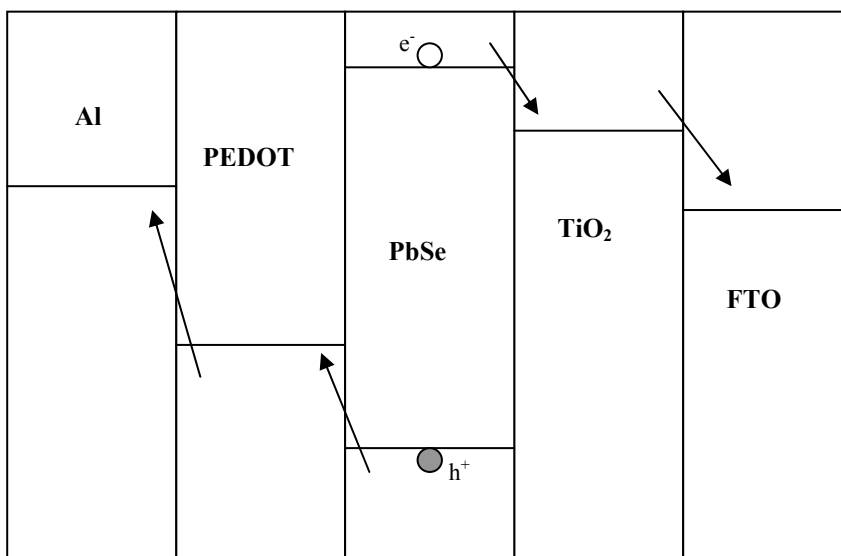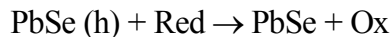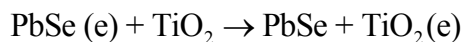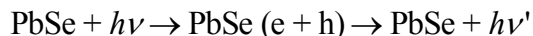

Fig. 53: Ideal band diagram with PbSe QDs, indicating relevant level transitions of carriers.

The following sequence will produce the current density from the structures being built, with the example of PbSe/TiO$_2$/PEDOT:PSS structure.

$$PbSe + h\nu \rightarrow PbSe\ (e + h) \rightarrow PbSe + h\nu'$$
$$PbSe\ (e) + TiO_2 \rightarrow PbSe + TiO_2(e)$$
$$PbSe\ (h) + Red \rightarrow PbSe + Ox$$

PEDOT: PSS Polymer films:

The chemical structure of Polyethylenedioxythiolphene Polystyrenesulfunate (PEDOT: PSS) is shown in Fig. 54.   PEDOT:PSS has been chosen as the redox coupler for several reasons. The sp^2 hybrid PEDOT [110] has a band gap of 1.6 -1.7 eV, precisely what is needed to transport holes from the excitons created in 2 nm diameter QDs efficiently. Due to the Pierels instability the C – C bond length is greater than that of the C = C bond length, leaving 2 sub-bands, i.e. a completely filled valence (HOMO) and an empty conduction (LUMO) separated by an energy gap. This semiconducting nature is the primary reason for using this polymer through which the primary transport mechanism is known to be hopping, with a several orders of magnitude difference in the longitudinal and transverse directions.

The overall goal of the solar technology project is to produce low-cost high-efficiency solar cells. High efficiency is the first of these two characteristics being pursued. PbSe QDs with diameters of 2 nm have a band-gap of 1.7 eV. The UV portion of the solar spectrum is divided into three parts, ranging in wavelength from roughly 100 nm to 250nm to 400nm,

PEDOT sp^2 hybrid with double bonds
which are shorter than single bonds
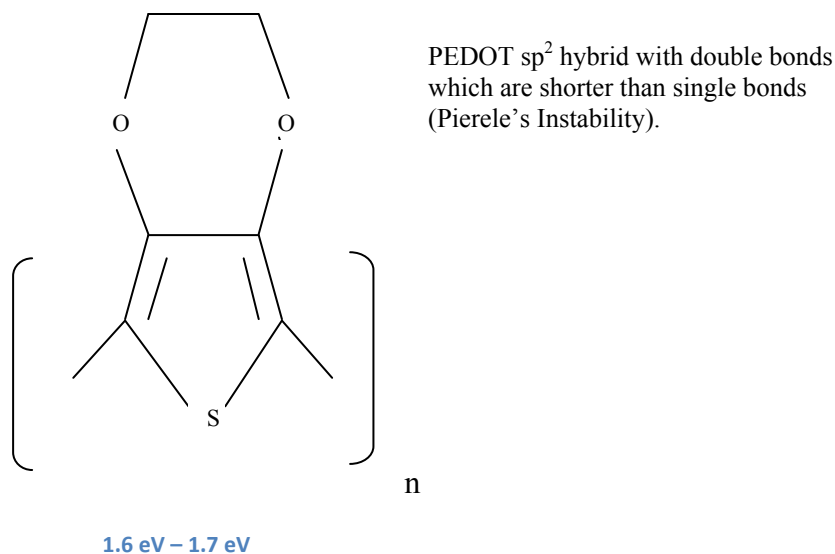(Pierele's Instability).

1.6 eV – 1.7 eV

Fig. 54: Chemical structure of PEDOT : PSS, the polymer used to promote hole mobility in the solar devices.

corresponding to E_{UV} = 12.4 eV, 4.6 eV, and 3.1 eV for the respective ranges. This translates into multiples of the band-gap of 7.29 E_g, 2.9 E_g, and 1.8 E_g. It is known that excitons produced

from incident photons with multiples of E_g are capable of producing multiple exciton generation (MEG). Production of larger sized (4 nm) quantum dots is a profitable venture as the visible range of the solar spectrum can be utilized to produce MEG from a larger portion of the solar spectrum, albeit with a lower multiple of the band gap in TiO_2. For that reason the larger sized QDs are reserved for carbon nanotube structures, which are more amenable to charge transfer from the relatively larger sized sensitizers. From this vantage point the potential of total quantum efficiencies exceeding 100% are being pursued.

The new Laser Assisted Spray process chamber for co-deposition of QDs and polymer films is shown in Fig. 55.
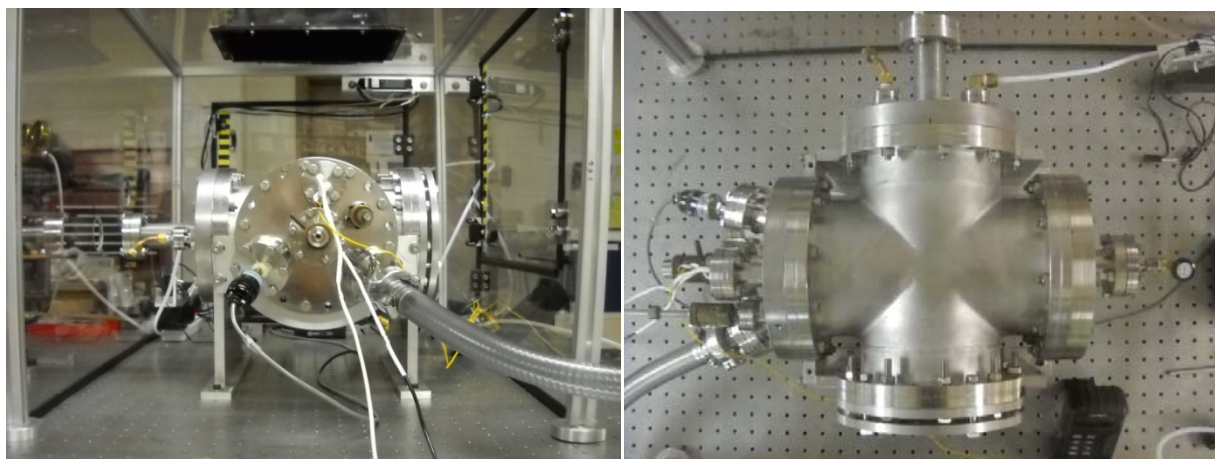
Fig. 55: Laser Assisted Spray process chamber top and side views

TiO_2 nanorods are deposited on fluorine doped tin oxide films by a hydrothermal process that was described in a previous report. We have used the laser assisted spray (LAS) deposition process to deposit PbSe QDs over the vertically aligned TiO_2 nanorods. Figure 56 (a) shows an SEM image of TiO_2 nanorods deposited on a substrate. Figure 56 (b) is a high resolution TEM image showing the single crystal like TiO_2 nanorods and PbSe particles attached to the rod. The boundary of the QD is highlighted.

Subsequently, a layer of the p-type polymer PEDOT was spin-coated over the QD layer to form the composite device structure shown in Figure 57 (a). The photocurrent generated by the composite structure was investigated by exposing the device to different light intensities from a white light source. As shown in the graph in Figure 57 (b) a significant photocurrent was generated by the cell.

In summary, laser assisted spray process was used to deposit PbSe QDs on crystalline TiO_2 nanorods grown by a hydrothermal process. Absence of surfactants enhanced exciton dissociation and charge transport. A significant photocurrent was produced by the composite TiO_2-QD-polymer structures.
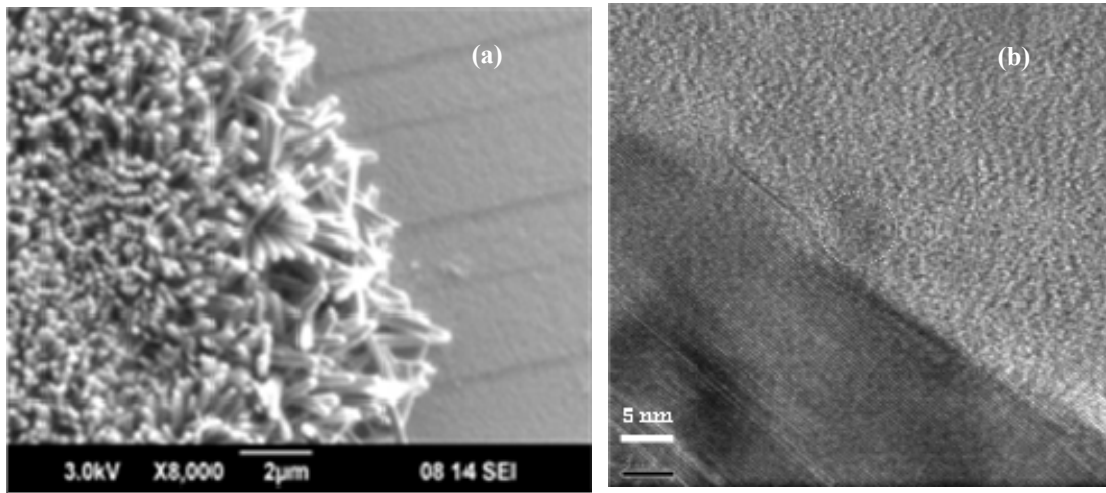
Fig. 56: (a) SEM images of vertically aligned TiO$_2$ nanotubes and (b) TEM image of a TiO$_2$-PbSe composite. The circle indicates the position of a QD.
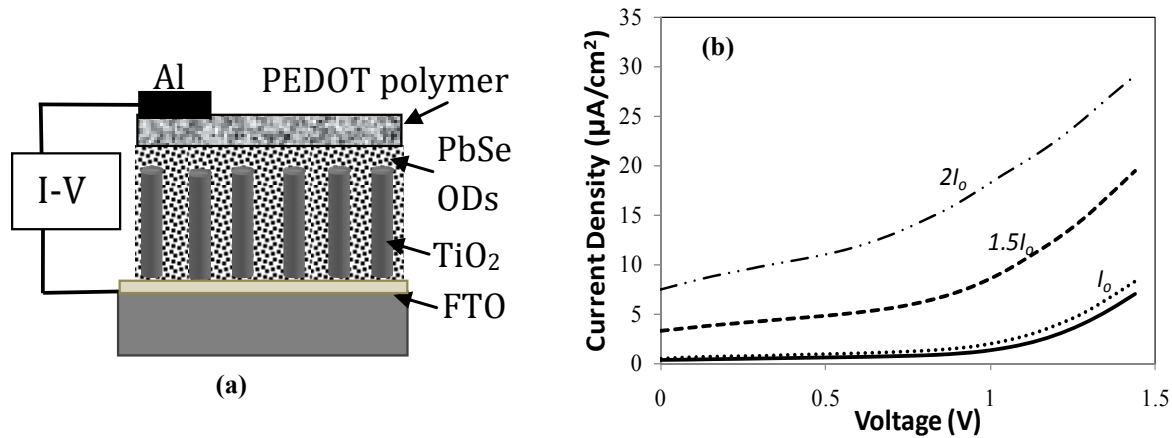
Fig. 57: (a) TiO$_2$-PbSe QD-polymer composite cell structure and, (b) photocurrent at different illumination intensities.

Task III : Solid-state materials for power generation and refrigeration

[E]   High performance nanofabricated thermoelectric materials for power generation

The research accomplishments in this task are described below.

- Preparation of core-shell PbTe@Ag nanocrystals by a two-step solution phase synthesis process and optimization of the synthesis parameters. Preliminary studies with XRD and SEM are underway.
- Measurement and optimization: In the following we outline the synthesis and thermoelectric (TE) properties of Bi-doped PbTe nanocomposites.

- Preparation of Bi and Bi-Sb alloy nanocomposites starting from the respective nanocrystals.
- Measuring the TE properties as well as structural and calorimetric analyses of nanocomposites.
- Oxide materials with potential for TE applications.
- Comparing our experimental results with theoretical modeling.

Semiconductor thermoelectric materials:

Synthesis:

PbTe nancrystal synthesis with different grain sizes: PbTe nanocrystals were synthesized with different sizes in high-yield employing two different approaches; low temperature reverse microemulsion (ME) with 25-30 nm crystals and direct precipitation (DP) synthesis with 50 nm (DP-small) and 100 nm (DP-large) crystals.[111, 112] Na-AOT, water and n-hexane, each of high purity grades, were used as the surfactant, water phase, and oil phase, respectively, for the microemulsion process. Pb-acetate, Na-tellurite and Bi-nitrate were used as the Pb, Te and Bi sources, respectively. A tellurium alkaline aqueous solution and lead acetate trihydrate were used for the direct precipitation process. The dark black precipitate in each case was separated out repeatedly with water and ethanol. The carrier concentrations were modified by directly doping the PbTe nanocrystals with Bi (Bi-nitrate) prior to the densification procedure. Nominal doping percentages varied from 1-40 mol % in order to investigate their transport properties as a function of doping.

$Bi_2Se_xTe_{3-x}$ and $Sb_2Se_xTe_{3-x}$ Nanocrystal synthesis: Bismuth telluride and antimony telluride Se-doped nanocrystals were prepared by ethyleneglycol mediated solvothermal process. For the synthesis, Bismuth nitrate ($Bi(NO_3)_3.5H_2O$), antimony(III) chloride ($SbCl_3$) and selenium dioxide (SeO_2) were chosen as the Bi, Sb and Se sources, respectively. Sodium tellurite (Na_2TeO_3) was the tellurium source for all syntheses. Monohydrate hydrazine hydrate ($N_2H_4.H_2O$) was used as a reducing agent and pH regulator to yield the desired nanocrystals. All the chemicals were analytical grade and were used without further purification. Selenium doping was carried out with varying Te:Se atomic ratios (Te:Se = 2.9:0.1, 2.8.0.2 and 2.7:0.3).

Bi-Sb Alloy Nanocrystals synthesis: To synthesize Bi-Sb alloy nanocrystals of specific stoichiometry, first Bismuth nitrate ($Bi(NO_3)_3.5H_2O$), antimony(III) chloride ($SbCl_3$) and polyvinyl pyrrolidone (PVP, M.W. 40,000) were dissolved in ethyleneglycol at a low temperature (~ 60 °C). Reductant sodium borohydride ($NaBH_4$) was then added to the solution and the solution was refluxed from 15-60 min at 150 °C. Black and/or dark grey precipitates were collected and washed several times with ethanol to wash out the impurities.

In all three processes, the nanocrystals were dried and used for the structural characterizations by X-ray diffraction (XRD), Scanning electron microscopy (SEM), Transmission Electron Microscope (TEM), and Energy dispersive x-ray analysis (EDS). The nanocrystals were densified into bulk polycrystalline TE materials with nano-scale grains by a Spark Plasma Sintering (SPS). The densified TE materials were cut into 2 x 2 x 5 mm^3 parallelepipeds for transport property measurements.

Results:

PbTe nanocomposites: Higher percentages of different sized Bi-doped PbTe nanocrystals did not show Bi related impurities in the XRD spectra. This along with EDS results suggests successful Se doping (Fig. 58a-c). The XRD peaks for the 100 nm Bi-doped PbTe nanocrystals are sharper
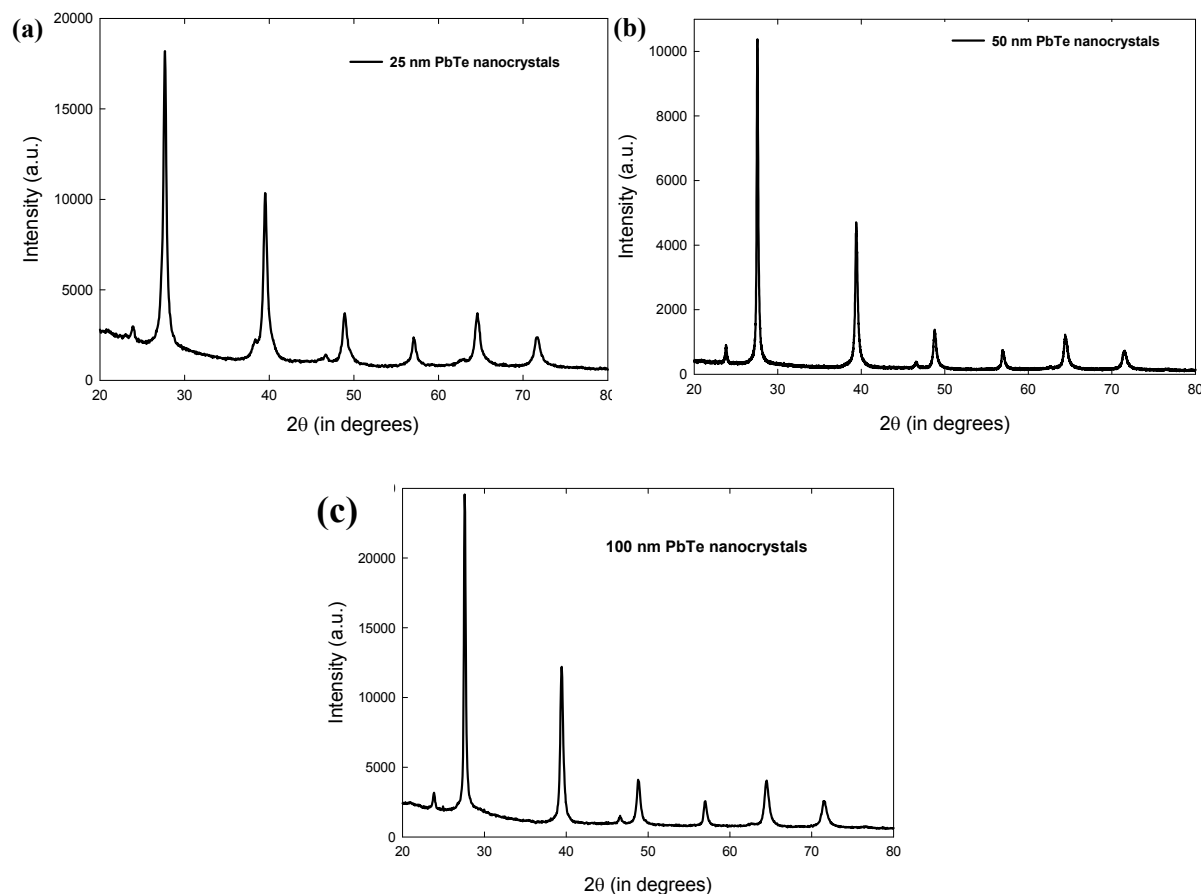
Fig. 58: Typical XRD spectra of different grain sized heavily Bi-doped PbTe specimens. The XRD patterns indicate the phase purity of the prepared nanocrystals.

than that for the 50 nm and 25 nm sized PbTe nanocrystals, a qualitative corroboration of the differing grain sizes. Nanocrystal sizes were calculated using the Scherrer equation and the results were corroborated by SEM images of the nanocrystals. After densification, the grains 'grew' to 30-50 nm for densification of the nanocrystals synthesized by ME, and 50-100 nm for those synthesized by DP-small and 100-300 nm for DP-large. Composition analysis of the nanocrystal specimens were carried out by EDS. Increasing the nominal Bi concentration increased Bi doping. Bi doped PbTe nanocomposites did not show any impurities after densification, from XRD results. SEM images indicate the presence of nano-scale grains. SEM images of fractured pellet surfaces indicated densities of 95-98% of that of the theoretical density of PbTe. Transport properties measurements are shown in Figures 59-61. The specimens showed an increasing electrical conductivity with doping. From Figure 59(a) and (b), the temperature

dependence of resistivity, ρ, indicates $\Delta\rho/\Delta T > 0$ above 150K, indicating metallic conduction above ~150K, while $\Delta\rho/\Delta T < 0$ below 150K.

Fig. 59: Temperature dependent resistivity for representative undoped and Bi doped PbTe nanocomposites. The nominal Bi doping concentrations are indicated.
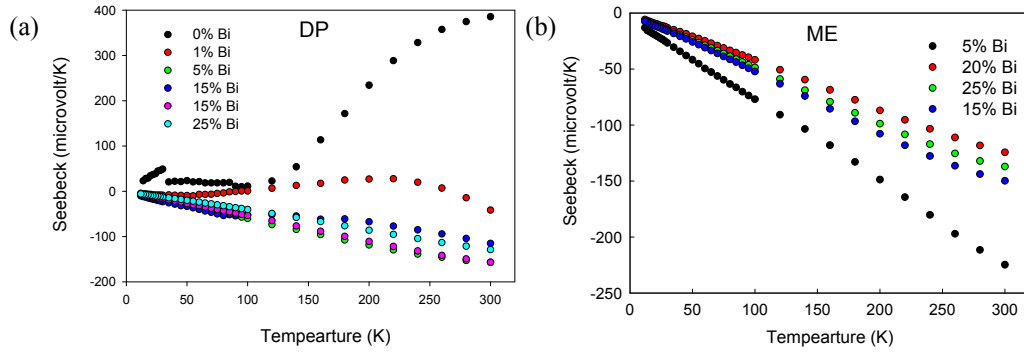
Fig. 60: Temperature dependent Seebeck coefficient for representative undoped and Bi doped PbTe nanocomposites. The nominal Bi doping concentrations are indicated.

With increasing Bi doping, a systematic decrease in room temperature resistivity values were observed, presumably indicating higher electron concentrations with Bi doping. Figure 60(a) and (b) shows the Seebeck coefficient, S, as a function of temperature for the Bi-doped PbTe specimens. The undoped PbTe nanocomposite shows positive S values, whereas the Bi doped specimens show $S < 0$ suggesting an excess of electron carriers in the doped nanocomposites. For the 1% Bi doped PbTe nanocomposite, conduction from holes and electrons may be present as can be assumed from the change in sign and slope of S, in addition to the high ρ values. However, for higher concentrations of Bi, the PbTe nanocomposites show larger absolute S values and lower ρ, indicating an increased electron concentration. Hall measurements currently underway will reveal the doping in these specimens.

All the Bi-doped PbTe nanocomposites possessed relatively low thermal conductivity, κ, as shown in Figure 61(a) and (b). The temperature dependence of κ for all specimens is similar to that of bulk polycrystalline PbTe with a maxima occurring between 20 K and 30 K.
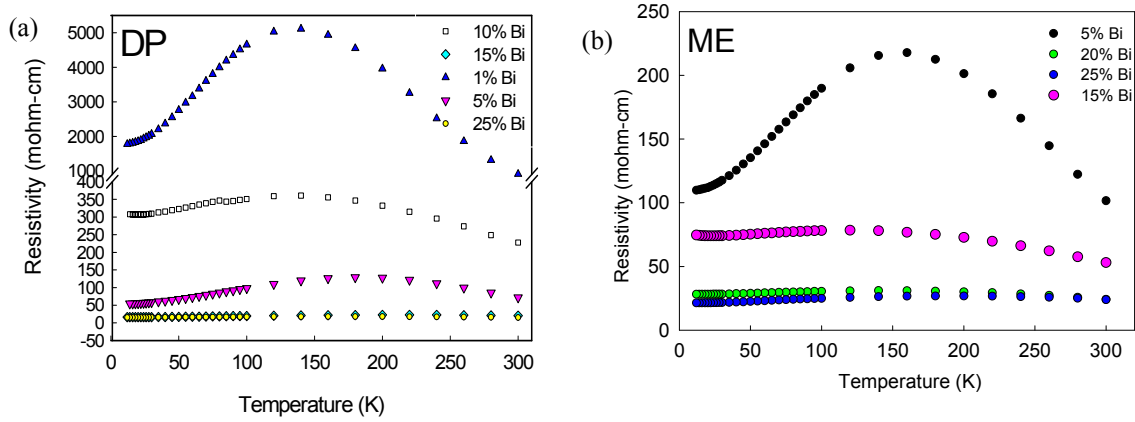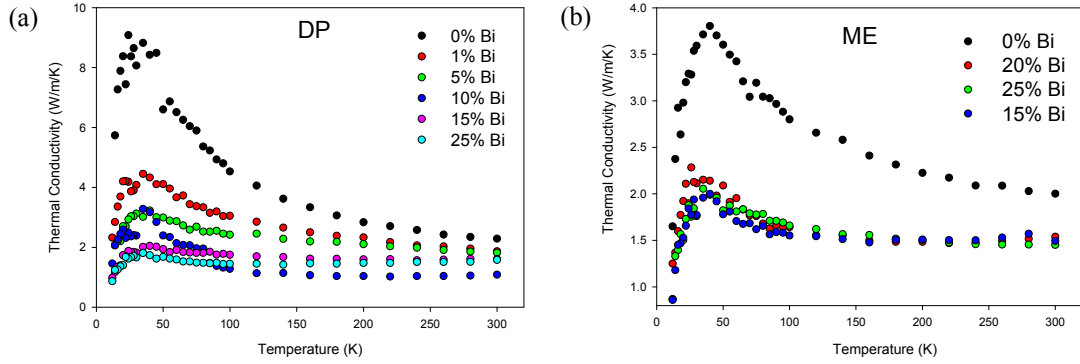
Fig. 61: Temperature dependent thermal conductivity for undoped and Bi doped PbTe nanocomposites. The nominal Bi doping concentrations are indicated.

$Bi_{0.5}Sb_{1.5}Te_3$ alloy nanocomposites:

Structural studies show successful preparation of Se doped $Bi_{0.5}Sb_{1.5}Te_3$ alloy nanocrystals of ~18-25 nm in diameter. Representative XRD spectra of the Se doped Bi_2Te_3, $Bi_{0.5}Sb_{1.5}Te_3$ and Sb_2Te_3 nanocrystals are shown in Figures 62(a)-(c). The spectra did not indicate a secondary phase. Nanocrystallite sizes calculated from the Debye-Scherrer formula were ~18-25 nm. Crystal sizes estimated from SEM images corroborate these results. Figure 63(a) and (b) show the representative SEM images of the Se doped $Bi_{0.5}Sb_{1.5}Te_3$ and Sb_2Te_3 nanocrystals. Both undoped and Se doped Bi_2Te_3 and $Bi_{0.5}Sb_{1.5}Te_3$ nanocrystals are particulate in shape where as undoped and Se doped Sb_2Te_3 nanocrystals are found to be platelets ~5 nm thick. Room temperature S values are shown in Table 5.

Table 5: Room temperature Seebeck and density values of the specimens

Specimen	Density	Seebeck (microvolt/K)	Specimen	Density	Seebeck (microvolt/K)
Bi_2Te_3	87	-154	$Sb_2Te_{2.9}Se_{0.1}$	89	147
$Bi_2Te_{2.9}Se_{0.1}$	88	-102	$Bi_{0.5}Sb_{1.5}Te_{2.8}Se_{0.2}$	87	139
Sb_2Te_3	86	157	$Bi_{0.5}Sb_{1.5}Te_{2.9}Se_{0.1}$	85	117
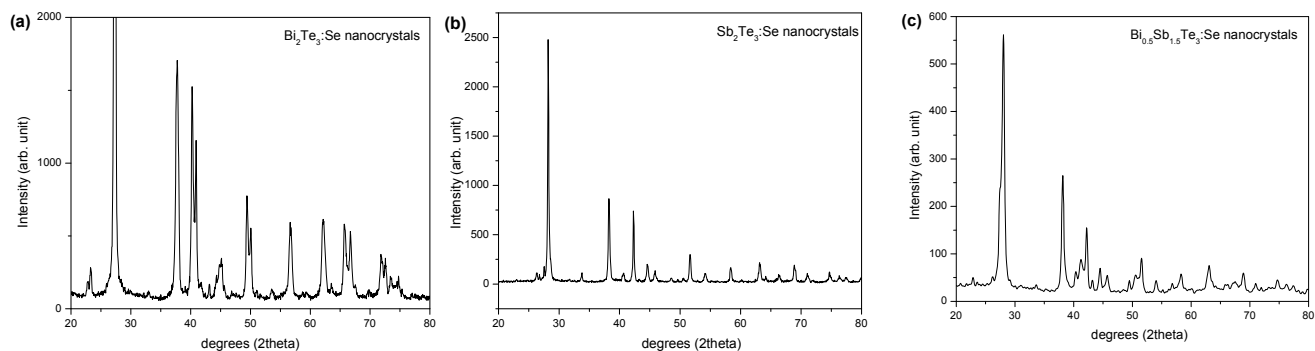
Fig. 62: XRD spectra of the representative Bi-Sb-Te-Se specimens (a) Bi_2Te_3:Se (b) Sb_2Te_3:Se and (c) $Bi_{0.5}Sb_{1.5}Te_3$:Se nanocrystals .
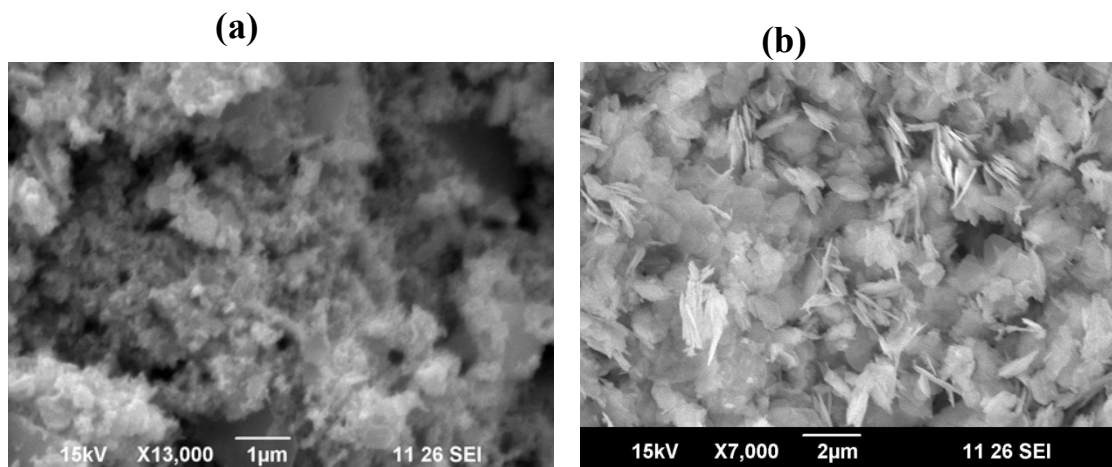
Fig. 63: SEM images of the representative Bi-Sb-Te-Se specimens (a) $Bi_{0.5}Sb_{1.5}Te_3$:Se nanocrystals and (b) Sb_2Te_3:Se nanocrystals .

Bi-Sb nanocrystals

XRD spectra of phase-pure Bi and Bi-Sb nanocrystals are shown in Figure 64. The spectra indicate the formation of Bi-Sb. The nanocrystallites ranged in size from 30 nm to 50 nm. EDS analysis indicated a Bi:Sb ratio of 0.88:0.12 for the Bi-Sb alloy as shown in Figure 65. Both nanocrystals possess a rhombohedral morphology, as shown in TEM images. A representative TEM micrograph of the Bi-Sb nanocrystals is shown in Figure 65.
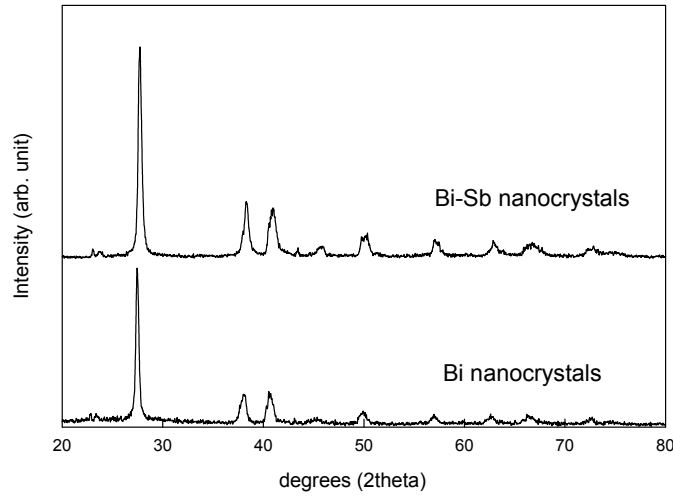
Fig. 64. XRD spectra of the pure Bi and $Bi_{0.88}Sb_{0.12}$ nanocrystals.
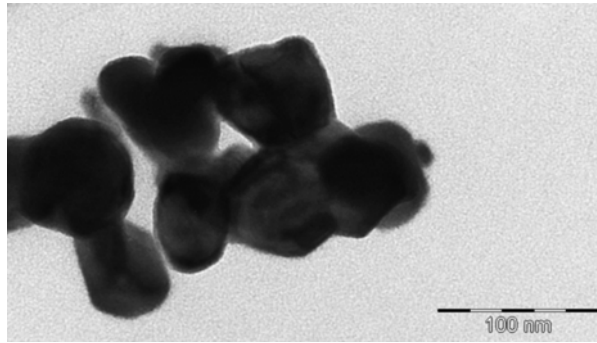
Fig. 65: TEM image of the representative $Bi_{0.88}Sb_{.12}$ nanocrystals.

Modeling the transport properties of n-type Bi-doped PbTe nano-composites were also performed. The model [113, 114] is represented as a collection of grains whose grain boundaries result in the formation of potential barriers with an average height and width, as well as grain size. A key issue is the additional scattering mechanism introducing a relaxation time for the carrier/interface scattering. Our goal was to find a set of parameters relevant to the experimental settings in order to achieve the best possible fit between experiment and theory for these materials [115]. In Figure 66 the results for ρ as a function of temperature for different percentages of Bi doping n-type PbTe nanocomposites are shown. Similar modeling is currently underway for S and κ.
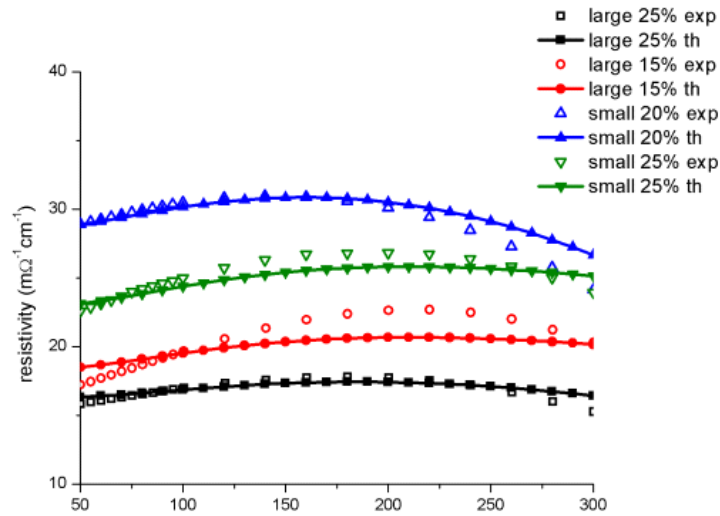
Fig. 66: Resistivity versus temperature for samples with different granular sizes and concentrations. Experimental and theoretical curves are shown.

Oxide thermoelectric materials:

This year we also focussed on a new material system from the family of layered oxides generally referred to as delafossites. These derive their name from the mineral $CuFeO_2$ [6], with which their crystal structures are isotypic. Denoted by the general chemical formula ABO_2, the crystal structures of these materials (Figure 67) are characterized by layers of distorted, edge-sharing octahedra with oxygen coordinating metal cations (B = typically transition or group 13 elements) separated by planar layers of a transition metal (A = typically Cu, Ag, Pd, or Pt) which are linearly coordinated along the c-axis by two oxygen sites. Characterized by a wide range of possible compositions, the delafossite oxides also exhibit a significant richness in properties. Motivated by the relatively high electrical conductivities observed in some delafossite compounds [116-119], an investigation of these novel oxide materials for thermoelectric power generation applications was undertaken. Very recently, it has been suggested [120-122] that some delafossite compounds, in particular the composition $CuCoO_2$ [121], might be of interest as candidate oxide materials for thermoelectric power generation. To date the $CuCoO_2$ delafossite has not been experimentally well characterized.

$CuCoO_2$ has previously been prepared by hydrothermal [123] and solution-based [124] techniques, as well as thermal decomposition of copper-cobalt hydroxysalts [125]. Reactions of CuCl and $LiCoO_2$ were carried out in alumina crucibles, sealed inside evacuated silica tubes. $CuCoO_2$ was successfully prepared reproducibly by reaction at 590°C for 2 days. The resulting products were very fine, grayish powders consisting of $CuCoO_2$, with only small amounts of impurity phases. Figure 68 shows calculated and experimental p-XRD patterns, confirming the $CuCoO_2$ 3R-delafossite crystal structure. Weak reflections due to minor impurity phases CuO and $LiCoO_2$ are also indicated in Figure 68. As shown, all other peaks are indexed to the $CuCoO_2$ phase, with the positions and relative intensities in good agreement.
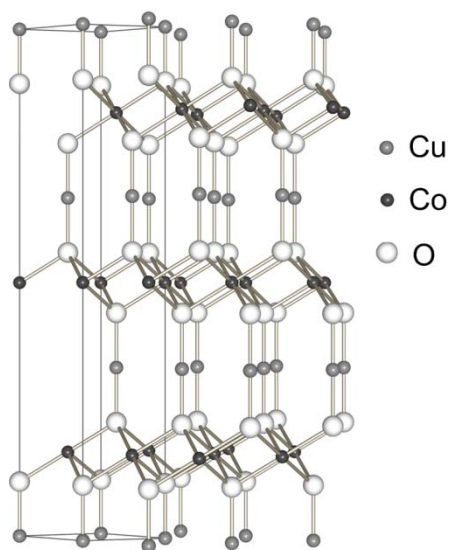
Fig. 67: A depiction of the CuCoO$_2$ 3R delafossite crystal structure. The rhombohedral unit cell is outlined at left.
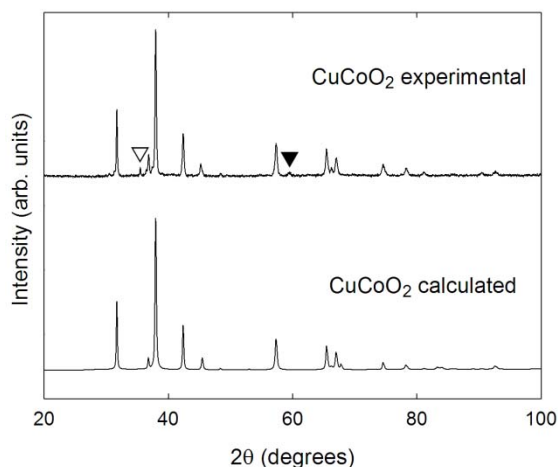
Fig. 68: Experimental (top) and calculated (bottom) powder X-ray diffraction patterns for a CuCoO$_2$ specimen synthesized at 590 ^{o}C. Weak reflections due to minor impurity phases of CuO ($\triangledown$) and LiCoO$_2$ ($\blacktriangledown$) are indicated.

Differential thermal analysis (DTA) and thermogravimetric (TG) data for a CuCoO$_2$ specimen in the range of 200°C to 1000°C are shown in Figure 69. No thermal events are observed until 680°C, whereupon a prominent endothermic event commences. Two-step decomposition is thereafter observed, with an accompanying loss of weight presumably due to oxygen loss. Powder XRD revealed the post DTA/TG products consist of a mixture of the binary oxides CoO and Cu$_2$O, the latter metal-rich oxide being consistent with the observed weight loss.
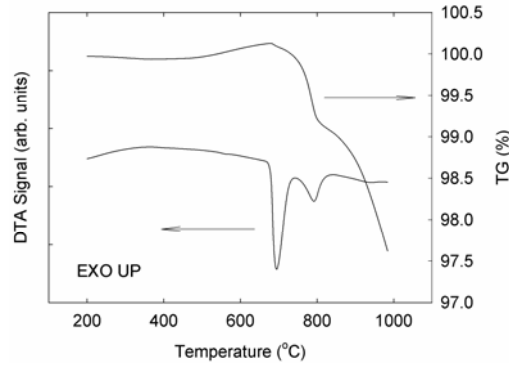
Fig. 69: DTA and TG curves for a CuCoO$_2$ specimen heated at 20 $^{\circ}$C/min under flowing N$_2$.

Consolidation of CuCoO$_2$ powders was accomplished at 600°C with an applied pressure of 45 MPa and resulted in a compact that was 72 % of the calculated density from XRD. Electrical resistivity measurements were performed on a parallelepiped specimen cut from the SPS consolidated compact and are shown in Figure 70. The data show an activated temperature dependence with $\rho(300$ K$) \sim 5$ Ohm-m. An Arrhenius plot (inset to Figure 70) and corresponding fit indicate a temperature dependence of $\rho(T) \sim \exp(E_a/k_BT)$, where k_B is Boltzmann's constant and E_a is an activation energy for conduction. From the fit, we obtain $E_a = 0.195$ eV, which is close to the value 0.2 eV previously reported [6] for conductivity measurements perpendicular to the c-axis on a small single crystal CuCoO$_2$ platelet. If the data in Figure 70 represent intrinsic conduction (and assuming temperature independent carrier mobility), this would imply a band gap $E_g = 2E_a = 0.39$ eV, quite close to the value 0.38 eV predicted [121] from DFT calculations.
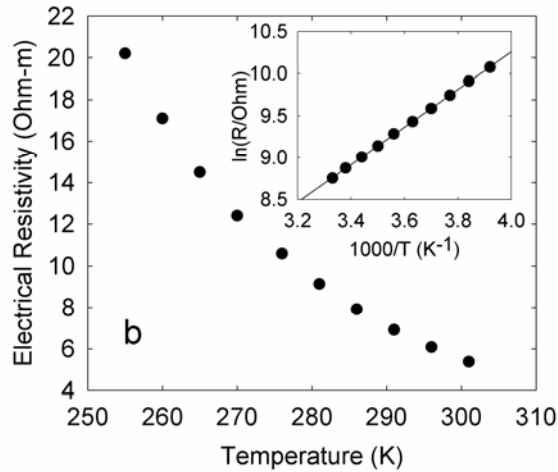
Fig. 70: Electrical resistivity data for CuCoO$_2$ indicating an activated temperature dependence. Inset: Arrhenius plot showing a fit to the data of the form $\rho(T) \sim \exp(E_a/k_BT)$.

Overview and Future Plans:

The research is going according to the scheduled tasks. The synthesis of different thermoelectric materials in nanocrystalline form has been optimized. Synthetic approaches have achieved nanocrystal formation in high yield allowing for nanocomposite processing and TE properties investigations. These results also include Bi and Bi-Sb compounds, of interest for TE refrigeration applications. Optimization employing the developed materials, in addition to an investigation of bulk oxide TE materials, is now underway. Theoretical investigations have corroborated our experimental data and provided impetus for future directions. A systematic investigation of the morphology and thermoelectric properties at elevated temperatures as well as Core-shell morphologies are underway.

Growth of nanoparticle coatings of $Ca_3Co_4O_9$ by a microwave plasma process for thermoelectric applications:

Layered cobaltates have been shown to have excellent thermoelectric properties and are promising candidate as a high temperature thermoelectric (TE) material. $Ca_3Co_4O_9$ has been grown in many forms including bulk, polycrystalline, and thin-film. Interfaces are expected to increase phonon scattering, so thin-films with good material properties could result in a higher ZT values. Furthermore, the additional incorporation of nanoparticles in a thin-film is expected to increase phonon scattering even further. In this study, we used a microwave plasma process to fabricate nanoparticle coating of $Ca_3Co_4O_9$. In previous work, we showed the growth of films with nanoparticles using a laser assisted spray pyrolysis technique (LASP) [126]. In this project the idea of generating nanoparticles from aerosols have been extended to a microwave plasma assisted process that enable the production of nanoparticles that require high temperature processing. Electrical conductivity and Seebeck measurements were performed to characterize the deposited films.

Introduction:

Advances in thermoelectric materials are essential for the developing the next generation of energy conversion devices. Devices in the future may provide localized cooling, or efficiently convert waste heat into electricity. TE materials made of cobaltates have been identified as promising materials for TE devices due to their bulk electronic material properties. Quality of TE materials is measured by the Seebeck coefficient, which related to performance of a TE device, given by ZT. Specifically, the Figure of merit is given as in equation 1:

$$ZT = S^2T/(\rho\kappa) \tag{1}$$

where S, T, ρ and κ are Seebeck coeff., temperature, electrical resistivity, and thermal conductivity, respectively. Bulk cobaltates have reported S as high as~130 µV/K [127]. Higher Seebeck values have been obtained by the incorporation of dopants such as Silver. High quality TE thin films that have the crystal structure of single crystals can have a low ρ and high S. It is well known that increased boundaries can lower thermal conductivity. Thin films and nanoparticles are expected to have a higher resistivity due to interfaces, and at the same time a lower thermal conductivity. This implies that exploiting these effects could result in maximizing

ZT, the Figure of merit. In this study we check the effect caused by reduced particle size on film morphology and electrical material properties.

Experiment:

Nanoparticle Film Growth:

A microwave assisted spray pyrolysis technique was used to grow nanograined films of $Ca_3Co_4O_9$. Typical spray pyrolysis consists of two steps. The first is the deposition of the elements of interest onto the substrate, and the evaporation of the solute. Then, a second step may be necessary to anneal the material to make it crystalline. In microwave-assisted spray pyrolysis, the microwave was used to heat the spray droplets. Heating causes the evaporation of the solvent, condensing the organic salts to a smaller particle. The particles will be partially or completely reacted before deposition on the substrate. In this microwave assisted spray process radiation transferred through a waveguide was coupled into a gas through a quartz flow tube as shown in Fig. 61. Oxygen was used as the carrier gas for the droplet transport. The microwave is resonantly absorbed by O_2 and water molecules, heating the gas and the droplets.

Initially, molar solutions were prepared by dissolving stoichiometric amounts of chlorides. This solution was transferred into a small cylinder containing an ultrasonic nebulizer. The nebulizer was operated at a frequency of 2.4 MHz to generate uniformly distributed droplets of a precursor with an average diameter of 1.5 microns. The aerosol was injected into the energy flow tube by flowing a carrier gas through a nozzle as seen in Fig. 71 and 72. The chamber was kept at a constant pressure near atmospheric, in order to maintain a constant spray.
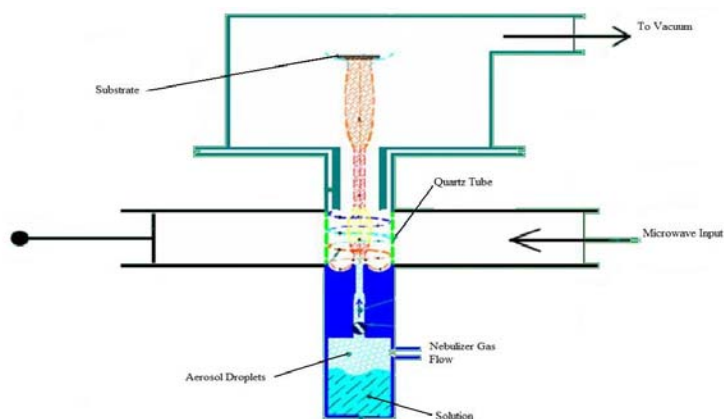
Fig. 71: Setup with nebulizer on bottom, waveguide in center, and substrate on top.
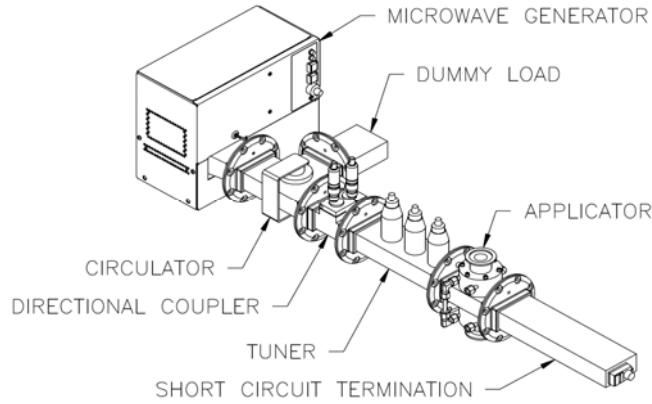
Fig. 72: Microwave guide of the experimental setup.

The created droplets pass through the microwave plasma into the deposition chamber. The aerosol droplets reduce in size and react due to the plasma and are finally deposited onto a heated substrate (~300-400°C). Note that this temperature is well below the >800°C melting point of $Ca_3Co_4O_9$. The temperature of the gas entering the deposition chamber was measured using a thermocouple. The temperature within the plasma region was determined by an optical emission spectroscopy technique. The morphology and crystallinity of as-grown films were investigated by SEM and XRD while electrical properties were investigated by a 4-point probe.

Films were deposited on quartz substrates by using this method and solute concentrations from 0.02M to 0.08M. This technique was used to create films containing many nanograined particles.

Results and discussion:

Spectral Temperature Calculations:

In order to determine the plasma temperature, mixtures of argon and oxygen were used as the carrier gas. From spectroscopic data the temperature can be determined because the excited atoms have populations N_{nm} described by the Boltzmann distribution when emission occurs due to electronic transitions.

$$N_{nm} = (n_n g_m / Z) * \exp - (E_m/kT) \tag{2}$$

where n_n = population of the lower state, g = statistical weight of the upper level transition, E_m = the energy of the upper level transition, k = Boltzmann constant, and Z = Partition function [128]. Intensity of the observed lines is described by:

$$I = A_{nm} N_{nm} hc/\lambda_{nm} = A_{nm} n_n g_m hc/ Z \lambda_{nm} * \exp - (E_m /kT) \tag{3}$$

where A = Einstein coeff. of spontaneous emission, h= Plank's constant, and c=speed of light. Taking the natural log of the above equation and using constants from the literature [129]

$$Ln (I\lambda_{nm}/g_m A_{nm}) = - (E_m)/kT \tag{4}$$

Therefore, a plot Ln (Iλ/gA) vs. the upper state energy gives a straight line of *slope = – 1/kT*.

Using this method, plots were made using spectroscopic data such as in Figure 73, taken in microwave plasma at various pressures, using Argon gas flow pushing a light water vapor.
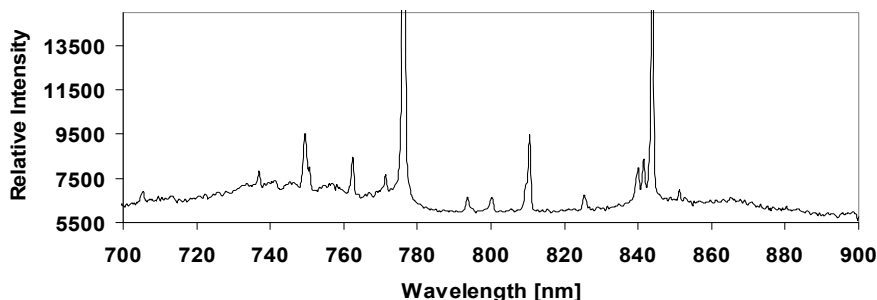
Fig. 73: Sample atomic spectra for plasma of an argon and oxygen gas mixture at 50 T. The two largest peaks are oxygen, and all others are argon.

Calculations using the data from 50 Torr and argon spectral lines gave a Temp = 3353 K, and using oxygen spectral lines gave a Temp = 3370 K. Both results are in close agreement, and well above the boiling temp of water, and the melting point of $Ca_3Co_4O_9$.

Film Morphology:

Top surface film images show very interesting formations of individual particles of fairly uniform sizes (Fig. 74). Note: this is a surface picture and crystals may form at different sizes in under the surface, where size can be estimated from XRD data.

The films created using a microwave plasma are much more uniform in the size distribution than those grown by the laser method. The nanoparticle nature of the films was additionally verified by AFM and XRD scans of nanoparticle films as seen in Figure 75.

| A | B | C | D |
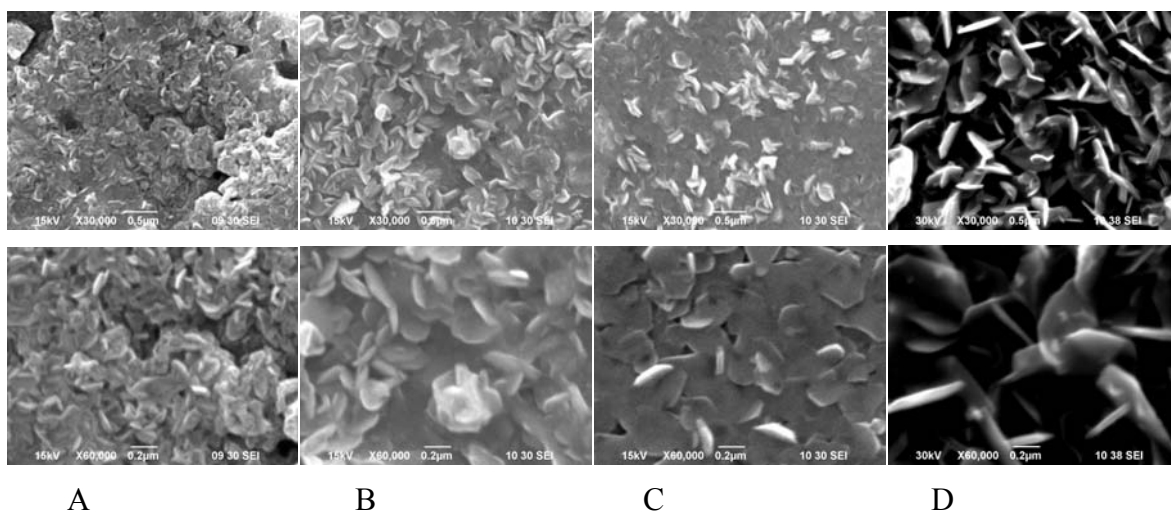
Fig. 74: SEM's of prepared films varying in surface size from between 100nm to 500nm. Scan magnification is 30kX (top), and 60kX (bottom).

Signature peaks of $Ca_3Co_4O_9$ in crystalline phase are shown. The average particle size of two thin films was calculated from data due to peak broadening caused by the small crystals. The diameter of the crystals was calculated using data from the [200] peak and the full width half maximum (FWHM). The diameter of the particles is given by the Debye–Scherrer formula [130, 131]:
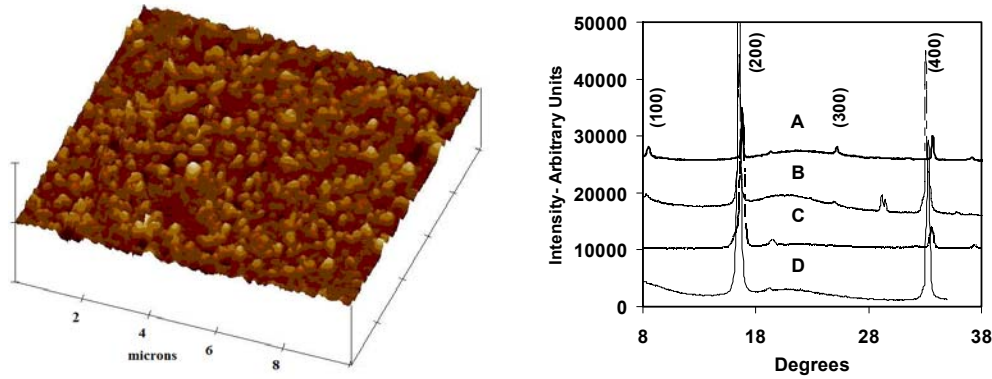
Fig. 75: (a) AFM 10 µm scan of film C.   (b) XRD of films A – D respectively.

$D= 0.9\lambda/b *\cos\theta$

where λ is the wavelength of X-ray, b = FWHM in radians, and θ is diffraction angle. From XRD data and eqn. 4, crystal sizes of films B,C,and D are estimated as 70.8 [nm], 41.2 [nm] and 22.1 [nm], respectively.

Resistance measurements exhibit the effect of the smaller particle size as evident from the onset of semiconducting behavior at a higher temperature as seen in Fig. 76.
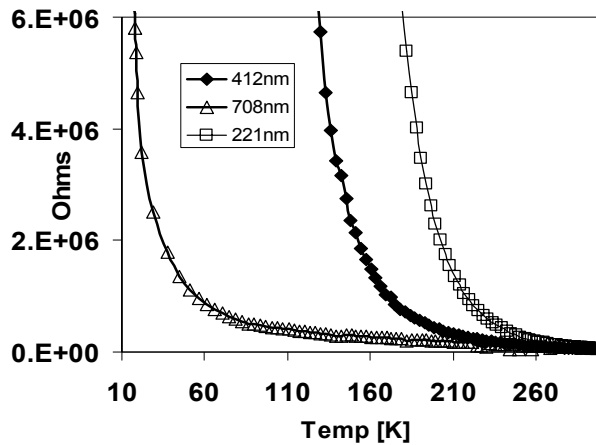
Fig. 76: Normalized resistance measurements on films containing different sized particles.
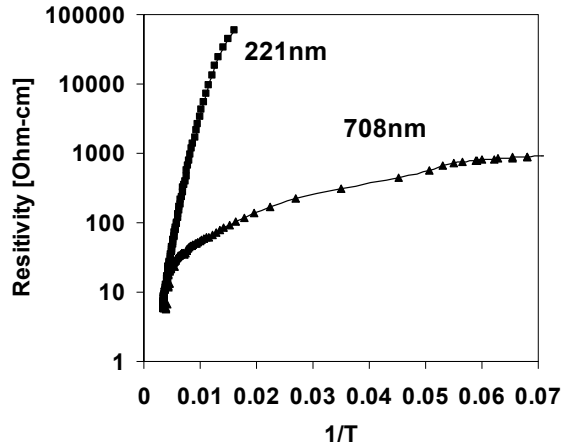
Fig. 77: Resistivity for films with particle sizes 221nm to 708nm.

The film with the smallest particles shows what appears to be a different type of activated conduction mechanism than that of the largest particles as seen from the graph of ρ vs. 1/T shown in Figure 77. The large particles exhibit the primarily thermally activated conduction typically seen in bulk materials. The smaller particle film shows a deviation from the larger particles just below room temperature, and the resistivity quickly increases exponentially. This suggests that the smaller particle film exhibits an additional conduction mechanism, such as carrier hopping. This effect is attributed to the larger number of interfaces and defects due to the smaller particle size.

Seebeck Measurements:

A system capable of measuring the Seebeck coefficient in the region near room temperature was constructed. The apparatus clamps the substrate to heater blocks at opposite ends of substrate by silver paint that is heated up and allowed to dry. The temperature is monitored by using thermocouples in 4 locations, two in the middle, on top of the film; and two on the outside attached to the heaters. As with the substrate, the thermocouples are attached with silver paint. Care is taken to minimize the size of the silver dots so that any contribution to Seebeck measurements is minimal. The type of thermocouple is T-type, which has a negligible contribution to the measurement. The size of the thermocouple is 0.005 inches, chosen again to minimize any measurement contributions.

Our system is limited to the regions near room temperature, due to contributions from radiation which will take place at higher temperatures. In addition to the atmospheric radiation, the thermocouples are fragile, and will break down at higher temperatures. It is desired to get high temperature Seebeck measurements of our material due to it prospective use at high temperatures. For this, we will have to seek out possible systems with high temperature capability that may exist already at other institutions.

Measurements are done by heating one side of the substrate, allowing temperature to reach a steady state, and measuring the values of voltage and temperatures at steady state.

A typical Seebeck measurement on one of the $Ca_3Co_4O_9$ films is shown in Figure 78. The value of the slope shows the Seebeck value as 158 µV/K , which is near or slightly better than typical values (~130 µV/K) given for bulk material [Fig.78].
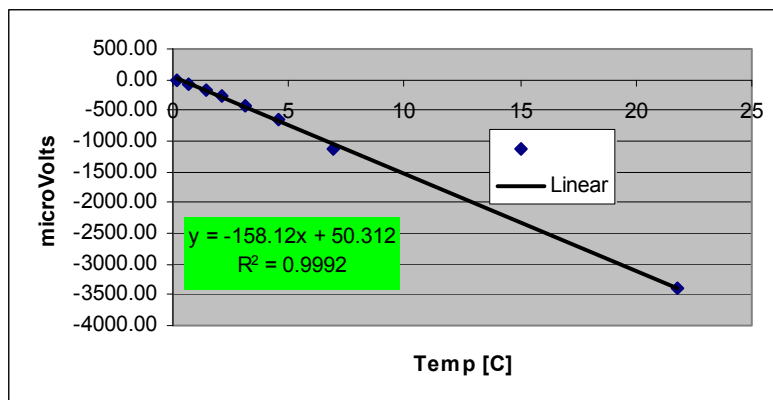
Fig. 78: Sample Seebeck measurement on a film grown with the microwave system.

Conclusion:

The growth of $Ca_3Co_4O_9$ nanocrystalline thin films using a microwave assisted spray technique has been demonstrated. Thin films containing nanocrystals of different sizes were grown and the dominant mechanism of current transport was shown to carrier hopping. Seebeck measurements showed the coefficients to be in the same range as bulk material.

III. Reportable Outcomes

Publications and presentations based on support through grant USAMRMC W81XWH-07-1-0708 *(CIFM-supported researchers are shown in bold, with students and postdocs italicized)*:

Book / Book Chapter (Submitted):
1. "The Bottom-Up Approach To Bulk Thermoelectric Materials With Nano-Scale Domains" *Anuja Datta, Adrian Popescu*, **Lilia Woods** and **George S. Nolas** , CRC Handbook on Thermoelectrics and Its Energy Harvesting, Taylor & Francis (submitted).
2. *Edited Volume:* Proceedings of the 2009 Materials Research Society Volume 1166, *Materials and Devices for Thermal-to-Electrical Energy Conversion*, Editors: J. Yang, **G.S. Nolas**, K. Koumoto and Y. Grin.

Journal Publications (Published/Submitted):

1. "Structural and magnetic characterization of agglomeration-free superparamagnetic polymer nanocomposites and their microwave properties" –*K. Stojak, S. Pal*, C. Morales, J. Dewdney, T. Weller, J. Wang and **H. Srikanth**, Advanced Functional Materials (submitted 2010)
2. "Phase coexistence and magnetic anisotropy in polycrystalline and nanocrystalline $LaMnO_3$" –*S. Chandra, A. Figueroa*, B. Ghosh, *M. H. Phan*, **H. Srikanth** and A. K. Raychaudhuri, Journal of Applied Physics (submitted 2010)
3. "Giant magnetoimpedance and field sensitivity in amorphous and nanocrystalline $(Co_{1-x}Fe_x)_{89}Zr_7B_4$ (x =0, 0.025, 0.05, 0.1) ribbons" –*A. Chaturvedi, N. Laurita*, A. Leary, *M. H. Phan*, M. E. McHenry and **H. Srikanth**, Journal of Applied Physics (submitted 2010)
4. "Enhanced GMI effect and field sensitivity in Co-coated soft ferromagnetic amorphous ribbons" –*N. Laurita, A. Chaturvedi*, C. Bauer, P. Jayathilaka, A. Leary, C. Miller, *M. H. Phan*, M. E. McHenry and **H. Srikanth**, Journal of Applied Physics (submitted 2010)
5. "Magnetic switching and magnetic transitions in $ErCo_2$ probed by radio frequency transverse susceptibility" –A. I. Figueroa, *S. Chandra, M. H. Phan*, **H. Srikanth**, C. M. Bonilla, L. M. Garcia, F. Bartolome, J. Bartolome and J. Herrero-Albillos, Journal of Applied Physics (submitted 2010)
6. "Magnetically tunable nanocomposites for microwave applications" –C. Morales, J. Dewdney, *S. Pal, K. Stojak*, **H. Srikanth**, J. Wang and T. Weller, IEEE Transactions of Microwave theory and techniques (accepted, 2010)
7. "Role of epitaxy in controlling the magnetic and magnetostrictive properties of cobalt ferrite – PZT bilayers" –*D. Mukherjee, T. Dhakal, R. Hyde*, **P. Mukherjee**, **H. Srikanth** and **S. Witanachchi**, Journal of Physics D: Applied Physics (accepted, 2010)
8. "Dual-laser deposition of epitaxial $PbZr_{0.52}Ti_{0.48}O_3$ ferroelectric thin films on $La0.7Sr_{0.3}MnO_3$ electrodes" –*D. Mukherjee, R. Hyde, T. Dhakal*, **H. Srikanth**, **P. Mukherjee** and **S. Witanachchi**, Journal of Applied Physics (under review, 2010)
9. "Correlation between magnetic softness, sample surface and magneto-impedance in $Co_{69}Fe_{4.5}X_{1.5}Si_{10}B_{15}$ (X = Ni, Al, Cr) amorphous ribbons" –*A. Chaturvedi, T. Dhakal*, **S. Witanachchi**, A. –T. Le, *M. H. Phan* and **H. Srikanth**, Physica B 405, 2836 (2010)
10. "Evidence for carrier-mediated magnetism in Mn-doped ZnO films" –*D. Mukherjee, T. Dhakal*, **H. Srikanth**, **P. Mukherjee** and **S. Witanachchi**, Physical Review B 81, 205202 (2010)

11. "Enhancement of the giant magnetoimpedance effect and its magnetic response in ion-irradiated amorphous ribbons" –A. T. Le, N. Q. Hoa, D. G. Park, *M. H. Phan*, **H. Srikanth** and S. C. Yu, Materials Science and Engineering B 166, 89 (2010)

12. "Field dependence of the magnetocaloric effect in core-shell nanoparticles" –V. Franco, A. Conde, D. Sidhaye, B. L. V. Prasad, P. Poddar, S. Srinath, *M. H. Phan* and **H. Srikanth**, Journal of Applied Physics 107, 09A910 (2010)

13. "Magnetic anisotropy and field switching in cobalt ferrite thin films deposited by pulsed laser ablation" –*T. Dhakal, D. Mukherjee*, **P. Mukherjee**, *M. H. Phan*, **H. Srikanth** and **S. Witanachchi**, Journal of Applied Physics 107, 053914 (2010)

14. "Critical length and giant magnetoimpedance in Co-Fe-Ni-Si-B amorphous ribbons" –*A. Chaturvedi, T. P. Dhakal*, **S. Witanachchi**, A. –T. Le, *M. –H. Phan* and **H. Srikan th**, Materials Science and Engineering B (in press, 2010)

15. "Carbon Nanostraws: Nanotubes filled with superparamagnetic particles" –*S. Pal, S. Chandra, M. H. Phan*, **P. Mukherjee** and **H. Srikanth**, Nanotechnology 20, 485604 (2009)

16. "Chemical synthesis and magnetic properties of cubic CoO nanocrystals and 3D nanostructures" –V. Alexandrakis, G. Basina, D. Niarchos, G. Hadjipanayis, *S. Pal*, **H. Srikanth**, I. Panagiotopoulos, V. Tzitzios, Crystal Growth and Design 9, 3353 (2009).

17. *Khadka, D.* and **Haynie, D.T.** (2010) Insoluble synthetic polypeptide mats from aqueous solution by electrospinning, *ACS Appl. Mater. Interf.*, DOI: 10.1021/am1006657

18. "Facile Chemical Synthesis of Nanocrystalline Thermoelectric Alloys Based on Bi-Sb-Te-Se" *Anuja Datta, Jagannath Paul*, Arik Kar, Amitava Patra, Zhengliang Sun, Lidong Chen, *Joshua Martin,* and **George S. Nolas**, *Crystal Growth and Design*, 10, 3983, 2010.

Conference Presentations (contributed) [2009-10]:

1. "Magnetocaloric effect and refrigeration capacity in $Eu_8Ga_{16}Ge_{30}$ – EuO composites" –*A. Chaturvedi, S. Stefanoski, M. H. Phan,* **G. Nolas** and **H. Srikanth**, 54th annual Magnetism and Magnetic Materials (MMM) conference, Nov. 14-18, 2010, Atlanta GA

2. "Phase coexistence and magnetic anisotropy in polycrystalline and nanocrystalline $LaMnO_{3+d}$" –*S. Chandra, A. Figueroa, M. H. Phan*, **H. Srikanth**, B. Ghosh and A. K. Raychaudhuri, 54th annual Magnetism and Magnetic Materials (MMM) conference, Nov. 14-18, 2010, Atlanta GA

3. "Giant magnetoimpedance and field sensitivity in amorphous and nanocomposite $(Co_{1-x}Fe_x)_{89}Zr_7B_4$ ribbons" –*A. Chaturvedi*, A. Leary, N. Laurita, *M. H. Phan*, M. E. McHenry and **H. Srikanth**, 54th annual Magnetism and Magnetic Materials (MMM) conference, Nov. 14-18, 2010, Atlanta GA

4. "Magnetic polymer composites with tunable microwave properties" –*K. Stojak, S.Pal*, **H. Srikanth**, S. Skidmore, C. Morales, J. Dewdney, J. Wang and T. Weller, APS March meeting, Portland OR (March 15 – 19, 2010)

5. "Probing magnetic anisotropy and exchange bias in coupled Au-Fe_3O_4 nanoclusters" –*S. Chandra, N. A. Frey, M. H. Phan*, **H. Srikanth**, C. Wang and S. Sun, APS March meeting, Portland OR (March 15 – 19, 2010)

6. "Fabrication and magnetic properties of CNT filled with Fe_3O_4 nanoparticles" –*S. Pal, K. Stojak, S. Chandra, M. H. Phan*, **P. Mukherjee** and **H. Srikan th**; APS March meeting, Portland OR (March 15 – 19, 2010)

7. "Ferromagnetism and large MCE in EuGaGe clathrates" –*M. H. Phan, A. Chaturvedi, S. Stefanoski, H. Kirby,* **G. S. Nolas** and **H. Srikan th**; APS March meeting, Portland OR (March 15 – 19, 2010)

8. "Optimization of GMI in amorphous CoFeZrB ribbons" –*A. Chaturvedi, M. H. Phan*, **H. Srikanth**, A. Leary and M. McHenry; APS March meeting, Portland OR (March 15 – 19, 2010)

9. "High-aspect ratio magnetic nanotubes" – *S. Pal, K. Stojak, S. Chandra, M. H. Phan*, **P. Mukherjee** and **H. Srikanth**, 11th joint MMM-INTERMAG conference, Washington DC (Jan 18-22, 2010)

10. *Jason Rejman, Dino Ferizovic,* Martin Munoz, **Pritish Mukherjee** and **Sarath Witanachchi**, "Composites of PbSe quantum dots and vertically aligned TiO_2 nanorods for next generation solar cells", 18th Annual International Conference on Composites & Nano Engineering, Anchorage, Alaska, July 4-10, 2010.

11. *Devajyoti Mukherjee, Robert Hyde, Tara Dhakal*, **Hariharan Srikanth**, **Pritish Mukherjee** and **Sarath Witanachc hi**, "Dual-laser deposition of stoichiometric $PZT/CoFe_2O_4$ epitaxial heterostructures" The Materials Research Society Spring Meeting, San Francisco, CA, April 2010.

12. **Sarath Witanachchi**, *Ted Wangensteen, Marek Merlak*, and **Pritish Muk herjee**, "Nanoparticle coatings of $Ca_3Co_4O_9$ with high power factors fabricated by a microwave plasma process", International Conference on Themoelectrics, Shanghai, China, May 2010.

13. *Khadka, D., Bhattarai, K.* and **Haynie, D.T.** (2010) Electrospinning of synthetic polypeptide nanofibers, NanoFlorida 2010, Orlando, 24th September

14. **L.M. Woods**, *A. Popescu, J. Martin*, and **G.S. Nolas**, 'Transport Properties of Thermoelectric Nanocomposites', *Proc. Mater. Rec. Soc.* 1166, 121 (2009).

15. *H. Kirby, J. Martin, A. Datta,* L. Chen, **G.S. Nolas**, 'Enhanced thermoelectric properties in PbTe nanocomposites', *Proc. Mater. Rec. Soc.*1166, 71 (2009).

16. *A. Datta, J. Paul, A. Popescu*, **L. Woods, G.S. Nolas**, "Synthesis and Transport properties of Dimensional Nanocomposite Chalcogenides"**,** Oral Presentation at *The American Physical Society Annual Meeting*, March 15-19, 2010, Portland, Oregon.

17. *A. Datta, J. Paul* and **G.S. Nolas**, "Solution Phase Synthesis Routes In Preparing Chalcogenide Nanocomposites With Enhanced Thermoelectric Properties" Oral Presentation at *The 86th American Chemical Society Florida Annual Meeting and Exposition*, May 13-15, 2010.

18. *H. Kirby, J. Martin,* L. Chen, **G.S. Nolas**, "Synthesis and Characterization of Doped and Undoped PbTe Nanocomposites" Oral Presentation at *The 86th American Chemical Society Florida Annual Meeting and Exposition*, May 13-15, 2010.

Invited talks:

Hari Srikanth gave the following invited talks:

1. **Invited Speaker**, Conference on Strongly Correlated Materials (iConQuest 2010), New Delhi, INDIA (December 20-23, 2010)

2. **Seminar,** Northwestern University, Department of Physics, Evanston, IL (Oct. 14, 2010)
3. **Invited Speaker**, Symposium on Magnetic and Transport Properties of Oxides, CIMTEC 2010, Montecatini Terme, ITALY (June 6-11, 2010)
4. **Seminar,** "Functional magnetic nanostructures", CNR-ISMN, Bologna, ITALY (June 11, 2010)
5. **Seminar,** "Functional magnetic nanostructures", University of Uppsala, Uppsala, SWEDEN (June 4, 2010)
6. **Seminar,** "Functional magnetic nanostructures", KTH –Royal Institute of Technology, Stockholm, SWEDEN (June 3, 2010)
7. **Seminar,** "Functional magnetic nanostructures", IFW-Dresden, Dresden, GERMANY (May 31, 2010)
8. **Invited Speaker**, Focus Topic on "Bulk properties of oxides", APS March Meeting, Portland, OR (March 15-19, 2010); Title "Magnetism in complex oxides probed by transverse susceptibility and magnetocaloric effect"
9. **Condensed Matter Seminar,** Department of Physics, University of Florida, Gainesville FL (November 16 2009)
10. **Colloquium,** Advanced Materials Research Institute, University of New Orleans, October 6, 2009.

George Nolas gave the following invited talks:

11. "Enhanced Power Factor in Nanocomposite Chalcogenides", **G.S. Nolas**, 2009 Department of Energy Thermoelectric Applications Workshop, October 1, 2009, San Diego, California.
12. "Thermoelectric Nanocomposite Chalcogenides" **G.S. Nolas**, 451st WE-Heraeus-Seminar: Nanostructured Thermoelectric Materials, February 23, 2010, Bad Honnef, Germany.
13. "Bottom-up Approach for Enhanced Thermoelectric Properties in Materials with Nano-scale Domains", **G.S. Nolas**, Colloquium at the Department of Physics, Central Michigan University, September 2nd, 2010, Mount Pleasant, Michigan.

Donald Haynie gave the following invited talk:

14. **Haynie, D. T.,** (2010) Polypeptide multilayer nanofilms, Nano-bio Collaborative 2010 Conference, USF, 11th March, invited talk.

Other noteworthy professional activities by CIFM researchers:

Hari Srikanth was:
- An Invited Speaker, "Functional Magnetic Nanostructures" –Evening with a Scholar lecture to the Tampa Bay community leaders/entrepreneurs, November 6, 2009
- **Publication Chair and Steering Committee Member**, 2011 MMM Conference, Scottsdale, AZ (November 2011)
- **Session Chair**, Session AT: Magnetocaloric Materials I, joint MMM/INTERMAG conference, January 2010, Washington DC
- **Co-organizer, MRS 2010 Spring Meeting Symposium N** "Functional oxide nanostructures and heterostructures", April 2010, San Francisco, CA

- **Publications Editor, 11th** Joint INTERMAG/MMM conference, Washington DC, January 2010
- **Scientific Committee Member**, Symposium E: Magnetic materials at the nanoscale, 11th International Conference on Advanced Materials (ICAM 2009), Rio de Janeiro, Brazil (Sept 2009)

IV. Conclusion

Update on Milestones:

- Studies of magnetic and hydrodynamic properties of bio-functionalized ferofluids under flow conditions.
  Magnetic properties of bio-functionalized ferrofluids have been completed and were presented in the last annual report. The hydrodynamic properties will be investigated in Year 4.

- Chemical synthesis of ferrite nanoparticles and fabrication of polymer nanocomposite films, analysis of structural, electrical and magnetic properties.
  Completed and results are presented in this report.

- PLD growth of ferroelectric/ferrite heterostructures with controlled interface strain, and high frequency measurements.
  Completed and results presented in this report.

- Fabrication and characterization of vanadium doped ZnO (ZnO:V) and manganese doped ZnO (ZnO:Mn) epitaxial heterostructures. Investigate the multiferroic coupling in these structures.
  Completed and results presented in this report. This sub-task in Project 5 has been completed three years ahead of schedule.

- Integration of nanoparticles (PbSe quantum dots) with polymer and characterization for optical properties:
  Completed in June 2009 and reported in last annual report.

- Structural and calorimetric analysis for thermal stability tests.
  Completed and results presented in this report.

- Comparative studies and analysis: Synthesis bulk materials for comparison to the nano-scale TE materials.
  Completed and reported in last annual report.

- Theoretical modeling of conductance and thermopower of core-shell nanocomposites.
  Completed and results presented in this report.

The experimental research conducted to achieve the following milestones has been refined to pursue other, more promising areas as indicated below:
- Growth of nano-wires of inorganic compounds with variable diameters
- Formation of polymer nano-templates.
- Manipulation of molecules using electrical stimulation.

- Molecular dynamics simulations of structural and mechanical properties of oxide nanostructures and density functional theory studies of electronic properties of nano-wires and nano-ribbons.
- Design and fabrication of substrates with controlled nanotopography.

Previous work on these milestones has reported on experiments in cell adhesion and viscoelasticity. Experiments investigating the combined effects of physical and biochemical stimuli on cell adhesion and organization are more important for developing biosensors than the insight gained from the previous work. Results pertaining to the control of substrate charge, viscoelasticity, and functionalization via polypeptide multilayer films are presented in this annual report, with the work to continue in the fourth year of the project. This also reflects the departure of Dr. Chun-Min Lo from USF and the addition of Dr. Donald Haynie to the research faculty associated with CIFM.

- Biosensor fabrication using carbon nanotube arrays and evaluating the potential to sense different analytes adsorbed to the surface.
- Theoretical modeling and simulation of toxic absorption, external fields and mechanics on carbon nanotubes.

The above experiments have been redesigned based on recent discoveries in graphene-based sensors which may have several advantages over carbon nanotube-based sensors. Preliminary work related to graphene as a sensor is presented in this annual report. Work on this and carbon nanotube-based sensors will continue in the fourth year of the project.

Project Milestones for Continuation Proposal:

We have received funding for continuation of this project for another three-year period till 9/19/2013. The following tables identify the milestones and timeline for each of the seven projects in the continuing proposal. The additional work is italicized and the revised timelines (for each project) are indicated. Green bars indicate accomplished work while the purple bars indicate work from the third year that is being continued onto Year 4. We expect to accomplish completion of the purple bars in Year 4. This rearrangement is based on the considerations described in the update on third-year milestones:

Task I: Nanostructured materials for biomedical diagnostics and chemical sensing

Project 1: Functional magnetic fluids for biomedical applications.

RESEARCH TASKS	Year 1	Year 2	Year 3	Year 4	Year 5	Year 6
Chemical synthesis of magnetic nanoparticles and ferrofluids, Structural analysis, DC and AC magnetization studies	███					
Functionalization of ferrofluids with biocompatible surfactant coatings of the nanoparticles. Chemical and Physical properties characterization of the functionalized ferrofluids	███	███				

RESEARCH TASKS	Year 1	Year 2	Year 3	Year 4	Year 5	Year 6
Studies of magnetic and hydrodynamic properties of bio-functionalized ferrofluids under flow conditions		green	magenta			
Synthesis of PEG, Dextran coated nanoparticles and clusters for hyperthermia experiments and their structural and magnetic characterization				gray	gray	
Measurements and comparative analysis of specific absorption rates and AC power losses of ferrofluids for magnetic hyperthermia applications				gray	gray	gray
Bifunctional metal-oxide coupled and core-shell nanostructures				gray	gray	gray

Project 2: Nanoparticle/nano-wire structures and polymer nanoparticles for sensing and molecular manipulation

RESEARCH TASKS	Year 1	Year 2	Year 3	Year 4	Year 5	Year 6
Synthesis and characterization of Au templates with variable spacing and formation of In nano-pore structures	green					
Growth of nano-wires of inorganic compounds with variable diameters.	green	green	green			
Formation of polymer nano-templates		green	magenta			
Manipulation of molecules using electrical stimulation			magenta			
Molecular dynamics simulations of structural and mechanical properties of oxide nanostructures and density functional theory studies of electronic properties of nano-wires and nano-ribbons		green	green/magenta			
Development and testing of amorphous magnetic ribbons for MI-based sensing			green	gray	gray	
Improving the field sensitivity and figure of merit of giant magnetoimpedance (GMI) materials				green	gray	gray

Project 3: Carbon-nanotube based sensors

RESEARCH TASKS	Year 1	Year 2	Year 3	Year 4	Year 5	Year 6
CVD and cluster deposition of carbon nanotube networks	green					
Structural, electrical, and capacitive measurements on nanotube networks	green	green				
Biosensor fabrication using carbon nanotube arrays and evaluating the potential to sense different analytes adsorbed to the surface		green	magenta			
Theoretical modeling and simulation of toxic absorption, external fields and mechanics on carbon nanotubes		green	magenta			

RESEARCH TASKS	Year 1	Year 2	Year 3	Year 4	Year 5	Year 6
Magnetoimpedance measurements and sensing of biomolecules				gray	gray	gray
Integrated ferroelectric-ferromagnetic high-aspect ratio nanostructures				gray	gray	gray

Project 4: Functional materials for affecting cell proliferation and locomotion

RESEARCH TASKS	Year 1	Year 2	Year 3	Year 4	Year 5	Year 6
Magnetic nanoparticle attachment to cell membranes	green					
Design and fabrication of lithographically pattered metallic micro wires	green	green				
Design and fabrication of substrates with controlled nanotopography		green	magenta			
Study of cell migration, cell-substrate adhesion, and cell growth	green	green	magenta			
Stimuli-response studies using ECIS of magnetic nanoparticle loaded cells		green	green	gray	gray	
An integrated functional materials approach to the development of an artificial Matrigel				gray	gray	gray
Formation and delivery of functionalized artificial platelets for rapid cessation of internal bleeding				gray	gray	gray

Task II: Multifunctional composites for communication and energy applications

Project 5: Tunable multifunctional nano- and heterostructures for RF and microwave applications

RESEARCH TASKS	Year 1	Year 2	Year 3	Year 4	Year 5	Year 6
Chemical synthesis of ferrite nanoparticles and fabrication of polymer nanocomposite films, analysis of structural, electrical and magnetic properties	green	green	green			
PLD growth of ferroelectric/ferrite heterostructures with controlled interface strain, RF and microwave measurements of polymer composites and oxide films	green	green	green			
Materials growth efforts continued with piezoelectric films containing nanoparticle inclusions, experiments to study the magneto-electric and multiferroic coupled response in materials and prototype device structures				gray	gray	gray
Fabricate and characterize ZnO:V, ZnO:Mn and ZnO:V/ZnO:Mn heterostructures. Investigate the multiferroic coupling in these structures				green	green	green

Synthesis of ferroelectric-ferromagnetic nanopillar-nanoparticle structure and exploration of magnetoelectric coupling.			▒	▒	▒

Project 6: Flexible photonic materials for solar-based energy sources

RESEARCH TASKS	Year 1	Year 2	Year 3	Year 4	Year 5
Synthesis and characterization of PbSe and PbS_xSe_{1-x} nanoparticles by microwave plasma	█	█			
Integration of nanoparticles with polymer and characterization of optical properties	█	█	▒	▒	
Formation of single cell device structures with nanoparticles of different sizes and characterization of the output			█	▒	
Fabrication and evaluation of tandem structures			▒	▒	▒
Synthesis and characterization of InSb nanoparticles			▒	▒	▒
Fabricate InSb-polymer hybrid solar cell structures and compare the performance with PbSe based devices				▒	▒

Task III: Solid-state materials for power generation and refrigeration

Project 7: High-performance bulk and nanocomposite thermoelectric materials for power generation

RESEARCH TASKS	Year 1	Year 2	Year 3	Year 4	Year 5	Year 6
Bulk nanocomposites: optimize synthesis parameters	█	█				
Core-shell approach towards optimization		█	█			
Structural and calorimetric analysis for thermal stability tests		█	█			
Measurement of TE properties		█	█	▒	▒	
Comparative studies and analysis: Synthesis bulk materials for comparison to the nano-scale TE materials		█	█			
Optimization employing the developed materials			█	▒	▒	
Device design development					▒	▒
Measurement, optimization and re-development of prototype TE devices					▒	▒
Theoretical modeling of conductance and thermopower of core-shell nanocomposites		█	█			
Fabrication of CaCoO nanoparticle coatings by a microwave plasma process and investigation of thermoelectric properties			▒	▒	▒	▒
Synthesis of bulk thermoelectrics			█	▒	▒	

Relevance of the Research:

From the perspective of military applications specific to the US Army Medical Research and the DoD in general, we have identified three key targeted applications where timely advances are critically needed. The concerted effort in this Integrated Functional Materials Project and our ongoing development of an interdisciplinary Center for Integrated Functional Materials (CIFM) at USF will advance the science knowledge base in these areas. The three targeted tasks broadly encompass issues of most importance to the soldier in the battlefield. At the culmination of the projects specific advances are expected in new materials and functionalities that aid in diagnostics and communication of medical problems encountered by the soldier in the field, sensors with improved sensitivity and specificity to detect threats such as trace biological agents, and the need for novel portable and renewable energy and power sources to power these new devices.

Once established, CIFM will continue to be a national resource in the development of new materials and devices for the military and commercial sector, and a stimulant of industry in the United States based on emerging technologies and manufacturing processes. The specific outcome of the research activities is therefore expected to lead to new devices/systems/composite materials useful for the USAMRMC.

V. Bibliography

1. S. Sun, H. Zeng *J. Am, Chem. Soc*. 2002, 124, 8204.
2. M. Liu, X. Li, J.Lou, S. Zheng, K.Du, N. X. Sun. *J. Appl. Phys.* 2007, 102, 083911.
3. J. Xie, C. J. Xu, Z. C. Xu, Y. L. Hou, K. L. Young, S. X. Wang, N. Pourmand, S. H. Sun, *Chem. Mater.* **2006**, *18*, 5401.
4. Sun S and Zeng H (2002), J. Am. Chem. Soc. 124 8204-5.
5. P. R. Wallace (1947). *Physical Review* **71**: 622.
6. C. Lee *et al.* (2008). *Science* **321**: 385.
7. Nair, R. R.; Blake, P.; Grigorenko, A. N.; Novoselov, K. S.; Booth, T. J.; Stauber, T.; Peres, N. M. R.; Geim, A. K. (2008). Science **320**: 1308.
8. Qingkai *et al.* (2008). *Applied Physics Letters* **93**, 113103
9. Gelehrter, T.D. and R. Sznycer-Laszuk, Thrombin induction of plasminogen activator-inhibitor in cultured human endothelial cells. J Clin Invest, 1986. 77(1): p. 165-169.
10. Moore, K.L., et al., Endotoxin enhances tissue factor and suppresses thrombomodulin expression of human vascular endothelium in vitro. J Clin Invest, 1987. 79(1): p. 124-130.
11. Weiss, T., et al., Serial subculture and relative transport of human endothelial cells in serum-free, defined conditions. In Vitro Cellular & Developmental Biology - Plant, 1990. 26(8): p. 759-768.
12. Maciag, T., et al., Organizational behavior of human umbilical vein endothelial cells. J Cell Biol, 1982. 94(3): p. 511-520.
13. Kubota, Y., et al., Role of laminin and basement membrane in the morphological differentiation of human endothelial cells into capillary-like structures. J Cell Biol, 1988. 107(4): p. 1589-1598.
14. Grant, D.S., et al., Two different laminin domains mediate the differentiation of human endothelial cells into capillary-like structures in vitro. Cell, 1989. 58(5): p. 933-943.
15. Folkman, J., Angiogenesis in cancer, vascular, rheumatoid and other disease. Nat Med, 1995. 1(1): p. 27-31.
16. Bergers, G. and L.E. Benjamin, Tumorigenesis and the angiogenic switch. Nat Rev Cancer, 2003. 3(6): p. 401-410.
17. Yonemura, S., et al., Cell-to-cell adherens junction formation and actin filament organization: similarities and differences between non-polarized fibroblasts and polarized epithelial cells. J Cell Sci, 1995. 108 (Pt 1): p. 127-142.
18. Pelham, R.J., Jr. and Y. Wang, Cell locomotion and focal adhesions are regulated by substrate flexibility. Proc Natl Acad Sci U S A, 1997. 94(25): p. 13661-13665.
19. Discher, D.E., P. Janmey, and Y.L. Wang, Tissue cells feel and respond to the stiffness of their substrate. Science, 2005. 310(5751): p. 1139-1143.
20. Georges, P.C. and P.A. Janmey, Cell type-specific response to growth on soft materials. J Appl Physiol, 2005. 98(4): p. 1547-1553.

21. Califano, J.P. and C.A. Reinhart-King, Substrate Stiffness and Cell Area Predict Cellular Traction Stresses in Single Cells and Cells in Contact. Cellular and Molecular Bioengineering, 2010. 3(1): p. 68-75.

22. Picart, C., Polyelectrolyte multilayer films: from physico-chemical properties to the control of cellular processes. Curr Med Chem, 2008. 15(7): p. 685-697.

23. Richert, L., et al., Improvement of stability and cell adhesion properties of polyelectrolyte multilayer films by chemical cross-linking. Biomacromolecules, 2004. 5(2): p. 284-294.

24. Richert, L., et al., Elasticity of native and cross-linked polyelectrolyte multilayer films. Biomacromolecules, 2004. 5(5): p. 1908-1916.

25. Schneider, A., et al., Elasticity, biodegradability and cell adhesive properties of chitosan/hyaluronan multilayer films. Biomed Mater, 2007. 2(1): p. S45-S51.

26. Lavalle, P., et al., Comparison of the Structure of Polyelectrolyte Multilayer Films Exhibiting a Linear and an Exponential Growth Regime: An in Situ Atomic Force Microscopy Study. Macromolecules, 2002. 35(11): p. 4458-4465.

27. Picart, C., et al., Molecular basis for the explanation of the exponential growth of polyelectrolyte multilayers. Proc Natl Acad Sci U S A, 2002. 99(20): p. 12531-12535.

28. Lavalle, P., et al., Modeling the Buildup of Polyelectrolyte Multilayer Films Having Exponential Growth ✗. The Journal of Physical Chemistry B, 2003. 108(2): p. 635-648.

29. Haynie, D.T., et al., Quantal self-assembly of polymer layers in polypeptide multilayer nanofilms. Biomacromolecules, 2006. 7(8): p. 2264-2268.

30. Zhang, L., et al., Context dependence of the assembly, structure, and stability of polypeptide multilayer nanofilms. ACS Nano, 2007. 1(5): p. 476-486.

31. Vautier, D., et al., Polyelectrolyte multilayer films modulate cytoskeletal organization in chondrosarcoma cells. J Biomater Sci Polym Ed, 2002. 13(6): p. 713-732.

32. Boura, C., et al., Endothelial cells grown on thin polyelectrolyte mutlilayered films: an evaluation of a new versatile surface modification. Biomaterials, 2003. 24(20): p. 3521-3530.

33. Picart, C., et al., Primary Cell Adhesion on RGD-Functionalized and Covalently Crosslinked Thin Polyelectrolyte Multilayer Films. Advanced Functional Materials, 2005. 15(1): p. 83-94.

34. Schneider, A., et al., Polyelectrolyte multilayers with a tunable Young's modulus: influence of film stiffness on cell adhesion. Langmuir, 2006. 22(3): p. 1193-1200.

35. Werner, S., et al., The effect of microstructured surfaces and laminin-derived peptide coatings on soft tissue interactions with titanium dental implants. Biomaterials, 2009. 30(12): p. 2291-2301.

36. Kim, S., A.E. English, and K.D. Kihm, Surface elasticity and charge concentration-dependent endothelial cell attachment to copolymer polyelectrolyte hydrogel. Acta Biomater, 2009. 5(1): p. 144-151.

37. Zhu, Y. and Y. Sun, The influence of polyelectrolyte charges of polyurethane membrane surface on the growth of human endothelial cells. Colloids and Surfaces B: Biointerfaces, 2004. 36(1): p. 49-55.

38. Knight, C.G., et al., The collagen-binding A-domains of integrins alpha(1)beta(1) and alpha(2)beta(1) recognize the same specific amino acid sequence, GFOGER, in native (triple-helical) collagens. J Biol Chem, 2000. 275(1): p. 35-40.

39. Reyes, C.D., et al., Biomolecular surface coating to enhance orthopaedic tissue healing and integration. Biomaterials, 2007. 28(21): p. 3228-3235.

40. Wojtowicz, A.M., et al., Coating of biomaterial scaffolds with the collagen-mimetic peptide GFOGER for bone defect repair. Biomaterials, 2010. 31(9): p. 2574-2582.

41. Saunders, R. and D. Hammer, Assembly of Human Umbilical Vein Endothelial Cells on Compliant Hydrogels. Cellular and Molecular Bioengineering, 2010. 3(1): p. 60-67.

42. Li, C., A. Hill, and M. Imran, In vitro and in vivo studies of ePTFE vascular grafts treated with P15 peptide. J Biomater Sci Polym Ed, 2005. 16(7): p. 875-891.

43. Hersel, U., C. Dahmen, and H. Kessler, RGD modified polymers: biomaterials for stimulated cell adhesion and beyond. Biomaterials, 2003. 24(24): p. 4385-4415.

44. Massia, S.P. and J.A. Hubbell, An RGD spacing of 440 nm is sufficient for integrin alpha V beta 3-mediated fibroblast spreading and 140 nm for focal contact and stress fiber formation. J Cell Biol, 1991. 114(5): p. 1089-1100.

45. Beer, J.H., K.T. Springer, and B.S. Coller, Immobilized Arg-Gly-Asp (RGD) peptides of varying lengths as structural probes of the platelet glycoprotein IIb/IIIa receptor. Blood, 1992. 79(1): p. 117-128.

46. Haynie, D.T., et al., Polypeptide multilayer films: role of molecular structure and charge. Langmuir, 2004. 20(11): p. 4540-4547.

47. Leung, D.W., et al., Vascular endothelial growth factor is a secreted angiogenic mitogen. Science, 1989. 246(4935): p. 1306-1309.

48. Neufeld, G., et al., Vascular endothelial growth factor (VEGF) and its receptors. FASEB J, 1999. 13(1): p. 9-22.

49. Byrne, A.M., D.J. Bouchier-Hayes, and J.H. Harmey, Angiogenic and cell survival functions of vascular endothelial growth factor (VEGF). J Cell Mol Med, 2005. 9(4): p. 777-794.

50. Sieminski, A.L. and K.J. Gooch, Biomaterial-microvasculature interactions. Biomaterials, 2000. 21(22): p. 2232-2241.

51. Vailhe, B., D. Vittet, and J.J. Feige, In vitro models of vasculogenesis and angiogenesis. Lab Invest, 2001. 81(4): p. 439-452.

52. Francis, M.E., S. Uriel, and E.M. Brey, Endothelial cell-matrix interactions in neovascularization. Tissue Eng Part B Rev, 2008. 14(1): p. 19-32.

53. Dejana, E., Endothelial cell-cell junctions: happy together. Nat Rev Mol Cell Biol, 2004. 5(4): p. 261-270.

54. Waltenberger, J., et al., Different signal transduction properties of KDR and Flt1, two receptors for vascular endothelial growth factor. J Biol Chem, 1994. 269(43): p. 26988-26995.

55. Rousseau, S., et al., p38 MAP kinase activation by vascular endothelial growth factor mediates actin reorganization and cell migration in human endothelial cells. Oncogene, 1997. 15(18): p. 2169-2177.

56. Rousseau, S., et al., Vascular endothelial growth factor (VEGF)-driven actin-based motility is mediated by VEGFR2 and requires concerted activation of stress-activated protein kinase 2 (SAPK2/p38) and geldanamycin-sensitive phosphorylation of focal adhesion kinase. J Biol Chem, 2000. 275(14): p. 10661-10672.

57. Dejana, E., M. Corada, and M.G. Lampugnani, Endothelial cell-to-cell junctions. FASEB J, 1995. 9(10): p. 910-918.

58. Dejana, E., G. Bazzoni, and M.G. Lampugnani, Vascular endothelial (VE)-cadherin: only an intercellular glue? Exp Cell Res, 1999. 252(1): p. 13-19.

59. J. Schwarzkopf et al., Progress in Crystal Growth and Characterization of Materials **52**, 159 (2006)

60. P. Mukherjee, J. Cuff, S. Witanachchi, Appl. Surface Science 127-129 (1998) 620-625.

61. S. Witanachchi, K. Ahmed, P. Sakthivel, P. Mukherjee, Appl. Phys. Lett. **66**, 1469 (1995)

62. X. Y. Chen, Z. G. Liu Appl. Phys. A **69** [Suppl.], S523-S525 (1999)

63. S. Witanachchi and P. Mukherjee, "Role of Temporal Delay in Dual-Laser Ablated Plumes", Journal of Vacuum Science and Technology, **A13**, 1171-1174, 1995.

64. P. Mukherjee, S. Chen and S. Witanachchi, "Effect of initial plasma geometry and temperature on dynamic plume expansion in dual-laser ablation", Applied Physics Letters, **74**, 1546-1548, 1999.

65. P. Mukherjee, J. B. Cuff, and S. Witanachchi, Rev. Sci. Instrum. 72, 2380 (2001)

66. P. Mukherjee, J. Cuff, and S. Witanachchi, Appl. Surface Science 127-129, 620 (1998)

67. D. Mukherjee, R. Hyde, T. Dhakal, H. Srikanth, P. Mukherjee and S. Witanachchi, Mater. Res. Soc. Symp. Proc. 1199, 37(2009).

68. Feng Chen, Q. Z. Liu, H. F. Wang, F. H. Zhang, and Wenbin Wu, Appl. Phys. Lett. 90, 192907 (2007)

69. S. Witanachchi, K. Ahmed, P. Sakthivel, P. Mukherjee, Appl. Phys. Lett. 66, 1469 (1995)

70. Lee E W 1955 *Rep. Prog. Phys.* **18** 184-229

71. Kneller E 1962 *Ferromagnetismus* (Berlin: Springer)

72. D Sander 1999 *Rep. Prog. Phys.* **62** 809–858

73. Jiles D C and Atherton D L 1984 *J. Phys. D: Appl. Phys.* **17** 1265–81

74. Bozorth R M, Tilden E F and Williams A J 1955 *Phys. Rev.* **99** 1788

75. Ranvah N, Nlebedim I C, Melikhov Y, Snyder J E, Jiles D C, Moses A J, Williams P I, Anayi F and Song S H 2008 *IEEE Trans. Mag.* **44**, 3013

76. Paulsen J A, Ring A P, Lo C C H, Snyder J E and Jiles D C 2005 *J. Appl. Phys.* **97** 044502

77. Chen Y, Snyder J E, Dennis K W, McCallum R W and Jiles D C 2000 *J. Appl. Phys.* **87** 5798

78. Inoue M, Yamamoto S, Fujita N and T. Fujii 1987 *IEEE Trans. Mag.* **23** 3334

79. Ramesh R and Spaldin N A 2007 *Nature Materials* **6** 21-9

80. Zheng H, Wang J, Lofland S E, Ma Z, Mohaddes-Ardabili L, Zhao T, Salamanca-Riba L, Shinde S R, Ogale S B, Bai F, Viehland D, Jia Y, Schlom D G, Wuttig M, Roytburd A and R. Ramesh 2004 *Science* **303** 661

81. Zhou J P, Qiu Z C and Liu P 2008 *Mater. Res. Bull.* **43** 3514

82. Vopsaroiu M, Blackburn J and Cain M G 2007 *J. Phys. D: Appl. Phys.* **40** 5027–5033

83. Li Z, Wang Y, Lin Y and Nan C 2009 *Phys. Rev. B* **79** 180406(R)

84. Sim C H, Pan Z Z and Wang J 2009 *J. Appl. Phys.* **105** 084113

85. He H, Ma J, Lin Y and Nan C W 2008 *J. Appl. Phys.* **104** 114114

86. He H C, Wang J, Zhou J P and Nan C W 2007 *Adv. Funct. Mater.* **17** 1333

87. Zhou J P, He H C, Zhang Y, Deng C Y, Shi Z, Nan C W 2007 *Appl. Phys. A* **89** 553

88. Zhou J P, He H, Shi Z and Nan C W 2006 *Appl. Phys. Lett.* **88** 013111

89. Ortega N, Kumar A, Katiyar R S and Rinaldi C 2009 *J. Mater. Sci.* **44** 5127

90. Zhang Y, Li Z, Deng C, Ma J, Lin Y and Nan C W 2008 *Appl. Phys. Lett.* **92** 152510

91. Nan C, Bichurin M I, Dong S, Viehland D and Srinivasan G 2008 *J. Appl. Phys.* **103** 031101

92. Zhang J X, Dai J Y and. Chan H L W 2010 *J. Appl. Phys.* **107** 104105

93. Eom C B, Van Dover R B, Phillips J M, Werder D J, Marshall J H, Chen C H, Cava R J, Fleming R M and Fork D K 1993 *Appl. Phys. Lett.* **63**, 2570

94. Dhakal T, Mukherjee D, Hyde R, Mukherjee P, Phan M H, Srikanth H and Witanachchi S, 2010 *J. Appl. Phys.* **107** 053914

95. Hirata K, Moriya K and Waseda Y 1977 *J. Mater. Sci.* **12**, 838

96. Meyer G M, Nelmes R J and Hutton J 1978 *Ferroelectrics* **21**, 461

97. Huang W, Zhu J, Zeng H Z, Wei X H, Zhang Y and Li Y R 2006 *Appl. Phys. Lett.* **89** 262506.

98. P. Sharma et. al., Nature Materials, **2**, 673 (2003)

99. Andrea Dal Corso, Michel Posternak, Raffaele, and Alfonso Baldereschi, Physical Review B, **50**, 10175 (1994)

100. R. D. Vispute et. al, Applied Physics Letter, **73**, 348 (1998)

101. Q. H. Li, T. Gao, Y. G. Wang, and T. H. Wang, Applied Physics Letters **86**, 123117 (2005)

102. Mrinal Dutta and Durga Basak, Nanotechnology **20**, 475602 (2009)

103. D. Corso et. al, Phys. Rev. B 50, 10715 (2004).

104. T. Shibata et. al, Sens. Actuators, A **102**, 106 (2002)

105. Y. C. Yang et al., Appl. Phys. Lett. **92**, 012907 (2008)

106. Y. C. Yang et al., Appl. Phys. Lett. **90**, 242903, (2007)

107. C. Namchul, et. al., *Adv. Mater.*, **19**, 232-236 (2007)

108. A. N. Aleshin, S. R. Williams, A. J. Heeger, *Synth. Met.* **94**, 173, 1998

109. P. Nguyen, S. A. de Vos, *Appl. Surf. Sci.* **221**, 330, 2004

110. A. Nozik, *Chemical Physical Letters,* **457**, 3-11 (2008).

111. W. Zhang, L. Zhang, Y. Cheng, Z. Hui, X. Zhang, Y. Xie, and Y. Qian, Materials Research Bulletin 35, 2009 (2000).

112. M. Fanun, *Microemulsions: Properties and Applications*, CRC Press (2008).

113. A.Popescu, L.M. Woods, J. Martin, and G.S. Nolas, Phys. Rev. B 79, 205302 (2009).

114. L.M. Woods, A. Popescu, J. Martin, and G.S. Nolas, MRS Symposium Proceedings, Vol. 1166-N05-08 (2009).

115. L.M. Woods, A. Popescu, A. Datta, and G.S. Nolas, J. of Appl. Phys., to be submitted.

116. D.B. Rogers, R.D. Shannon, C.T. Prewitt, J.L. Gillson, Inorg. Chem. 10 (1971) 723.

117. H. Kawazoe, M. Yasukawa, H. Hyodo, M. Kurita, H. Yanagi, H. Hosono, Nature 389 (1997) 939.

118. H. Yanagi, S. Inoue, K. Ueda, H. Kawazoe, H. Hosono, J. Appl. Phys. 88 (2000) 4159.

119. M.A. Marquardt, N.A. Ashmore, D.P. Cann, Thin Solid Films 496 (2006) 146.

120. K. Isawa et al, in *Oxide Thermoelectrics* (Research Signpost, Trivandrum, India, 2002), edited by K. Koumoto, p. 213.

121. D.J. Singh, Phys. Rev. B 76 (2007) 085110.

122. D.J. Singh, Phys. Rev. B 77 (2008) 205126.

123. R.D. Shannon, D.B. Rogers, C.T. Prewitt, Inorg. Chem. 10 (1971) 713.

124. H.H. Emons, E. Beger, Z. Chem. 7 (1967) 200.

125. P. Porta, R. Dragone, G. Fierro, M. Inversi, M. L. Jacono, G. Moretti, J. Chem. Soc. Faraday Trans. 88 (1992) 311.

126. T. Wangensteen, S. Witanachchi, and P. Mukherjee, "Initial Studies of thermoelectric nanoparticle growth using a laser-assisted spray pyrolysis (LASP) method", *ACS*, (2007).

127. Y.F. Hu, E. Sutter, W.D. Si, and Li Qiang, "Thermoelectric properties and microstructure of c-axis-oriented thin films on glass substrates", *Applied Physics Letters,* **87**, 171912 (2005)

128. S. S. Harilal, B. O'Shey, M. Tillack, M. Mathew, "Spectroscopic characterization of laser induced tin plasma", *J. Appl. Phys. 98*, 01330, (2005)

129. NIST, *Basic Atomic Spectroscopic Data, Website*, Tables of Argon, Oxygen constants

130. A. Patterson, "The Scherrer Formula for X-Ray Particle Size Determination". *Phys. Rev.* (American Physical Society) **56** (10): 978-982. November 1939

131. Kuldeep S. Rathone, D. Patidar, et.al, "Structural and Optical Characterization of chemi-cally synthesized ZnS nanoparticles", Chalcogenide Letters, Vol 5, No. 6, (2008), p. 105-110